Methods and technologies for high-throughput and high-content small animal screening

by

Christopher B. Rohde

B.Sc., The University of Manitoba (2002)
M.Sc., The University of Manitoba (2006)

Submitted to the Department of Electrical Engineering and Computer Science
in partial fulfillment of the requirements for the degree of

Doctor of Philosophy

at the

MASSACHUSETTS INSTITUTE OF TECHNOLOGY

February 2012

Author .....
Department of Electrical Engineering and Computer Science
January 13, 2012

Certified by .....
Mehmet Fatih Yanik
Associate Professor of Electrical Engineering
Thesis Supervisor

Accepted by .....
Leslie A. Kolodziejski
Professor of Electrical Engineering
Chair of the Committee on Graduate Students

Methods and technologies for high-throughput and high-content small animal screening

by

Christopher B. Rohde

Submitted to the Department of Electrical Engineering and Computer Science
on January 13, 2012, in partial fulfillment of the requirements for the degree of
Doctor of Philosophy

Abstract

High-throughput and high-content screening (HTS and HCS) of whole animals requires their immobilization for high-resolution imaging and manipulation. Here we present methods to enable HTS and HCS of the nematode *Caenorhabditis elegans (C. elegans)*. First we present microfluidic technologies to rapidly isolate, immobilize, image and manipulate individual animals. These technologies include **1.** a high-speed microfluidic sorter that can isolate and immobilize *C. elegans* in a well defined geometry for screening phenotypic features in physiologically active animals, **2.** an integrated chip containing individually addressable screening-chamber devices for incubation and exposure of individual animals to biochemical compounds and high-resolution time-lapse imaging of multiple animals and **3.** a design for delivery of compound libraries in standard multiwell plates to microfluidic devices and also for rapid dispensing of screened animals into multiwell plates. We then present an improved immobilization method that restrains animals with sufficient stability to perform femtosecond laser microsurgery and multiphoton imaging, without any apparent effects on animal health. We subsequently screen the contents of a small-molecule library for factors affecting neural regeneration following femtosecond laser microsurgery of *C. elegans* using these technologies. This screen identifies the kinase inhibitor staurosporine as a strong inhibitor of neural regeneration, and does so in a concentration and neuronal cell type-specific manner. Finally, we present a simple device for immobilizing *C. elegans* inside standard microtiter plates that is compatible with existing HTS systems. The device consists of an array of metal pins connected to individually-controlled thermoelectric coolers. We use this to perform femtosecond laser microsurgery on *C. elegans* in microtiter plates and to analyze the regeneration dynamics over time. This analysis shows that neurons tend regenerate in single short bursts that occur stochastically within the first two days post-surgery.

Thesis Supervisor: Mehmet Fatih Yanik
Title: Associate Professor of Electrical Engineering

Acknowledgments

There are many people without whom this work would not be possible: Firstly, I would like to express my gratitude to my Ph.D. supervisor, Dr. Mehmet Fatih Yanik, for his contributions to this work and his support throughout my studies. I wish to also thank Dr. Doug Lauffenburger and Dr. Jongyoon Han, for their service on my thesis committee. I am indebted to my co-authors over the years, especially Fred Zeng, Chrysanthi Samara, and Cody Gilleland. Without their contributions this document would not be nearly as complete. I am grateful for my group members, especially Matthew Angel and Mark Scott, for their friendship throughout the years. I would like to thank my Master's supervisor, Dr. Douglas Thomson, for encouraging me to apply to MIT. I am also grateful to Frances Choi for her love and support, and to John Percival for his friendship over the years. Finally, and most importantly, I wish to thank my parents, Deanne and Peter Rohde, for their love and support throughout my academic journey and beyond.

Contents

List of Figures

Chapter 1

Introduction[†]

1.1 High-throughput and high-content screening and the use of *C. elegans*

The increase in potential molecular targets for pathway analysis and therapeutic applications, brought about by efforts such as the human genome project, has made high-throughput screening (HTS) crucial to both basic research and the biotech industry [2]. Investigations and discoveries made using high-throughput assays include determining the role of genes involved in Drosophila cell growth and viability [3], identification of inhibitors of cancer stem cells [4], and identification of compounds to promote neural outgrowth [5]. In the pharmaceutical industry, HTS is the main component of lead discovery [2]. The throughput of these methods has evolved to the point where more than 100,000 assays per day are achievable.

HTS typically employs fluorescence-based detection because of its versatility and sensitivity, and the use of fluorescence-based detection also open the door to high-content screening (HCS). For cell-based screens, HCS typically means the use of methods to examine the spatial and temporal properties of cellular components such as genes, proteins and organelles [6]. HCS assays have been used in a wide range of investigations such as the search for regulators of stem cell fate via various morphological properties [7], identification of drug targets using yeast [8] and to determine cytotoxicity of nanoparticles [9]. A survey of research groups employing HCS found that oncology groups showed the greatest

[†]**Portions of this chapter are adapted from the material found in [1].**

interest, with neurology, *in vivo* toxicology and immunology groups also expressing strong interest [10]. HCS interest is high in all areas of the pharmaceutical industry [10] and use was predicted to grow in every category other than therapeutic areas. The same survey showed that signaling pathway analysis and multiplexed assays were seen as the most relevant applications for HCS. The combination of HTS and HCS technologies can enable highly complex screens. These technologies were recently used together to profile all 21,000 protein-coding genes of the human genome for their effects on cell division, migration, and survival [11].

HTS and HCS are almost exclusively performed *in vitro*, however thorough study of many biological phenomena, including as development, organogenesis, regeneration, and aging, requires the use of animal models. The use of multicellular organisms also facilitates identification of off-target or toxic effects. The size and complexity of the instrumentation used to study large vertebrate animal models prohibits their use in high-throughput assays for rapid identification of new genes and drug targets. Because of this, researchers turn to simpler organisms, and the advantages of using small invertebrate animals as model systems for human disease have become increasingly apparent. The nematode *Caenorhabditis elegans* (*C. elegans*) is a powerful model organism due to a number of useful properties including its small size, optical transparency, rapid developmental cycle and the availability of a wide array of species-specific genetic techniques. Additionally, the small size and simple physiology of *C. elegans* make it suitable for culture in 96- and 384-well plates. Since nematodes can be cultured and screened in liquid, many techniques currently used for screening cells can be adapted for *C. elegans*. Because *C. elegans* is optically transparent, it also permits visualization of internal organs. However, since the first studies on *C. elegans* in the early 1960s, little has changed in how scientists manipulate this tiny organism by manually picking, sorting, and transferring individual animals. The reliance on manual techniques means that large-scale forward- and reverse-genetic screens can take several months to years to complete. The high-throughput techniques that exist in *C. elegans* require assays to be significantly simplified in order to be even partially automated.

1.2 Background information

Many of the properties (Summarized in Table 1.1) that make *C. elegans* a useful model organism also make it amenable to manipulation via flow cytometery and in microfluidic devices. This section outlines previous developments in microfluidic devices for behavioral experiments using *C. elegans* as well as flow cytometry methods for HTS of nematodes. In addition, several optical techniques for imaging and manipulating *C. elegans* are described.

Table 1.1: Physical features of *C. elegans*

Genome	*Length*	$\approx$ 100 Mbp
	Number of genes	$\approx$ 20,000
Life Cycle	*Maturation*	$\approx$ 3 days
	Lifespan	$\approx$ 2-3 weeks
Cells	*Hermaphrodite*	959
	Male	1,031
Progeny		$\approx$ 300 in first week
Size	*Embryo*	$\approx$ 50 µm
	Larva	$\approx$ 250-700 µm
	Adult	$\approx$ 1 mm
Neurons		302

1.2.1 Micofluidic technologies for *C. elegans* studies

C. elegans shows remarkable sensitivity to its environment, and obtaining meaningful data often requires strict control over the experimental conditions. Because of *C. elegans'* small size, this level of control can be exerted in precisely defined structures created through microfabrication techniques. Additionally, the ability of *C. elegans* to grow in liquid allows the use of microfluidic technologies for manipulating both the animals and their environment. These microfluidic devices are most often made from the flexible transparent polymer

poly(dimethylsiloxane) (PDMS) [12,13]. See Appendix B for more information on microfluidic device fabrication.

One of the earliest devices for controlling *C. elegans'* microenvironment was demonstrated by Gray *et al.* [14] to study oxygen-related behaviors. Using microfabrication methods, the authors constructed a PDMS device with a 200-µm-tall rectangular chamber with dimensions 3.3 cm × 1.5 cm. Holes were punched into the four corners of the chamber to allow for intake and outflow of air and nitrogen. By placing the intake/outflow of air on one side and intake/outflow of nitrogen on the other, the authors created an oxygen gradient across the long axis of the device. The device was placed over an agar surface and the behavior of wild-type and mutant animals was observed. Wild-type animals were observed to avoid low oxygen regions below 2% as well as high oxygen regions above 12%. *tax-2* and *tax-4*, which encode the two subunits of the 3',5'-cyclic guanosine monophosphate (cGMP)-gated sensory transduction channel, and *gcy-35*, which encodes a cGMP homolog, mutant animals were found to be defective in hyperoxia avoidance. The small size of the main chamber allowed for control of the animals' environment that would be difficult to achieve through other means.

Another novel approach by Qin and Wheeler [15] used microfabricated mazes to study the behavior of worms both individually and in groups. Microfabrication methods were used to mold PDMS with simple T-shaped and more complex branching U-shaped channels. These were placed on agar plates and used to observe the exploratory behavior of groups of animals with and without food. When a drop of the anesthetic NaN_3 was placed at the exit of the mazes, groups of animals could be run through the mazes and their destinations could be measured by recording the number of paralyzed worms at the exits over time. This allowed the authors to assess the exploratory behavior, and they showed that the wild-type animals exhibited significantly more exploratory behavior than the dopamine-deficient *cat-2* mutants. Additionally, exogenous dopamine made both types of animals more likely to explore the maze. Finally, to test associative learning associated with reward in individuals, the authors used a T-shaped maze with a reward at one end. By repositioning the maze after each trial, they could test if the worms would reach their destination faster in future attempts. Both wild-type and *cat-2* mutant animals reached the destination faster with subsequent trials; however, when the reward was removed the *cat-2* mutants were less likely than the wild-type animals to "remember" where the reward was located.

In the laboratory *C. elegans* is typically cultured on agar plates, but in the wild it is most found commonly in soil, compost, or decaying leaf or fruit [16]. Agar plates are significantly different from the worm's natural environment and this may affect observations of animal behavior. To represent *C. elegans'* natural environment more closely, Lockery *et al.* [17] created microfabricated PDMS devices consisting of a 1 cm $\times$ 1 cm $\times$ 50 µm array of small cylindrical posts bonded to glass in order to mimic moist soil. Due to the precision achievable by microlithographic techniques, the authors were able to vary the size and spacing of the posts easily. Whereas the motion of the animals in the artificial soil device exhibited the same principal characteristics of the motion of crawling on agar, the constraints on motion caused by the posts likely better mimicked the complexity of *C. elegans'* natural environment. The use of microfluidics also facilitated precise environmental modification, which the authors demonstrated by modifying the NaCl concentration of the main chamber rapidly and immediately observing the effect on locomotion. Tracking animals through such a rapid media exchange would not be possible in a larger environment. To further study crawling behavior, the authors also created a PDMS microfluidic device that consisted of sinusoidal channels of varying wavelengths. These devices allowed the researchers to manipulate the oscillating body motion of the crawling animals; this technique can be used in investigations of the biophysical and neuronal mechanisms of locomotion and proprioception while also simplifying tracking of behavioral responses.

A similar investigation of *C. elegans* locomotion by Park *et al.* [18] studied swimming behavior. The authors used microfabrication to make molds that then were used to create posts for restricting movement of worms, but, unlike researchers conducting other investigations, the authors cast agar using the molds and left the devices unsealed. This simplified device fabrication and the loading and unloading of animals from the device. Interestingly, when microstructures with post spacings of 425-475 µm were used, animals moved much more rapidly and efficiently, reaching speeds greater than 10-fold those reached in unstructured environments. This behavior was not observed in mutants deficient in mechanosensation, suggesting a greater importance of touch-feedback in locomotory behavior than previously thought.

C. elegans locomotion was also studied by Chronis *et al.* [19], who used a tapering channel to trap *C. elegans*, but not to restrain it completely. Once the worm entered the channel, it was unable to escape, but the channel was wide enough for the animal

to generate the sinusoidal movement patterns used in locomotion. By using transgenic animals expressing G-CaMP (a genetically encoded calcium sensor) specifically in the AVA interneurons, the authors were able to correlate neuronal activity with specific body motion patterns.

In the same work, the authors also introduced a novel "olfactory chip" for stimulation of the chemosensory neurons and detection of the neuronal activity by calcium imaging [19]. Investigating neural activity in response to stimuli in *C. elegans* is particularly challenging as *C. elegans* is highly mobile. The olfactory chip held the worm in a tapered channel which restrained its motion but exposed its head to another microchannel. Four inlets then were used to switch between stimuli that flowed past the animal's nose. The authors were able to successfully measure calcium transients in the ASH sensory neurons in response to a hyperosmotic stimulus. The same device was used by Chalasani *et al.* [20] to characterize the *C. elegans* AWC olfactory neurons and their downstream interneurons. The authors expressed G-CaMP in *C. elegans* under cell-specific promoters, which allowed monitoring of the response of the these neurons to the addition and removal of odorants. This enabled the correlation of the processing of odorants with specific neural activity and the subsequent behavioral responses. A fully automated form of this technology was reported recently by Chokshi *et al.* [21], who noted significant differences in the calcium images between young and old animals.

To cultivate and observe *C. elegans* for use in space, Kim *et al.* [22] developed an automatic compact disk system with minimal size and weight. Their device used capillary forces to control fluid flow in one direction (toward the center of the disk) and centrifugal forces to pump liquid in the opposite direction (toward the edge of the disk). The use of centrifugal force in this device also enabled it to be used for studying the effects of increased gravity on *C. elegans.* Two versions of the device were created: one from PDMS and one from polycarbonate. The PDMS version consisted of multiple polymer layers clamped between two acrylic plates. One layer contained the cultivation chambers, a loading chamber, and the microfluidic connections. The other layer contained the flow lines to enable waste removal from the cultivation chambers. The authors demonstrated successful breeding of three generations of *C. elegans* inside the device.

1.2.2 Macro-scale flow cytometry based methods

Behavioral studies are valuable, but they often are limited in either throughput or information content. For performing HTS and HCS using *C. elegans* a different class of techniques is required. The methods described below enable manipulation of *C. elegans* by using their ability to survive in liquid, which allows the use of fluidics to transport animals rapidly.

Flow-cytometry techniques such as fluorescence-activated cell sorting (FACS) [23] are used frequently in modern biology and medicine for detection of marker expresion levels in cells for high-throughput counting and sorting purposes. The COPAS™ Biosort [24] is a commercially-available flow cytometer that has adapted FACS technology to sort *C. elegans*. Because *C. elegans* has a tapered cylindrical shape, is of small size, and can survive in liquid, the animals are well-suited to such flow-based techniques. The fluidic lines of the Biosort are larger than those of a standard flow cytometer and can accommodate objects as large as 150-200 µm. While the worms are flowing at high speeds, the scattered light and fluorescence intensity levels from whole worms are measured. On the basis of the measured signals, animals exiting the system can be sorted between two possible output areas using a jet of air. The first area will contain the animals being sorted for and can be either a multiwell plate (containing 24, 96 or 384 wells) or a bulk container. The second area will contain a receptacle for the remaining animals, which can be recovered if desired. Each animal that flows through the system is measured for its size and optical density, as well as its green (500-520 nm), yellow (535-555 nm) and red (600-620 nm) fluorescence emission signals. The throughput achievable using flow-cytometry techniques is very high, reaching rates up to 100 animals per second.

Flow cytometers such as the COPAS system measure only one-dimensional (1D) fluorescence profiles of the animals as they flow by the optical detection area. Nonetheless, this can be quite useful, as Doisidou *et al.* [25] demonstrated by a forward genetic screen for mutations affecting dopamine cell fate. *C. elegans* possesses eight dopaminergic neurons among its 959 cells, so sensitive measurements are required to detect mutants with a reduced number of these neurons. The authors used a broadly expressed red fluorescent protein (RFP) background to control for changes in fluorescence expression of the green fluorescent protein (GFP)-labeled dopamine neurons. By sorting based on the ratio of green to red fluorescence, the authors isolated mutants with reduced neuronal GFP expression.

These mutants included those with reduced GFP expression in some or all of the dopamine neurons and, most interestingly, those with a reduced number of dopaminergic neurons. Mapping of the mutations of the latter category revealed new genes affecting dopamine cell fate.

The large-bore fluidics of the COPAS Biosort are required for analyzing mature animals, but earlier stages of *C. elegans* are small enough to be compatible with standard FACS machines. Stoeckius *et al.* [26] used conventional FACS to collect tens of thousands of precisely staged *C. elegans* embryos. Typically, isolation of embryos from groups of gravid adults yields a wide range of embryo stages, ranging from single-cell embryos to nearly hatched larvae, and manual collection of precisely-staged *C. elegans* embryos severely limits the amount of embryos collected. To isolate a large number of single-cell-stage embryos, the authors used a strain that expressed GFP in developing oocytes and in one-cell-stage embryos, but that rapidly lost fluorescence beyond the single-cell stage. Sorting mixed-stage embryos obtained from gravid adults yielded a sample containing $\approx 70\%$ one-cell-stage embryos. Because embryonic cell division progresses rapidly, the authors were unable to enrich this population further without methanol fixation of the embryos. However, fixation enabled sorting of $\approx 60{,}000$ one-cell stage embryos with $> 98\%$ purity. In addition to one-cell embryos, the authors examined two- to four-cell-stage embryos (by selecting for cells with reduced fluorescence expression), older embryos (by selecting for cells with no fluorescence expression), post-gastrulation embryos (by allowing isolated embryos to develop for 3h at 20 °C), and a population of mixed-stage embryos. From these six sample types the authors sequenced small RNA (sRNA) samples to study sRNAs in early embryogenesis. Among their findings were that most microRNAs (miRNAs) are expressed in the one-cell-stage embryo, suggesting maternal deposition of the miRNAs. They also showed that the miRNAs from the miR-35 cluster are most likely specific to the early embryo.

In addition, the use of conventional FACS to sort early larval stage worms was demonstrated by Fernandez *et al.* [27]. By making minor and reversible modifications to a commercial FACS machine the authors were able to collect a nearly 100% pure population of first-larval-stage (L1) *mel-28* [28] homozygous worms from a mixed population using two passes through the machine. A mutation in *mel-28*, which is required for nuclear envelope integrity and chromosome segregation, was kept over a balancer chromosome containing a GFP marker and a recessive lethal allele. Thus, sorting for GFP-negative animals, enabled

a population homozygous for *mel-28* to be obtained. The authors used these animals to perform an RNAi-based synthetic interaction screen on the genes from chromosome 1 and identified several genes that interact with *mel-28*. Collecting a large number of these animals would be challenging by other means, because homozygous *mel-28* mutations cause embryonic lethality in the progeny.

1.2.3 Optical techniques for imaging and manipulating *C. elegans*

Methods for manipulation and immobilization of *C. elegans* can enable the use of many precise optical techniques in a rapid and repeatable fashion. In this section, *C. elegans* techniques that are compatible with the methods described in the subsequent chapters of this work are outlined.

Free-space imaging techniques

Phase/interference contrast and epifluorescence microscopy are used commonly by *C. elegans* laboratories for both low- and high-resolution imaging. In addition to allowing rapid high-resolution imaging, techniques that enable stable immobilization of animals permit the use of additional imaging methods that allow precise measurements to be performed, such as those outlined in this section.

Laser scanning confocal [29] and two-photon [30] microscopies allow 3D imaging of fluorescently labeled features with very high resolution and minimal out-of-plane fluorescence. However scanning techniques require the worms to be stably immobilized in order to scan the animal and reconstruct 3D images. Filippidis *et al.* [31] demonstrated the use of two-photon imaging in *C. elegans* combined with another nonlinear optical technique, second harmonic generation. By combining the two methods, the authors simultaneously mapped neurons (using two-photon excitation fluorescence) and musculature (using second-harmonic generation) in the *C. elegans* pharynx. These imaging modalities later were combined with third-harmonic generation to enable 3D imaging of organs [32] and to monitor neural degeneration [33].

Fluorescence-based techniques require that animals be labeled either chemically or genetically. For monitoring certain biological processes fluorescent labeling can be inconvenient or may interfere with normal behavior. Coherent anti-Stokes Raman scattering (CARS) microscopy [34] allows specific, label-free *in vivo* imaging through detection of

the characteristic vibrational spectrum of certain molecular bonds. Hellerer *et al.* used CARS microscopy to monitor the effect of environmental conditions of mutations affecting metabolic pathways on lipid storage [35]. A more recent investigation examined lipid metabolism in *C. elegans* using a combination of CARS, two-photon excited fluorescence, and confocal Raman spectral analysis [36]. Like two-photon microscopy, CARS is also a scanning technique that requires immobilization of worms for high-resolution imaging. Coupled with a method for rapid and repeatable worm immobilization, CARS microscopy can accelerate *in vivo* investigations of lipid storage significantly.

Optogenetics techniques

The use of calcium imaging and microfluidics to image the activity of specific neurons is discussed in Section 1.2.1. In addition to measurement of neuronal activity, control of neural activity in *C. elegans* can be achieved through the use of optogenetic methods. Optogenetics [37] is an emerging field that uses genetic targeting of light-activated channels and enzymes to manipulate neural activity *in vivo* precisely and rapidly. Channelrhodopsin-2 (ChR2) [38], a single-component light-activated cation channel from algae, can be used to optically excite neurons [39, 40]. The light-driven chloride pumping halorhodopsins [41] (Halo) can serve as the complement to ChR2, enabling optical inhibition of neurons [42,43]. Microfluidic techniques have been combined with optogenetics for rapid investigation of neural circuits in *C. elegans* [44].

Lensless imaging of *C. elegans*

Microfluidic technologies and similar methods can be advantageous also owing to the small size and low cost of the resulting devices. However, nearly all of these devices are designed to operate on expensive and bulky compound microscopes, reducing these benefits. Several methods integrate on-chip imaging systems into devices for *C. elegans* screening. The first system to provide integrated imaging capabilities was the microfludic shadow imaging system by Lange *et al.* [45]. This device was designed to enable culture and imaging of *C. elegans* to study the effects of spaceflight (here as part of a satellite payload) on *C. elegans* behavior. The significant size, weight, and power restrictions of a satellite payload preclude the use of standard microscopes, so the authors designed a 500 µm-tall transparent microchamber that was illuminated from the top using a light-emitting diode (LED). Such

illumination casts a shadow of the worms onto a complementary metal-oxide-semiconductor (CMOS) chip below the chamber, allowing acquisition of still images and movies of the worms' behavior. The 3.2 mm $\times$ 2.5 mm oval-shaped culture chamber in which the worms resided was milled from polycarbonate, a gas-permeable membrane was bonded to the top of the polycarbonate and optically clear polyester film was bonded to the bottom. Animals to be imaged were loaded via a syringe, and the animals were kept inside the chamber using Teflon stop pins at the chamber inlets.

The system designed by Lange *et al.* [45] was created to monitor the behavior of whole organisms and was not designed to image cellular or subcellular-level features. Traditionally, imaging these features requires an expensive objective lens housed inside a compound microscope. Without a lens, imaged features are limited by the sensor size of the detector, which is typically $\geq$ 5 µm. Optofluidics [46], the fusion of microfluidics and optics, offers a partial solution to this problem. Optofluidic microscopy (OFM) is a lensless method to image beyond the sensor-size limit, enabling on-chip high-resolution imaging in microfluidic channels [47]. In OFM, nematodes are flown through a narrow channel in a PDMS chip that is bonded to an opaque metal film into which an array of submicrometer holes have been etched. The film can be fabricated directly onto the detector array, and the holes are arranged to form a diagonal line across the channel. Each hole is designed to match to an individual pixel on the detector, so that line scans captured as the object flows past the array can be used to reconstruct a 2D image of the animal. Because the holes form a diagonal line, the spacing between imaged points across the channel can be adjusted by changing the angle of the line. This means that the 2D resolution limit of the system is limited only by the size of the elements in the hole array (and the detector speed). To properly unskew the image captured through the hole array, the flow velocity must be known. This is calculated using the duration between the time when the object being imaged passes an isolated aperture at one end of the array and the time when it passes the hole in the array with the same y-coordinate. If the object is rotating as it passes the detector array, it cannot be properly unskewed. Rotating objects can be detected, however, by comparing the line scans between the two apertures used to calculate flow velocity.

An early demonstration of OFM used a microscope to relay the signal from the hole array to the detector [47], whereas a later demonstration of the technique fabricated the array directly on a CMOS sensor with a 9.9-µm pixel size [48]. The latter demonstration used two

sets of hole arrays to improve measurements of velocity and detection of object rotation. This technique was capable of capturing images of similar quality to those captured by a conventional microscope with a 20× objective lens; however, both demonstrations used fixed worms for imaging, and despite high theoretical imaging speed, the highest throughput observed was approximately five worms per minute. The same group recently demonstrated a version of the optofluidic microscope capable of imaging in color, which they used to image LacZ-stained fixed L1 animals [49].

A significantly faster lensless method was demonstrated by Isikman *et al.* who used incoherent lensless in-line holography [50] to image *C. elegans* at a resolution similar to that of a 10x objective lens over an area of > 24 mm in less than one second [51]. Monochromatic, spatially-incoherent light was passed through a small aperture 50-100 µm in diameter to image animals. The aperture sat 5-10 cm above the transparent sample plane that contained the animals, which was, in turn, situated 1-2 cm above a detector. This resulted in light with a 500-1000-µm coherence diameter at the sample, and the scattering of the incident waves by the individual animals was recorded. Because the individual animals were smaller than the coherence diameter, they were effectively illuminated by the incident wave, and digital reconstruction techniques [52, 53] were used to restore the phase information lost during recording. The system worked with various wavelengths of incident light, and thus by combining images captured through different monochromatic sources, color images could be acquired. Isikman *et al.* [50] used this method to obtain monochromatic images of animals captured between two cover slips, and color images of Ponceau-S-red-stained animals. A significant limitation of lensless imaging techniques is that they can only acquire 2D images, whereas many *C. elegans* studies require 3D microscopy.

Image analysis of *C. elegans*

Techniques enabling rapid imaging and manipulation of *C. elegans* encounter a bottleneck in the rate at which data can be acquired and/or analyzed. Image processing can enable partial or complete automation of data gathering and processing, significantly augmenting the utility of some of the techniques described so far. In addition to the methods for analyzing still images of *C. elegans* described below, there are several algorithms for behavioral analysis. These have been reviewed recently [54] and are not covered extensively here. However, many of the techniques for motility analysis previously developed were designed

for a particular animal environment (e.g., agar pads, fluidics, or microfluidic devices), and may be difficult to adapt to other environments. Recently, a framework to estimate an environmental model from a single image was demonstrated by Sznitman *et al.* [55]. This platform, based on a Mixture of Gaussians model, permitted analysis of behavior across a range of environments. To better understand neural mechanisms of behavior, Faumont and Lockery demonstrated the use of a two-objective system to simultaneously monitor neuronal activity (by using a calcium-sensitive fluorescent reporter at high magnification) and behavior (by imaging a large field of view at low magnification) [56]. Ben Arous *et al.* [57] also constructed a two-objective system incorporating feedback to control a motorized stage that allowed long-term automatic tracking of single worms within the field of view of a low-magnification objective lens for calcium imaging.

There are similarly several techniques for analyzing static images or image stacks of *C. elegans* to segment and analyze individual animals automatically; however, when *C. elegans* is anesthetized on agarose pads for imaging, the worms are oriented and curved randomly. Similarly, whereas we use pressure differentials and compressive membranes to align animals linearly, many microfluidic techniques leave animals unoriented. This significantly complicates the comparison of worms, which would be simpler if all the animals were in a linear orientation. Additionally, if the animals could be straightened, less image data would need to be stored (the bounding box for straightened images of worms is, on average 80% smaller [58]); this benefit becomes significant for large-scale image-based screens. Recently, a "worm-straightening" image-processing algorithm that operates effectively on both 2D and 3D images was developed [58]. The algorithm calculates the worm "backbone", a 1-pixel line that passes from the tail to the head through the center of the worm (in 2D or 3D). Once the backbone has been determined, the planes orthogonal to the backbone are found. These planes are then rotated and restacked along a linear backbone to create the straightened worm image.

An additional challenge is faced when imaging multiple nematodes, because the animals may cluster together. This significantly complicates identification of individual animals if they overlap. To overcome this, Wahlby *et al.* [59] developed an algorithm to extract individual animals from clusters. To identify the individual animals, the authors used a probabilistic shape model to represent the variability in a worm's body orientation. They began by using a learning methodology and a training set of individual animals to determine

the space of possible worm positions and their likelihood. The authors assumed that any detected object with a size greater than 1.5 times the mean worm size is a cluster, and, by calculating the pruned skeleton of the worm cluster and cutting it at the branch points, the authors obtained an undirected graph that represented possible arrangements of worms that could result in the observed clusters. The training enabled the algorithm to select the most probable arrangement of worms that would produce the cluster, allowing reliable worm segmentation.

Body straightening and segmentation algorithms enable simplified or automated image acquisition, and can also facilitate comparison of animals. However, further techniques are necessary to analyze detailed phenotypes. For this purpose, Orlov *et al.* [60] developed pattern-recognition methods to assess the relative age of *C. elegans* automatically. Differential interference contrast (DIC) images of the terminal bulb of the pharynx and fluorescence images of the body wall muscles were used to train a network using supervised machine learning. The prediction of age for individual worms was not very high, but the mean prediction for groups of worms was very accurate using this technique. The same group used pattern recognition of DIC images of the pharynx in age-grouped animals to show that there is a distinct stepwise transition between morphologies in aging [61]. They then studied the effect of neurotransmission mutations on the rate of these transitions. The authors also were able to identify mid-life morphological states that could accurately predict future decline. *C. elegans* is a powerful model for studying aging, and automated pattern-recognition methods in combination with techniques enabling high-throughput and high-content imaging can significantly enhance investigations in this area.

One of the most interesting properties of *C. elegans* is its well-characterized and stereotypical development and anatomy. Its cell lineage has been completely mapped [62, 63], as has the wiring of its neuronal network [64]. Although the *C. elegans* cell lineage has long been known, the exact 3D positions of the ~1,000 *C. elegans* cells during development were previously undocumented. Long *et al.* [65] have endeavored to create a 3D digital atlas of *C. elegans'* cells during the L1 stage. Previous work had examined cell lineage tracing in the dividing *C. elegans* embryo up to the 350-cell stage [66], and this later was extended to enable spatiotemporal characterization of gene expression on a per-cell basis [67]. In the embryo cells can be identified by tracking them as they divided, but in a further developed animal, all nuclei must be identified without using temporal or lineage information.

To create such an atlas of cells Long *et al.* [65] used DAPI staining to label the nuclei of all 558 cells at the L1 stage and GFP to label the 81 body-wall muscle cells (plus 1 depressor cell). The authors then captured images using a confocal microscope with a 63× oil lens. Imaged animals were straightened automatically using the technique described above, and a segmentation algorithm was used to determine the cell locations. These results were manually validated, corrected, and annotated using a system previously developed by the same group [68] and existing cell annotation information. Finally, the image stacks were mapped into the same canonical space to enable comparison. Of the 558 L1 cells, 357 could be segmented reliably and annotated and thus were included in the 3D atlas. The nuclei that could not be well characterized were located mainly in the cell-dense region of the head, and higher-resolution imaging methods could possibly overcome this difficulty. By expressing mCherry under specific promoters, the atlas was used to determine the expression levels of different proteins with single-cell resolution. This way, the authors were able to analyze the expression patterns of 93 different proteins in 363 cells of L1-stage nematodes [69].

Laser microsurgery in *C. elegans*

Ultraviolet (UV) laser ablation of individual cells in *C. elegans* anesthetized on agarose pads is a well-established technique in nematode research [70, 71], which allows study of a variety of processes, including the roles of individual neurons in neuronal networks and the interplay of cell-cell interactions on cell fate. However, out-of-focus absorption of UV light can cause uncharacterized collateral damage. The use of ultrafast near-infrared laser techniques enables highly localized ablation of subcellular features such as single axons with minimal collateral damage. Tissue is normally highly transparent to photons with low-energy near-infrared wavelengths. However, when such photons are focused both in space (via objective lens) and in time (via use of femtosecond short pulses), multiple photons can have sufficient energy to be absorbed simultaneously and generate quasi-free electrons. Appendix A describes in detail the construction of a system to perform these experiments. In 2004, the use of femtosecond laser microsurgery in the study of axonal regeneration in *C. elegans* was demonstrated [72, 73], and this method was later was adapted by several groups [74–78]. The neurites of motor neurons were cut *in vivo* using low-energy infrared laser pulses with ultrashort durations (10-40 nJ per 200 fs short pulse) delivered at a rate of 1 kHz [72, 73]. Full neurite regrowth, along with recovery of locomotive response following

touch stimulus, was observable 24 h post surgery.

Chapter 2

Microfluidic Technologies for *C. elegans* screening[†]

Abstract

We report a suite of key microfluidic devices for complex high-throughput whole-animal genetic and drug screens. We demonstrate a high-speed microfluidic sorter that can isolate and immobilize *Caenorhabditis elegans* in a well defined geometry for screening phenotypic features at subcellular resolution in physiologically active animals. We show an integrated chip containing individually addressable screening-chamber devices for incubation and exposure of individual animals to biochemical compounds and high-resolution time-lapse imaging of many animals on a single chip without the need for anesthesia. Finally, we describe a design for delivery of compound libraries in standard multiwell plates to microfluidic devices and also for rapid dispensing of screened animals into multiwell plates.

Key words: Caenorhabditis elegans, femtosecond laser microsurgery, microfluidics, immobilization and time-lapse imaging, mutagenesis, RNAi and drug screening.

[†]**This chapter is an adaptation of the material found in [79]. C.B.R., and F.Z. contributed equally to this work; M.F.Y. designed research; C.B.R., F.Z., R.G.-R., and M.A. performed research; and M.F.Y. wrote the paper.**

2.1 Motivation

Since the first studies on *C. elegans* in the early 1960s, little has changed in how scientists manipulate this tiny organism by manually picking, sorting, and transferring individual animals. The reliance on manual techniques means that large-scale forward- and reverse-genetic screens can take several months to years to complete. The high-throughput techniques that exist in *C. elegans* require assays to be significantly simplified in order to be even partially automated, due to the high motility of wild type nematodes. Imaging at the cellular level and optical manipulations such as precise laser axotomy require orientation and immobilization of animals. Traditional immobilization methods, such as the anesthetics sodium azide (NaN_3), levamisole and tricaine/tetrimisole, have significant and/or uncharacterized effects on nematode physiology, which may affect the regeneration process [80]. In addition, anesthetics need several minutes to take effect, and are thus incompatible with high-throughput screening. Other techniques that can be used to reversibly immobilize *C. elegans* include cooling [81] and exposure to CO_2 [82], however these techniques are not frequently used.

Many of the properties that make *C. elegans* a versatile and widely-studied model organism also make it amenable to manipulation in microfluidic channels. A number of novel microfluidic devices to study *C. elegans* have been published for performing specific experiments in *C. elegans*, including mazes for studying learning [15], devices for the generation of oxygen gradients [14], optofluidic imaging platforms [47,48], automated cultivation systems [22] and a shadow imaging system for studying animals in space [45].

This chapter and the next describe the development of a versatile platform which, unlike the devices mentioned above, is designed to perform general purpose experiments on *C. elegans*. This device can be used to perform forward genetic, reverse genetic, and chemical screens on *C. elegans*. Manipulation of animals is enabled by multiple layers of flexible polymers [12] that are bonded together thermally in an oven. This method allows the creation of small microfluidic valves [83] for directing fluid flow. To do this this, two layers are used, with a thin control layer below a thicker flow layer. This creates a thin membrane (10-15 µm) that separates overlapping channels between these two layers. The control layer contains single-ended channels, and when these channels are pressurized the membrane separating the overlapping regions expands into the flow channels. If the flow channels are rounded then the flow channel can be completely blocked by the membrane, allowing simple

and rapid fluidic control. A detailed protocol for fabricating a multi-layered microfluidic device similar to that of Chapter 3 is found in Appendix B.

2.2 Microfluidic sorter

Sorters enable rapid selection of organisms with phenotypes of interest for a variety of assays, including genetic and drug screens, and also for reducing phenotypic variability in large-scale assays. Existing small-animal sorters, such as the BIOSORT/COPAS machine, use a flow-through technique similar to the fluorescence-activated cell sorter (FACS) technology. These systems can capture and analyze only one-dimensional intensity profiles of the animals being sorted, and as a result, three-dimensional cellular and subcellular features cannot be resolved [84]. The animal sorter shown in Figure 2-1 was created to address this problem and to achieve on-chip integration. Animals enter the chip through the inlet channel and can be continuously recirculated. A single worm is captured in an immobilization chamber via suction by a microchannel held at a low pressure. The use of a single suction channel eliminates the problem of simultaneously capturing multiple animals. While the captured animal is held in the immobilization chamber, all of the other animals in the chamber are removed by flushing with media from a side channel. This step ensures that only a single animal is isolated even when the concentration of worms is high. The animals that are flushed in this design could be recirculated for screening if needed. Next, valves are closed to isolate the chamber containing the single worm from the rest of the chip. The captured worm is then released from the single suction channel and recaptured by an array of suction channels (the channel array) to restrain it in a straight position. At this stage, the worm can be imaged through the transparent glass substrate by using high-resolution optics for phenotype analysis (Figure 2-2). The chip is designed to allow both morphological details and fluorescence markers to be detected with white-light and epifluorescence imaging (Figure 2-2). After image acquisition and processing, the captured worm can be released and directed to the appropriate collection channels according to its phenotype.

The microfluidic chips have flow and control layers and are permanently bonded onto glass substrates to allow optical access. Flow layers are made by casting a room-temperature-vulcanizing dimethylsiloxane polymer (RTV615; GE Silicones, Wilton, CT) by using a mold consisting of a patterned layer of positive photoresist (SIPR-7123; Shin-Etsu, Tokyo, Japan)

on a silicon wafer. Flow layer channels are 250-500 μm wide and 80-110 μm high. The channels are rounded by reflowing the developed photoresist at 150 °C. In the current design, the flow layer is made from a mold with a single photoresist layer that defines suction channels that are 40 μm high and 50 μm wide after reflow, which allows capturing of adult worms. To capture juvenile worms, a two-layer photoresist mold could be used to make smaller suction channels (see Chapter 3). Control layers are made by casting from a mold consisting of a patterned layer of negative photoresist (SU-8 2075; MicroChem, Newton, MA) on a silicon wafer. Control channels are 70-80 μm high, and the membrane that separates the two layers is 10-20 μm thick. Polydimethylsiloxane chips cost significantly less than current flow-through animal-screening machines and can be easily incorporated into a variety of microscopy systems.

The speed of the sorter depends on the actuation speed of the valves, the concentration of animals at the input, the flow speed of the worms, and the image acquisition and processing times. The technique of immobilizing worms by lowering the pressure in a microchannel is fast because the actuation speed of the valves is < 30 ms. Because of the continuous recirculation at the input, animals can be flowed at high concentration without clogging the chip. The speed of image acquisition and recognition of subcellular features is fundamentally limited by the fluorescence signal-to-noise ratio and the complexity of the features being recognized. The entire worm can be imaged in a single frame by using a low magnification, high N.A. objective lens.

2.3 Additional microfluidic technologies

2.3.1 Small-animal incubation chip

Time-lapse imaging is important for a variety of assays, including drug and genetic screens. Currently, high-throughput time-lapse studies on small animals are done in multiwell plates by automated fluorescence microplate readers [85]. Because the animals swim inside the wells, only average fluorescence is obtained from each well, and cellular and subcellular details cannot be imaged. Although anesthesia can be used to immobilize the animals, they cannot be kept under anesthesia for more than a few hours, and they cannot be anesthetized frequently. Furthermore, the effect of anesthesia on many biological processes remains uncharacterized. Another limitation of current multiwell plates is the loss of animals that

occurs during media exchange. The microfluidic-chamber device shown in Figure 2-3a addresses these problems, enabling worm incubation and continuous imaging at subcellular resolution. Sorted worms can be delivered to the chambers by opening valves via multiplexed control lines [83]. The fabrication of the channels and valves is done as described in Section 2.2. To ensure that the chamber structure is not affected by the reflow process, two types of photoresist are used to make the mold for the flow layer. The chambers are first fabricated by using a 100-µm-thick layer of SU8-2075 (which does not reflow), and then the valve-controlled flow channnels are fabricated on the same wafer by using a 100-µm-thick layer of SIPR-7123. The pressure in the control lines is switched on and off with external electronically controlled valves (Numatics, Highland, MI). Because the number of control lines required to independently address n incubation chambers scales only with $log(n)$ [83], microchamber chips based on this design can be readily scaled for large-scale screening applications. Because of the millimeter scale of the microchambers, hundreds of microchambers could be integrated on a single chip. Each incubation chamber contains posts arranged in an arc. To image animals, a flow is used to push the animals toward the posts (Figure 2-3b and 2-3c). This flow restrains the animals for imaging. The circular arrangement of the posts reduces the size of the chambers and also positions the animals in a well defined geometry to reduce the complexity and processing time of image recognition algorithms. The medium in the chambers can be exchanged through the microfluidic channels for complex screening strategies. Thus, precisely timed exposures to biochemicals (e.g., drugs/RNAi) can be performed.

2.3.2 Microfluidic multiwell plate interface chip

Interfacing microfluidics to existing large-scale RNAi and drug libraries in standard multiwell plates represents a significant challenge. It is impractical to deliver compounds to thousands of microchambers on a single chip through thousands of external fluidic connectors. The microfluidic interface device (Figure 2-4) is designed to connect these microfluidic chambers to large-scale multiwell-format libraries, simplifying the delivery of existing large-scale RNAi and drug libraries. Minute amounts of individual compounds from standard multiwell plates can be routed to the incubation chambers, and the connection lines can be automatically washed between samplings. The device consists of an array of aspiration tips that can be lowered into the wells of microwell plates. The chip is designed to allow minute

amounts of library compounds to be collected from the wells by suction, routed through multiplexed flow lines one at a time, and delivered to the single output of the device. The output of the interface chip can then be connected to the microfluidic chamber device for sequential delivery of compounds to each microchamber. This device, when run in reverse, also functions as a multiplexed animal dispenser.

2.4 Discussion

Combining the devices described in different configurations can enable a wide variety of assays. Figure 2-5 shows a setup to perform large-scale RNAi and drug screens with time-lapse imaging by combining our sorter, integrated microchambers, and multiwell plate interface chips. Although *C. elegans* is self-fertilizing and has perhaps the lowest phenotypic variability among multicellular model organisms [85], variations among assayed animals are still present, reducing the robustness of current large-scale screens. Sorting technology can be used to select animals with similar phenotypes (such as fluorescent marker expression levels) before large-scale assays to significantly reduce initial phenotypic variations [85,86]. Feature extraction algorithms can be run on animals immobilized in the sorter or the incubation chambers to screen thousands of animals on a single chip.

Because the sorter and microchambers are designed to immobilize and release animals repeatedly in < 100 ms, the on-chip screening technology introduced here will allow high-throughput whole-animal assays at subcellular resolution and with time-lapse imaging in physiologically active animals. Arranging these devices in different configurations can enable a wide variety of assays. Mutagenesis screens could be performed by using the microfluidic sorter in combination with the microfluidic dispenser to dispense sorted animals at high speeds into the wells of multiwell plates (Figure 2-5a). Large-scale RNAi and drug screens with time-lapse imaging could be performed by combining the sorter, integrated microchambers, and multiwell plate interface chips as shown in Figure 2-5b. Although *C. elegans* is self-fertilizing and has perhaps the lowest phenotypic variability among multicellular model organisms [85], variations among assayed animals are still present, reducing the robustness of current large-scale screens. Sorting technology can be used to select animals with similar phenotypes (such as fluorescent marker expression levels) before large-scale assays to significantly reduce initial phenotypic variations (Figure 2-5b) [85, 86].

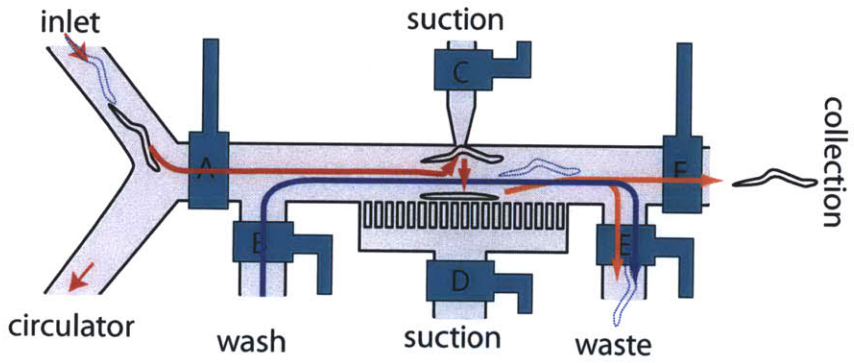

Step	A	B	C	D	E	F
1 (clean)	0	1	0	0	1	0
2 (capture)	1	0	1	0	1	0
3 (wash)	0	1	1	0	1	0
4 (immobilize)	0	0	0	1	0	0
5 (collect)	0	1	0	0	1/0	0/1

Figure 2-1: First generation sorter steps. The sorter consists of control channels and valves that direct the flow of worms in the flow channels in different directions. The valves are labeled with the letters A-F in the layout, and the actuation order of valves is listed in the table. A value of 1 represents an open valve, and a value of 0 represents a closed valve. The steps taken to sort each worm are as follows: step 1 (clean), the immobilization chamber is cleaned; step 2 (capture), a worm is captured in the chamber by suction via the top channel while the lower channel array is inactive; step 3 (wash), the chamber is washed to flush any other worms in the chamber (blue line) toward the waste or the circulator; step 4 (isolate), the chamber is isolated from all of the channels; step 5 (immobilize), the worm is released from the top suction channel and is restrained by the channel array and the image acquisition and processing are performed; step 6 (collect), the worm is either collected or directed to the waste, depending on its phenotype.

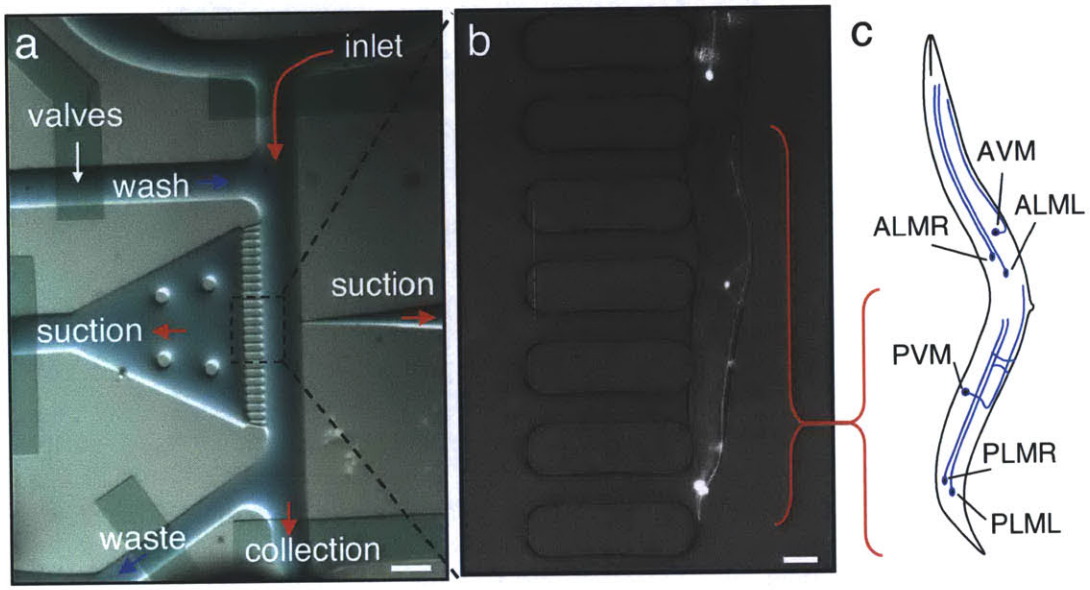

Figure 2-2: Immobilization and subcellular imaging using first generation worm sorter. (a) Image of the on-chip sorter described in Figure 2-1. (scale bar: 500 µm). (b) A single worm is shown trapped by multiple suction channels. A combined white-light and fluorescence image is taken by a cooled CCD camera with 6.45 µm pixels and a 100-ms exposure time through a 10× magnification, 0.45 N.A. objective lens (Nikon). From bottom to top, GFP-expressing PLM, PLV, and ALM touch neurons and their processes are clearly visible. (scale bar: 10 µm.) (c) The mechanosensory neurons PLML/R and ALML/R (L, left; R, right) are shown. AVM and PVM extend processes along the anterior and posterior half of the worm and contribute to mechanosensation in these regions. The cell bodies are shown as black dots. PVM, posterior ventral mechanosensory; ALM, anterior lateral mechanosensory; AVM, anterior ventral mechanosensory.

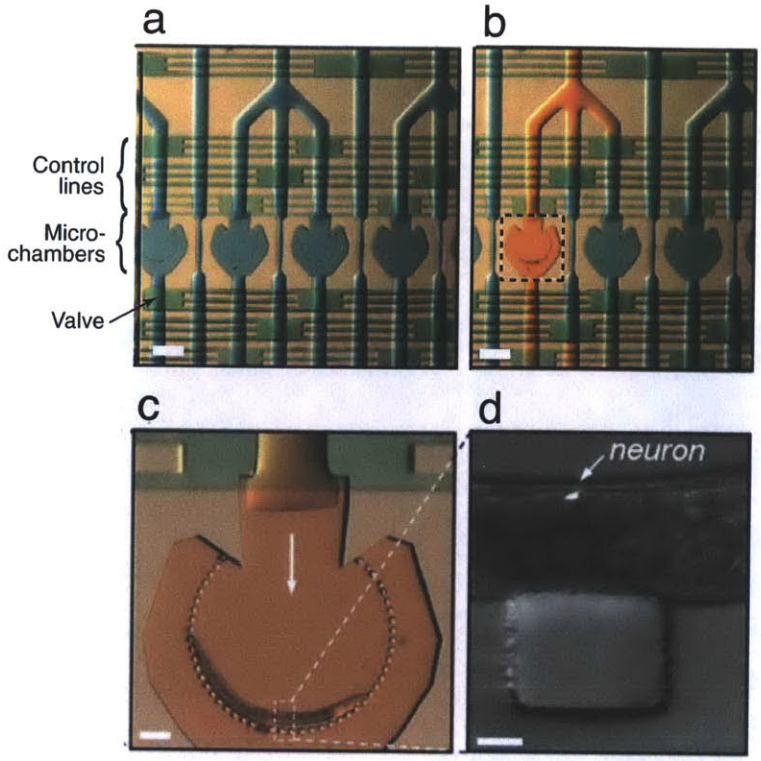

Figure 2-3: Multiplexed microfluidic incubation. (a) Device layout illustrating flow and control lines. (b) Illustration of individual chamber addressing. (c) Semi-circular post arrangement allows animal immobilization and imaging. (d) High-resolution image taken through glass substrate (scale bars a-b: 500 µm, c: 100 µm, d: 25 µm).

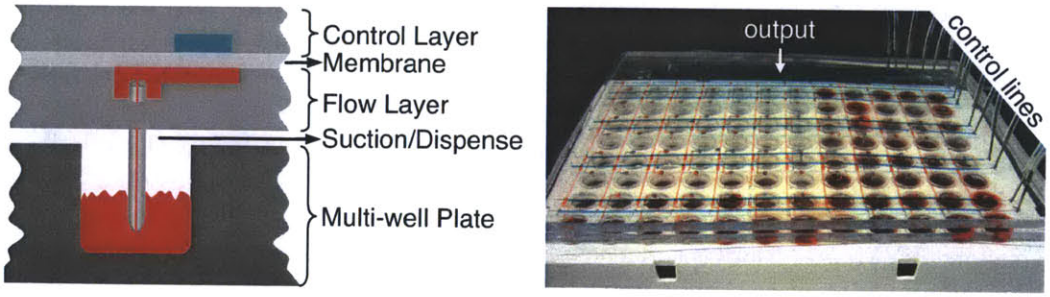

Figure 2-4: Design for delivery of compounds from standard multiwell plates to microfluidic devices. A microfluidic chip loads compounds from multiwell plates to flow channels by aspiration. The flow lines are multiplexed [83] to direct one compound at a time to a single serial output. The direction of flow in the channels is controlled by microfluidic valves. The flow lines are flushed with a wash buffer after loading each compound to prevent cross-contamination. The single serial output of this device can easily be connected to the microchamber screening chip (Figure 2-3) for compound delivery. Each microchamber chip is also multiplexed [83] to sort and deliver compounds to individual chambers (Figure 2-3).

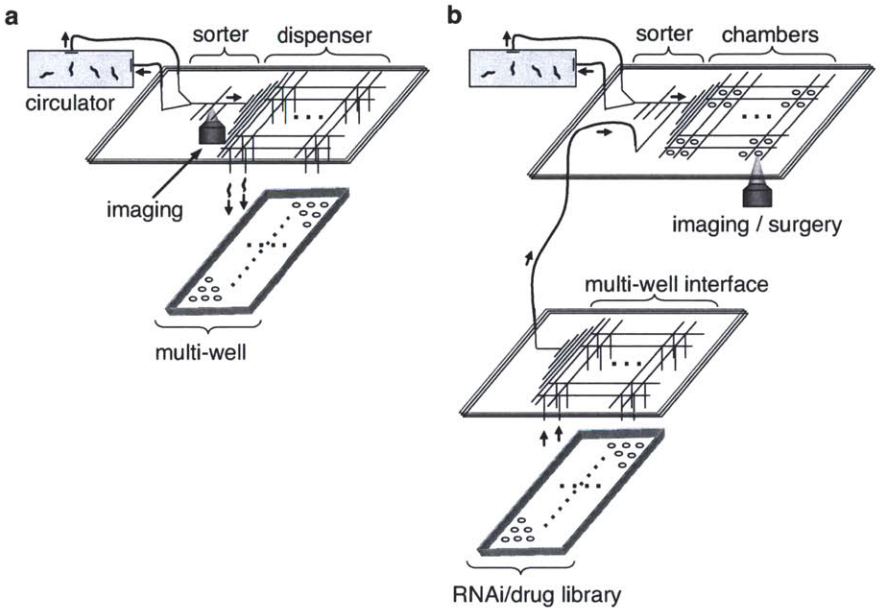

Figure 2-5: Screening Strategies. (a) High-speed phenotype screens can be performed by cascading the microfluidic sorter with the multiwell dispenser. (b) Large-scale RNAi/drug screens can be performed by delivering standard multiwell plate libraries to the microfluidic screening chambers via the multiwell interface chips.

Chapter 3

Improved *C. elegans* immobilization technology[†]

Abstract

Techniques for stable, rapid and repeatable small-animal immobilization are necessary for high-throughput *in vivo* genetic/drug screens using cellular and sub-cellular features in multi-cellular organisms. We demonstrate a method for non-invasive and high-throughput on-chip immobilization of physiologically active *C. elegans* without the use of anesthesia or cooling, but with comparable stability. We show observation and manipulation of sub-cellular features in immobilized animals using two-photon microscopy and femtosecond laser microsurgery.

Key words: Caenorhabditis elegans, microfluidics, femtosecond laser microsurgery, immobilization and time-lapse imaging.

3.1 Motivation

The devices described in the previous chapter are capable of immobilizing animals sufficiently for high-resolution imaging, and targeting individual axons for surgery is possible,

[†]**This chapter is an adaptation of the material found in [87]. Author contributions: C.B.R. and M.F.Y. designed the devices. C.B.R. and F.Z. fabricated the devices. C.B.R. and F.Z. performed the experiments. C.B.R. and M.F.Y. wrote the paper.**

however the animals are still capable of some movement in their head and tail. This chapter describes an improved immobilization method utilizing an additional microfluidic layer (the compression layer) above the channel array (Figure 3-1a) which enables more rapid and stable immobilization. A thin (15-25 µm) membrane separates this channel and the chamber below, and when this layer is pressurized, the membrane expands downwards (Figure 3-1b and 3-2d). The membrane flexes on top of the captured animals, wrapping around them and forming a tight seal. This seal completely constrains their motion in a linear orientation. Although the animals are constrained by the PDMS membrane from the top and bottom, they still have access to liquid media via the multiple aspiration channels on the side. This technique achieves stability comparable to that of deep anesthesia and affects neither the lifespan of the animals nor their brood size, and does not induce hypoxia. This method can immobilize animals in fractions of a second, and can be readily integrated with the microfluidic systems described in the previous chapter.

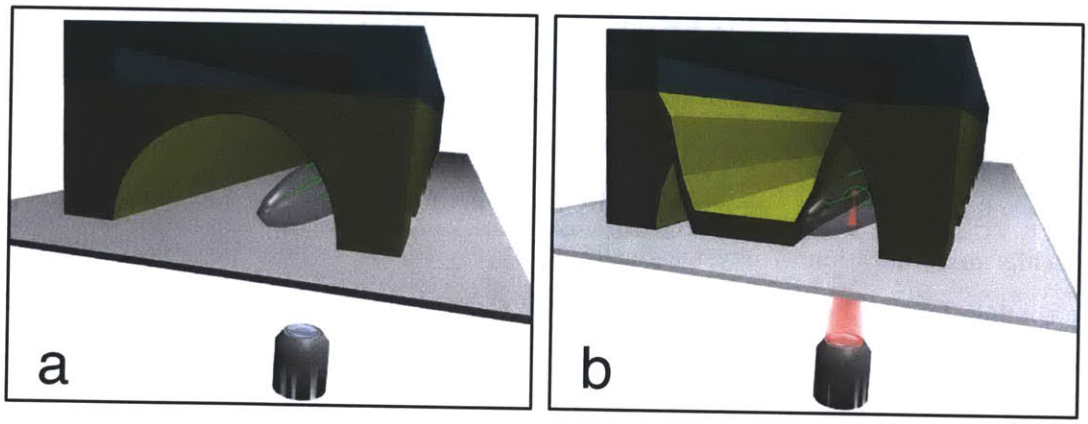

Figure 3-1: Illustration of the improved immobilization method. Once a single animal is captured and linearly oriented (a), a channel above it (in the compression layer) is pressurized pushing a thin membrane downwards (b). This membrane wraps around the animal significantly increasing immobilization stability for imaging and surgery. Precise laser targeting of sub-cellular features is achieved using a femtosecond laser tightly focused inside the *C. elegans* by a high numerical aperture objective.

3.2 Device fabrication

These improved devices consist of three PDMS layers, each fabricated from a separate master mold. To fabricate the flow layer, a master mold with two photoresist layers was

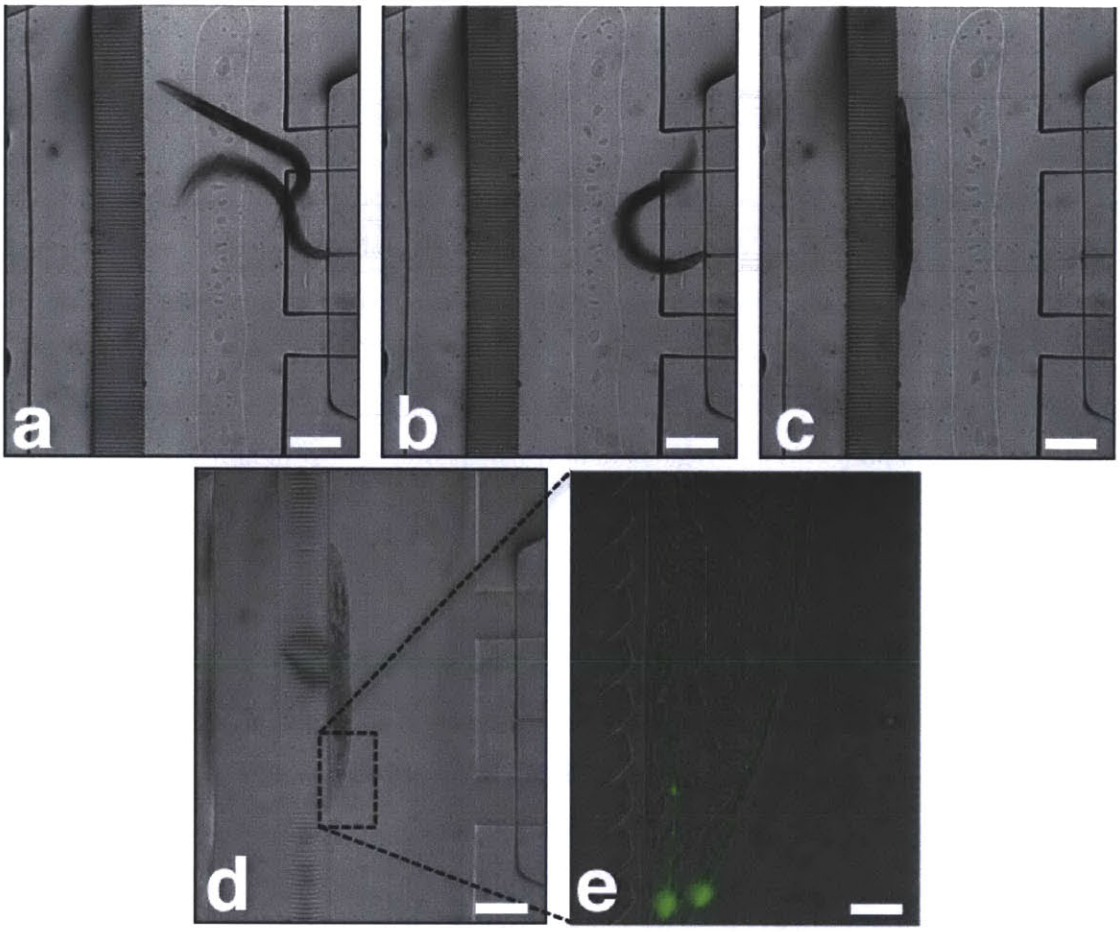

Figure 3-2: Isolation (a-b), immobilization (c-d) and imaging (e) of an individual animal. (e) shows a close-up combination bright-field and fluorescent image of an immobilized animal illustrating gfp-labeled mechanosensory axons (scale bar a-d: 250 µm, e: 20 µm).

used. The fabrication began by first spin coating and patterning a 15 µm-thick layer of SU8-2025 negative photoresist (Microchem) to define the channel array. Next, a 100 µm-thick layer of SIPR-7123 positive photoresist (Micro-Si) was spin coated and patterned to create the remaining parts of the flow layer mold. The compression and control layer molds were created from 65 µm- and 75 µm-thick layers of SU8-2050 (Microchem), respectively. From these molds RTV-615 PDMS (GE Silicones) is cast, deposited either by pouring (for the compression layer) or spinning (for the control and flow layers). Following this the layers were cured for 1 hour at 80 °C, and then bonded together thermally for 36 hours. A more detailed protocol for PDMS device fabrication of a simplified device is outline in Appendix B.

3.3 Characterization

3.3.1 Immobilization stability

To determine the effectiveness of our microfluidic immobilization technique both quantitative and qualitative analysis of the displacement of immobilized animals were performed. Figure 3-3a illustrates an animal's motion at three different time points following immobilization. Images of the anterior ventral mechanosensory (AVM) cell body and its axon were taken 5 s apart, pseudo-colored red (first time point), green and blue (final time point), and then superimposed. White regions indicate areas overlapping in all three time points. As seen in Figure 3-3a, the degree of movement for an animal immobilized in our device is small, even at 50× magnification. To quantify the effectiveness of our microfluidic immobilization versus chemical anesthesia, the cell bodies of touch neurons labeled with green fluorescent protein (GFP) were tracked using a software algorithm.

C. elegans has six touch neuron receptors, with three cells detecting anterior touch, located in the anterior mid-body (AVM, and the left and right anterior lateral mechanosensory (ALML and ALMR)), and three cells detecting posterior touch, one located in the posterior ventral mid-body (posterior ventral mechanosensory (PVM) and two in the tail (left and right posterior lateral mechanosensory (PLML and PLMR)). To track the movement of all cell bodies, movies were captured at 50× magnification of SK4005 animals immobilized either by the anesthetic sodium azide (NaN_3) at concentrations 10 mM or by our microfluidic device. 10 mM NaN_3 was the highest anesthetic concentration that allowed recovery of the animals. The SK4005 strains express GFP under the mec4 promoter, which is expressed in the six touch neurons of *C. elegans*. At 50× magnification, 1-3 cell bodies were randomly selected and were visible in the movies. The fluorescence intensity in the movies was first thresholded to identify locations of high GFP expression, corresponding to the cell bodies. An algorithm next identified all connected regions and removed those too small to be cell bodies, then calculated the centroids of the remaining objects. The centroids were overlaid onto the original movies to ensure the cell bodies were properly identified. The results of tracking these cell bodies are shown in Figure 3-3b, which shows the histogram of the frame-to-frame displacement of the tracked centroids, and Figure 3-3c, which shows their mean drift over time. The movement of the immobilized animals is quite small, and is comparable to their motion even when deeply anesthetized. Despite being completely re-

strained externally, the animals can still have small internal movements, especially around the pharynx. However, such internal activity does not cause significant displacement of the neurons imaged, and high-resolution two-photon images near the pharynx were easily acquired.

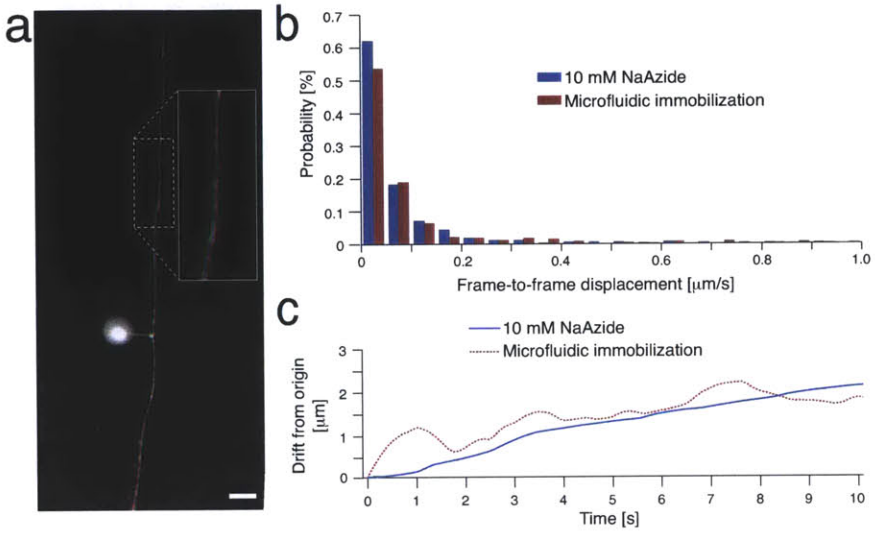

Figure 3-3: Quantitative and qualitative measurements of microfluidic immobilization. (a) Positional stability of a sub-cellular feature during microfluidic immobilization. Three images of the anterior ventral mechnosensory (AVM) neuron, its axon, and the PVM axon are taken at 5 s apart. These images are then colored red (earliest), green, and blue (latest) and overlaid on top of each other, such that the white regions indicate the overlap between all three images (scale bar 20 μm). Inset shows close-up of outlined area. (b)(c) Comparison of cell body movement during microfluidic immobilization versus deep anesthetic immobilization using 10 mM NaN_3. The centroids of the touch neuron cell bodies are tracked using a computer algorithm that analyzes data from movies taken at 20-30 Hz with 50× magnification. 12 microfluidically-immobilized animals and 9 anesthetized animals were tracked. (b) Histogram showing average displacement of cell bodies between frames divided by the time between frames. (c) Line plot showing mean drift of cell bodies over time.

3.3.2 Lifespan quantification

To check whether these devices affect the health of the animals being screened, the lifespans and brood sizes of 25 animals immobilized animals were tracked. Each animal was immobilized for 1 min using 15 PSI of pressure in the compression layer. Note that the pressure applied to the animals by the membrane is not the full 15 PSI, due to the resistance of the membrane to flexing. The immobilized population was compared to a control population that was not run through the device. Figure 3-4 shows the lifespans of both populations

(maintained at 20 °C). The mean lifespan of the immobilized population was 17.3 days (s.d. = 5.0 days) and 16.9 days for the control population (s.d. = 4.0 days). The Graphpad Prism software package was used to perform the log-rank (Mantel-Cox) test. The P-value is 0.8947, which suggests there is no statistically significant difference between the lifespans of the two populations. Both populations also produced normal brood sizes, and were free of axonal blebbing.

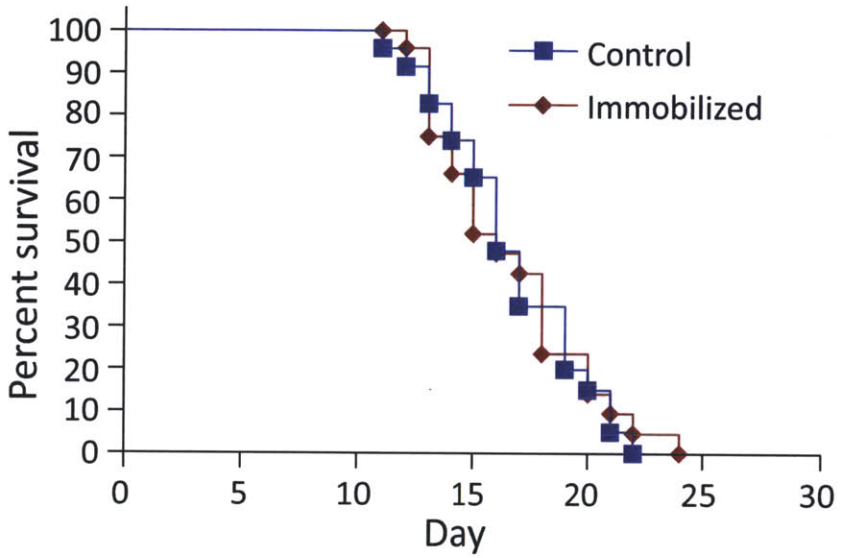

Figure 3-4: Lifespans of microfluidically-immobilized and control populations. The immobilized population consisted of 25 worms that were immobilized for one minute each, and the control population consisted of 23 worms that were not run through the device. Both populations were monitored once a day for dead animals, and surviving animals were transferred to a fresh plate. An animal was scored as dead if it did not respond to prodding with a platinum worm pick. The mean lifespan of the immobilized population was 17.3 days (s.d. 5.0 days), and the mean lifespan of the control population was 16.9 days (s.d. 4.0 days).

3.4 On-chip laser microsurgery and two-photon microscopy

The high immobilization stability achieved in these devices enables the use of a number of key optical techniques. To illustrate this we have chosen two methods that require repeatable, highly stable immobilization: multi-photon microscopy and femtosecond-laser nanosurgery. Multi-photon microscopy, including two-photon excitation fluorescence (TPEF) [30], is an important application that requires a very high degree of stabilization. Multi-photon microscopy is inherently non-linear, and thus has the ability to perform op-

tical sectioning with negligible out-of-plane absorption and emission. This dramatically reduces photobleaching and phototoxicity [31], which is especially significant in assays that require animals to be imaged at multiple time points. The advantages of multi-photon microscopy are offset by the requirement for live animals to be anesthetized, due to the long duration needed to capture an image. Our immobilization method can be used to successfully acquire two-photon images of non-anesthetized live animals using devices bonded to 175 µm-thin glass slide. The middle image of Figure 3-5 shows a volume reconstructions of a pmec4::gfp animal, obtained by a two-photon microscope scanning at 0.2 frames/s using a 40×/0.8 NA water-immersion objective. In this configuration, imaging a 120 µm × 120 µm × 30 µm volume required roughly two minutes of stable immobilization. Such non-invasive imaging of non-anesthetized animals can allow investigation of cellular processes sensitive to anesthesia, such as neural degeneration, regeneration and embryogenesis.

Femtosecond-laser micro/nanosurgery enables precision ablation of sub-cellular processes with minimal collateral damage [88]. This technique has been previously used study axonal regeneration in *C. elegans* [72, 73], which enables the use of a geneticaly amenable whole-animal model for screening factors affecting neural degeneration and regeneration. However, manually preparing an animal for surgery, imaging and recovering it afterwards are fairly laborious tasks. Furthermore, the effects of long-term anesthesia on these processes are not known. Using our immobilization technique, we can immobilize animals and perform femtosecond-laser nanosurgery repeatably, rapidly and precisely. The rightmost image of Figure 3-5 shows an SK4005 (pmec4::gfp) animal whose AVM axon has been cut. Our on-chip femtosecond-laser nanosurgery technique is a powerful tool for the discovery of potential drugs and genetic factors affecting neural degeneration and regeneration.

3.5 Discussion

Microfluidic immobilization using a compression layer is a rapid and highly repeatable technique for immobilizing small animals for imaging and manipulation of sub-cellular processes without anesthesia. The stability of this technique is comparable to that of deep anesthesia. It affects neither the lifespan nor brood size of the animals, and it does not induce hypoxia. This on-chip method can enable high-throughput screening of cellular and sub-cellular phenotypes in whole animals, as well as the use of precise techniques such as femtosecond-laser

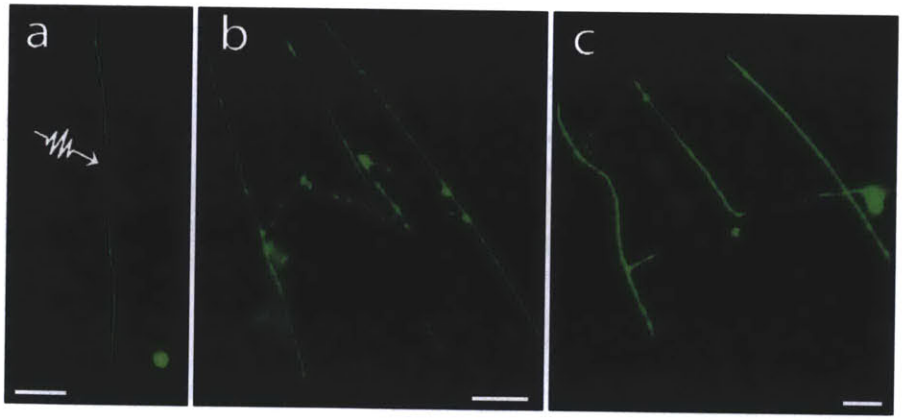

Figure 3-5: Microfluidic immobilization enables several key applications in live, un-anesthetized animals. (a) Successful axotomy of AVM process. 20 nJ femtosecond pulses were delivered using a MaiTai® Ti:Sapphire laser (Spectra-Physics) at a rate of 80 MHz to successfully cut the axons. Arrow indicates the focus of the laser and the axotomized region. (b), (c) Volume reconstruction of images captured using two-photon microscopy. (b) Head of mec4::gfp animal. (c) Posterior midbody of mec4::gfp animal and posterior ventral mechanosensory neuron (PVM). The left and right anterior lateral mechanosensory (ALML and ALMR) and AVM processes are clearly visible, as are the nerve ring branches that extend into multiple imaging planes (all scale bars 20 µm).

microsurgery and multi-photon microscopy on physiologically active animals. The next chapter discusses the use a microfluidic device based on this immobilization technique to perform a chemical screen for factors affecting neural regeneration.

Chapter 4

In vivo small-molecule screen for factors modulating neural regeneration[†]

Abstract

Discovery of molecular mechanisms and chemical compounds that enhance neuronal regeneration can lead to development of therapeutics to combat central nervous system injuries and neurodegenerative diseases. By combining high-throughput microfluidics and femtosecond laser microsurgery, we demonstrate for the first time large-scale *in vivo* screens for identification of compounds that affect neurite regeneration. We performed thousands of microsurgeries at single axon precision in the nematode *Caenorhabditis elegans* at a rate of 20 seconds per animal. Following surgeries, we exposed the animals to a hand-curated library of approximately one hundred small molecules, and identified chemicals that significantly alter neurite regeneration. In particular, we found that the PKC kinase inhibitor staurosporine strongly modulates regeneration in a concentration- and neuronal type-specific manner. Two structurally unrelated PKC inhibitors produce similar effects. We further show that regeneration is significantly enhanced by the PKC activator prostratin.

[†]**This chapter is an adaptation of the material found in [89]. Author contributions: C.S., C.B.R., C.L.G., and M.F.Y. designed research; C.S., C.B.R., and C.L.G. performed research; C.S., C.B.R., C.L.G., S.N., S.J.H., and M.F.Y. contributed new reagents/analytic tools; C.S. analyzed data; and C.S., C.B.R., and M.F.Y. wrote the paper.**

Key words: Caenorhabditis elegans, microfluidics, femtosecond laser microsurgery, neural regeneration, chemical screening, staurosporin, prostratin.

4.1 Motivation

The ability of neurons in the adult mammalian central nervous system to regenerate their axons after injury is extremely limited, which has been attributed to both extrinsic signals of the inhibitory glial environment [90] as well as intrinsic neuronal factors [91–93]. The discovery of cell-permeable small molecules that modulate axon regrowth can potentiate the development of efficient therapeutic treatments for spinal cord injuries, brain trauma, stroke, and neurodegenerative diseases. Identification of such molecules can also provide valuable tools for fundamental investigations of the mechanisms involved in the regeneration process. Currently, small-molecule screens for neuronal regeneration can only be performed in simple *in vitro* cell culture systems. *In vitro* cell culture screens have already produced large numbers of chemicals that enhance regeneration and/or affect cellular morphogenesis, yet many of these hits still remain untested *in vivo*. Most *in vitro* studies do not translate to animal models, and also fail to reveal off-target, toxic, or lethal effects. Thus, a thorough investigation of neuronal regeneration mechanisms requires *in vivo* neuronal injury models.

In vivo neuronal regeneration studies have been performed mainly in mice and rats. However, their long developmental periods, complicated genetics and biology, and expensive maintenance prevent large-scale studies in these animals. The nematode Caenorhabditis elegans (*C. elegans*) is a simple, well-studied, invertebrate model-organism with a fully mapped neuronal network comprising 302 neurons. Its short developmental cycle, simple and low-cost laboratory maintenance, and genetic amenability make it an ideal model for large-scale screens, rapid identification of the molecular targets of screened compounds, and discovery of novel signaling pathways implicated in regeneration.

Until recently however, the small size of *C. elegans* (~50 µm in diameter) prevented its use for investigation of neuronal regeneration mechanisms. We previously demonstrated femtosecond laser microsurgery as a highly precise and reproducible injury method for studying axon regrowth in *C. elegans* [72,73,94]. The non-linear multiphoton absorption of

the incident femtosecond pulse allows subcellular-resolution surgery of nematode neuronal processes with minimal out-of-plane absorption and collateral damage. Furthermore, due to the *C. elegans* stereotypic anatomy and hermaphroditic reproduction, the same neurons can be repeatedly axotomized at the same distance from the soma in isogenic animal populations, significantly enhancing reproducibility of assays. Recent low-throughput studies have used this technique to investigate how factors, such as animal age, neuronal type, synaptic branching, and axon guidance signaling, influence regeneration [74, 75]. In addition to screens on nematodes exhibiting spontaneous neurite breaks due to dysfunction of β-spectrin, this technique has also revealed that axon regrowth depends on the activity of MAP kinase pathways [76, 77].

However, neuronal regeneration in *C. elegans* is a highly stochastic process requiring large numbers of animals to be screened. The high motility of wild-type nematodes causes a significant throughput challenge. Precise laser axotomy and imaging at the cellular level require orientation and immobilization of animals. Traditional immobilization methods using anesthetics, such as sodium azide, levamisole and tricaine/tetramisole, have significant and/or uncharacterized effects on nematode physiology, which may affect the regeneration process [95]. In addition, anesthetics need several minutes to take effect, and recovery of nematodes from anesthesia requires exchange of media without losing animals, all of which are incompatible with high-throughput screening. Other techniques that can be used to reversibly immobilize *C. elegans* include trapping of nematodes in wedge-shaped microchannels [96], cooling [81, 97] and exposure to CO_2 [82, 98]. Wedge-shaped microchannels have not been shown to provide immobilization with sufficient stability to perform repeatably subcellular resolution manipulations, such as femtosecond laser microsurgery, and the physiological effect of exposure to low temperatures and CO_2 remain uncharacterized for many biological processes. In addition, none of these techniques have been scaled to handle large numbers of *C. elegans* for chemical or RNAi screens.

The previous chapter described non-invasive mechanical means to immobilize *C. elegans* for high-throughput *in vivo* imaging and femtosecond laser microsurgery. In order to facilitate large-scale screening of chemical libraries, we also developed a simple mechanism to transfer nematodes from multiwell plates to microfluidic chips for neurosurgery and imaging. In combination with the software we designed, we can load, image, and perform femtosecond laser microsurgery within $\sim$20 seconds per animal. We performed chemical

screens using thousands of animals to test a hand-curated library of approximately one hundred chemicals. We demonstrate that PKC kinases are involved in regeneration of *C. elegans* mechanosensory neurons. We also show that prostratin, a PKC activator, significantly increased neuronal regeneration.

4.2 Materials and methods

4.2.1 Nematode handling

Nematodes were grown at 15 °C in NGM agar plates, unless otherwise mentioned. Standard procedures were followed for *C. elegans* strain maintenance and genetic crosses [99]. Nematode strains used in this study include those given in Table 4.1.

Table 4.1: Strains used in this chapter

Strain Name	**Genotype**
BZ555	*egIs1*[$p_{dat\text{-}1}$GFP]
CX3553	*lin-15B(n765)kyIs104*[$p_{str\text{-}1}$GFP]X
EG1285	*lin-15B(n765)oxIs12*[$p_{unc\text{-}47}$GFP]X
MT1522	*ced-3(n717)*IV
SK4005	*zdIs5*[p_{mec-4}GFP]I
not named	*zdIs5*[p_{mec-4}GFP]I;*ced-3(n717)*IV

4.2.2 Chemical treatments

The small molecule library used in the chemical screening was prepared from initial compound stock plates with small molecule concentrations ranging from 5-10 mM. By consecutive dilutions in 100% dimethyl sulfoxide (DMSO, Sigma Aldrich) and transfers using the Cybi®-Well vario 384/35 µl Head, daughter plates were created, heat sealed and stored at -20 °C, in order to be used on the day of the screening. Compound concentrations in the daughter plates ranged from 2-4 mM. One day prior to laser microsurgeries, *Escherichia coli* (*E. coli*) OP50 bacteria were inoculated in Luria-Bertani (LB) media and grown overnight.

Subsequently, the *E. coli* culture was washed with M9 buffer and bacteria were resuspended in nematode growth media (NGM). For the compound library screens, 55 µl of the NGM resuspended bacterial culture was added to 0.55 µl of DMSO-dissolved compound library. After thorough mixing, 50 µl of the compound-containing NGM culture was further diluted, by adding 50 µl of NGM resuspended bacterial culture, so that the final DMSO concentration was 0.5% and the small molecule concentrations ranged from 10-20 µM. Control cases contained either 0.5% DMSO or bacterial culture alone. For each library-compound a total of 10-20 animals were tested. For the kinase effector treatments, axotomized animals were incubated at 20 °C with 10-100 µM dibutyryl-cAMP, H-89, LY-294,002, PD 98,059, staurosporine, wortmannin, Y-27632, chelerythrine, Gö 6983 or prostratin (Sigma Aldrich) in liquid NGM cultures supplemented with *E. coli* OP50 bacteria, and transferred into fresh cultures every 24 h. For control experiments in treatments with LY-294,002, PD 98,059, staurosporine, wortmannin, chelerythrine, Gö 6983, and prostratin, which were dissolved in DMSO, liquid NGM was also supplemented with the respective amount of DMSO. Each experiment was repeated at least three times.

4.2.3 Femtosecond laser microsurgery

Synchronized L4 nematodes were brought into the chip and immobilized. A Mai-Tai® HP (Spectra-Physics) femtosecond laser beam with 800 nm wavelength and 80 MHz repetition rate was delivered to a Nikon Ti microscope. ALM axons were axotomized by pulses with 10 nJ energy for 3.2 ms using a 20× objective lens with NA=0.75. For the control kinase modulator assays, synchronized L3, L4 or young adult nematodes were immobilized in 2% agarose pads with 0.1-1% 1-phenoxy-2-propanol. Neurites of mechanosensory, GABAergic and AWB or CEP neurons were axotomized by 7 nJ, 9.5 nJ and 11 nJ energy pulses respectively for 1.5 ms, with a 780 nm laser beam at 80 MHz repetition rate.

4.2.4 Data collection and analysis

48-120 h following axotomy, animals were imaged at the area of surgery with a Nikon Ti microscope. The length of the longest regrowing neurite and type of regeneration were scored using a MATLAB program. The percent regeneration versus the control indicated the percent difference from the mean value of the control. Statistical analysis was performed using a two-tailed Student's t-test.

4.3 Preliminary screening

To enable chemical screens, we made several modifications to the microfluidic *C. elegans* sorter technology described in the previous chapters (Figure 4-1 a). To incubate large numbers of animals in chemical libraries, we used multiwell plates, which are compatible with standard liquid handling technologies. We developed a method to rapidly, reliably, and repeatedly transport animals to and from standard multiwell plates containing chemicals into our sorter chips (Figure 4-1b). The multiwell plates are kept at an angle, and a metal tube is inserted into a well until it reaches near the well bottom. Since the animals settle near the well bottom, this allows rapid aspiration of animals without fluid being completely drained out of the wells. The channel array of the microfluidic sorter chip is used to rapidly load the animals into the main screening chamber (Figure 4-1c, step 1). Multiple animals are brought into the main chamber, and unwanted elements such as air bubbles or debris also enter occasionally. To capture an individual animal, the single aspiration port of the chamber is activated (Figure 4-1c, step 2). The rest of the animals in the chamber are flown back towards the input (Figure 4-1c, step 3) by brief application of a small pressure difference from the channel array. During this period, debris and air bubbles (which adhere more strongly to the chip surfaces) remain in the chamber. Next, by switching an off-chip valve, a stronger pressure pulse is applied to move debris or bubbles to the waste output (Figure 4-1c, step 4) while the single aspiration port tightly holds the animal in the chamber. Subsequently, all on-chip valves surrounding the main chamber are closed, isolating the single animal. The animal is then released from the single aspiration port, and aspirated towards the channel array (Figure 4-1c, step 5). This orients the animal linearly, making it easy to image and perform laser microsurgery. To increase the stability of immobilization, the channel above the chamber is then pressurized, pushing the thin immobilization membrane downwards (Figure 4-1a and d). This fully constrains the animal motion for imaging and surgery. Once the animal is immobilized, the microscope and camera configuration automatically switches to high-resolution acquisition. We developed a simple software interface to quickly target the laser to the surgery position at a pre-set surgery distance from the soma of the neuron. The software requires the user to make only two mouse clicks to perform the entire surgery operation: The user first clicks on the soma of the neuron to be axotomized. The software then draws a circle centered on the

soma where the radius of the circle is equal to the set surgery distance. The user next clicks on the intersection of the circle and the axon, which is the desired surgery location (Figure 4-1e). The software automatically moves the laser target to this surgery position, and performs the surgery. These enhancements significantly increase the throughput of our system: Our system can process animals within ~20 seconds on average, including off-chip loading and unloading of animals (Figure 4-1f). This is significantly faster than the time previously reported for automated ablation of entire cell bodies alone (which requires less surgical precision) [100].

Using this technology, we screened *C. elegans* for regenerative effects upon exposure to a chemical library enriched for compounds that may affect neurite outgrowth *in vitro* in mammalian cell cultures [101,102]. The potential targets of the small-molecule library that we screened included various kinases, cytoskeletal proteins, endocytic vesicle trafficking components, and nuclear processes (Figure 4-3a). Such use of chemicals with *a priori* known targets facilitates delineation of molecular mechanisms involved in regeneration. To test the effects of these compounds on regeneration we axotomized mechanosensory neurons of *C. elegans*. These neurons have been used extensively for investigation of neurodegeneration in connection with human diseases [103,104]. They grow long axonal processes devoid of any lateral branches, enabling highly precise microsurgery and subsequent imaging and characterization of outgrowing processes. Axotomies were performed on ALM mechanosensory neurons at larval stage 4 (L4) nematodes, approximately 200 µm away from the cell body. Following microsurgery animals were incubated in the presence of small molecules at concentrations ranging from 10-20 µM. Neurite regeneration was assessed 72 h post axotomy by measuring the length of the regrowing processes (Figure 4-3b). Figure 4-3a shows a classification of the library compounds, and the percentage of chemicals in each group that led to significant regeneration effects (i.e. $P \leq 0.05$ in Student's t-test). The compounds screened, the number of animals treated with each compound, the effects on regeneration, and the statistical significances are provided in Figure 4-2 and Tables 4.2 and 4.3.

Our preliminary screen identified a number of chemical compounds that significantly altered axon regeneration ($P < 0.05$ in Student's t-test). The compound category containing modulators of protein kinase function, such as staurosporine, wortmannin, LY294,002, H89, W7, PD 98,059, 50-E12 and dibutyryl-cAMP, exhibited the highest percentage of significant regeneration effects (Figure 4-1b). This observation, in conjunction with the recent studies

implicating specific kinases in the regeneration of nematode GABAergic and motor neurons [76, 77] prompted us to further investigate the effects of kinase modulators in *C. elegans* neurite regeneration.

4.4 Secondary screening

From our preliminary screen, we identified a number of chemical compounds that significantly altered axon regeneration ($P \leq 0.05$), among which were modulators of protein kinase activity (Figure 4-3a). This observation, in conjunction with studies implicating specific MAP kinases in the regeneration of nematode GABAergic motor neurons [76, 77], prompted us to further investigate the effects of kinase modulators in *C. elegans* neurite regeneration. We investigated the effects of this compound class on regeneration of PLM neurons since regrowing ALM neurons pass near or through the dense and complex neuronal circuitry of the nerve ring, and occasionally interact with its components, complicating analysis and interpretation of the results.

By performing laser axotomy on PLM mechanosensory neurons, we analyzed the effects of all the commercially available kinase modulators from our initial chemical library, which included staurosporine, wortmannin, LY294,002, H89, W7, PD 98,059, 50-E12, Y-27632 and dibutyryl-cAMP (Figure 4-3c and Table 4.4). Known targets of these compounds are shown in Table 4.4. Compounds were tested on late larval stage and young adult nematodes, at concentrations ranging from 10 to 100 µM (Figure 4-3c and Table 4.4). Staurosporine, a non-selective kinase inhibitor with high affinity for protein kinase C (PKC) [105], exhibited the strongest effects. Staurosporine administered at a concentration of 10 µM caused approximately a three-fold decrease in the regrowth of PLM neurons 48 h after axotomy, whereas concentrations lower than 5 µM did not exhibit any significant effect (Figure 4-5). The effect was similar in L4 and young adult animals (44.25 ± 7.47 vs. 112.86 ± 9.23 µm, $P = 2.89\times10^{-7}$ in L4 animals, 44.15 ± 6.23 vs. 89.32 ± 7.11, $P = 3.20\times10^{-5}$ in young adults) (Figure 4-4). In early larval stages, 0.5% DMSO (solvent for staurosporine) was toxic; however the few surviving L3 nematodes also exhibited decreased regrowth and strong morphological abnormalities. Although toxicity of DMSO is a limitation for using chemical libraries on young larvae, 0.5% DMSO is not toxic to either young adults or older animals.

Interestingly, the effect of staurosporine administration was specific to the neuronal type; although it affected PLM touch neurons, it did not alter regeneration of the ALM touch neurons, D-type GABAergic motor neurons, CEP dopaminergic neurons, or AWB olfactory neurons (Figure 4-5b). Given that only the posteriorly located PLM neurons exhibited sensitivity to staurosporine, this differential effect could be attributed to physical barriers preventing staurosporine from reaching more anterior parts of the *C. elegans* body. To investigate this possibility, we took advantage of the GABAergic neurons found along the nematode body. In contrast with its effect on PLM neurons, staurosporine did not alter significantly the regrowth of axotomized posterior GABAergic motor neurons, nor did it cause any difference in the response among GABAergic motor neurons in the posterior-, anterior- or mid-body of animals (Figure 4-5d). These observations suggest that different types of neurons have different molecular requirements for regeneration. This is true even for neurons with highly similar structure and functions, such as ALMs and PLMs, both of which extend long processes along the nematode body and are required for mechanosensation (Figure 4-5b and c).

Regenerating neurites in animals treated with staurosporine often exhibited large terminal retraction bulbs and swellings along the axon (Figure 4-5c). Such structures were observed mainly in the axotomized neurites of treated animals, and only rarely in non-treated animals. Since staurosporine is known to induce apoptosis at high concentrations [106–109], we investigated whether these swellings are an indication of apoptotic response, and whether staurosporine's effect on regeneration is related to the activation of apoptotic pathways. Initiation of apoptosis in *C. elegans* requires CED-3, a cysteine protease of the interleukin-1 -converting enzyme (ICE) family [106, 110]. *In vitro* mammalian cell culture assays have demonstrated the requirement of this family of caspases (ICE / CED-3 protease family) for the execution of staurosporine-induced apoptotic cell death [110, 111]. We tested staurosporine on a ced-3 mutant genetic background and observed no significant difference in regeneration compared with wild-type animals (Figure 4-6a). In addition, Hoffman imaging of nematodes from 24 to 120 h after laser axotomy did not show any apoptotic body formation in staurosporine-treated animals. 5 days after axotomy, the cell bodies of the injured neurons still exhibited normal morphology and strongly expressed GFP (Figure 4-6b).

While staurosporine can induce apoptosis at high concentrations, at lower concentrations it has been shown to inhibit the protein kinases PKC, PKA, PKG, CAMKII and MLCK,

as well as other kinases in a concentration-dependent manner, and to stimulate K-Cl co-transport in red blood cells [105,112–114]. Since staurosporine's strongest inhibitory effect is on PKC kinases, and in *C. elegans* it has been shown to inhibit PKC activity [115], we tested whether it exerts its effects on regrowing neurites via the inhibition of this particular kinase. To this end, subsequent to laser microsurgery of PLM neurites, we incubated nematodes in the presence of the two distinct structural classes of specific PKC inhibitors chelerythrine or Gö 6983 [116,117]. Treatment of axotomized animals with either chelerythrine or Gö 6983 at concentrations between 10 and 100 µM also significantly reduced regeneration (70.40 ± 8.20 vs. 123.35 ± 7.86 µm, $P = 2.65\times10^{-5}$ for chelerythrine, and 99.83 ± 8.28 vs. 128.65 ± 9.10 µm, $P = 0.023$ for Gö 6983) (Figure 4-7). Conversely, the PKC activator prostratin significantly increased regeneration of PLM neurites (145.25 ± 7.46 vs. 114.68 ± 8.88 µm, $P = 0.01$) (Figure 4-7). Treatment with specific inhibitors of other targets of staurosporine had no effect (Figure 4-8). In combination, the above results strongly suggest that PKC kinases are involved in the regeneration of *C. elegans* mechanosensory neurons. Although we cannot exclude contribution of other pathways to the inhibitory effect of staurosporine, these pathways likely do not involve PKA signalling (also targeted by staurosporine), since we did not observe any effect of the PKA-modulators db-cAMP and H-89 on regeneration (Figure 4-3c and Table 4.4). Four *pkc* genes have been identified in *C. elegans*: *tpa-1*, *pkc-1*, *pkc-2* and *pkc-3*, which span the all *pkc* subfamilies (Figure 4-9a). Genetic inactivation of the conventional PKCs (*pkc-2*) inhibited PLM regeneration, however inactivation of the novel PKCs (*pkc-1* and *tpa-1*) did not significantly affect regeneration (Figure 4-9b).

4.5 Discussion

We demonstrated here, for the first time, the use of laser microsurgery and microfluidic technologies for *in vivo* screening of chemicals affecting neuronal regeneration. We developed a simple and robust technique to load nematodes from and dispense to standard multiwell plates. This allowed use of standard technologies for incubation of large numbers of animals in chemicals while utilizing the manipulation capabilities of our microfluidic chips. In combination with software we developed, we were able to load, image, and perform single-axon-precision surgeries within ~20 seconds. Screening a chemical library of small molecules indicated the involvement of specific kinase pathways in neurite regrowth after

injury in *C. elegans*. We found that the kinase inhibitor staurosporine suppresses regeneration in a neuronal type-specific manner. In addition, we showed that axonal regeneration of neurons is significantly enhanced after administration of a PKC activator. Our results are consistent with *in vitro* studies on goldfish retina explants [118], on adult frog sciatic sensory axons [119], on post-natal mice retinal ganglion cells [120], and on adult mice sensory ganglia [121], wherein the administration of PKC inhibitors following mechanical lesion blocks neurite outgrowth. This indicates the existence of conserved neuronal regeneration mechanisms between nematodes and vertebrate organisms. However, other *in vitro* studies have yielded conflicting data regarding the involvement of PKC kinase in the inhibitory effects of staurosporine on neuronal regeneration [122, 123]. By performing regeneration studies on whole organisms, we showed for the first time *in vivo* that staurosporine blocks regeneration at least partially by inhibiting PKC. We also showed that other kinase inhibitors of PI3K, PKA, MAPKKK, and ROCK did not affect regeneration in a neuron type that is otherwise strongly affected by staurosporine. However, these kinase inhibitors affect neurite growth in other experimental models [124–128]. The lack of response to these other types of kinase inhibitors could be due to the differences among neuronal types, the ineffectiveness of these chemicals, or the absence of an inhibitory myelin sheath in *C. elegans*.

Many chemicals have been found to modulate neurite growth *in vitro*. However, validation of these effects *in vivo* and identification of their mechanisms of action have remained elusive due to the lack of large-scale screening platforms for genetically amenable animal models. The advantages of *C. elegans* genetics and our high-throughput screening technology should allow in the future discovery of novel molecular pathways required for neuronal regeneration. Further experiments on higher organisms will show which of these mechanisms are conserved in mammals, and may provide means for pharmaceutical or genetic interventions to combat human diseases and injuries.

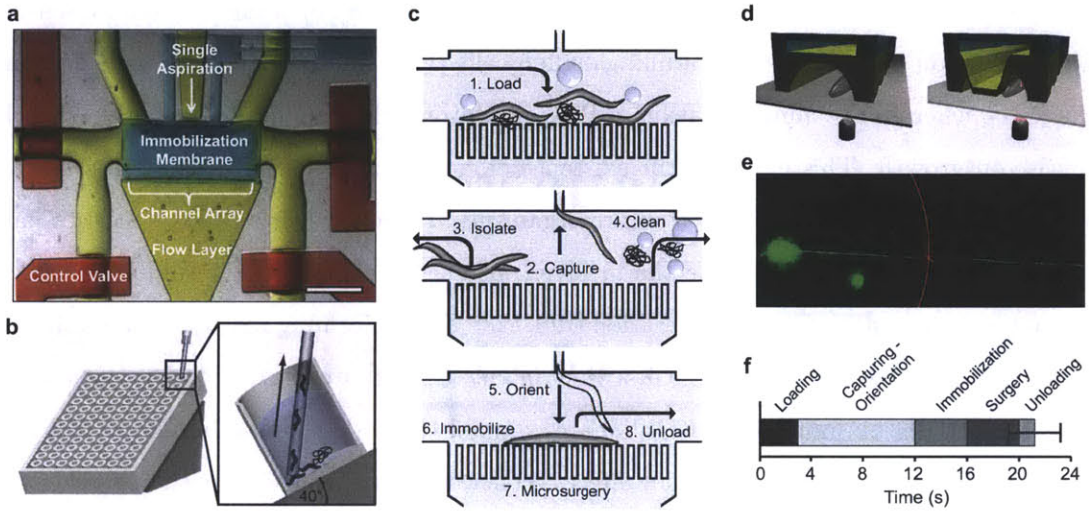

Figure 4-1: Microfluidic *C. elegans* manipulation for subcellular laser microsurgery and chemical library screening. (a) Micrograph of dye-filled microfluidic chip. Red: Control (valve) layer, yellow: Flow layer, blue: Immobilization layer. Scale bar: 1 mm. (b) Animal loading from multiwell plates. The multiwell plate is held at a 40° angle and a stainless steel tube is inserted to the well bottom. (c) Microfluidic *C. elegans* manipulation steps. **1**. Loading of nematodes. Dust, debris, air bubbles, and bacteria may also enter the chip. **2**. Capture of a single animal by the single aspiration channel. **3**. Isolation of a single animal within the chamber by low-pressure washing of the channels to remove and recycle the rest of the nematodes. **4**. Cleaning of channels by high pressure washing to remove debris and bubbles. **5**. Orientation of the single animal by releasing it from the single aspiration port and recapturing it by the channel array. **6**. Immobilization by pressurizing a thin membrane (see panel d). **7**. Laser microsurgery (see part e). **8**. Unloading of the animal from the chip after surgery. (d) Illustration of the final immobilization process. Once a single animal is captured and linearly oriented (i), a channel above the main chamber is pressurized pushing a thin membrane downwards (ii). The membrane wraps around the animal, significantly increasing immobilization stability for imaging and surgery. Precise laser targeting of subcellular features is achieved using a femtosecond laser tightly focused inside the *C. elegans* body by a high numerical aperture objective lens (see Section 4.2.3). (e) Software interface to accelerate axon targeting for laser axotomy. A right mouse click on the cell body is used to identify the portion of the axon a set distance from the soma, and a left mouse click moves this location to the laser focal point. (f) Average time per animal for screening steps. Total time per animal is from 3 independent experiments each with 100 worms.

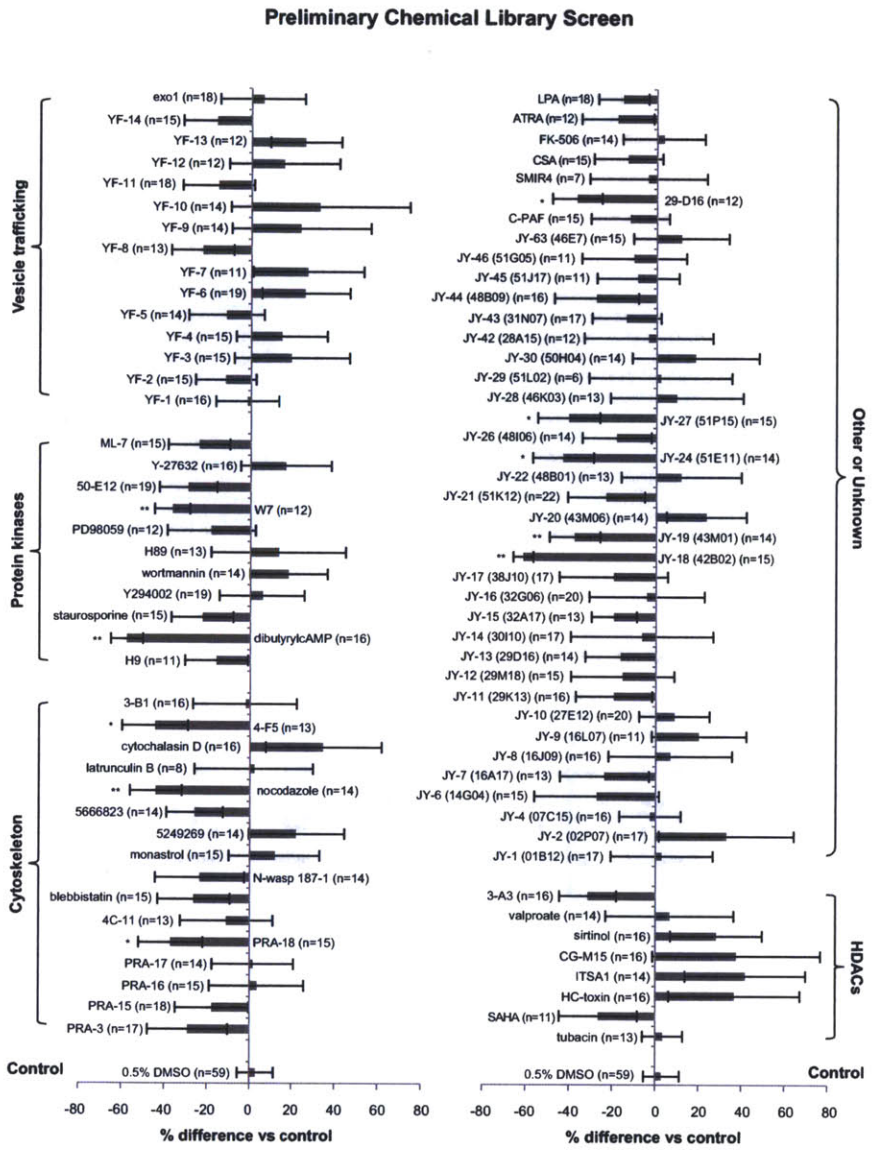

Figure 4-2: Preliminary screen of a hand-curated chemical library for effects on regeneration of *C. elegans* mechanosensory neurons. ALM neurons of L4 animals were axotomized approximately 200 µm away from the cell body and incubated for 72 h in the presence of chemical library compounds. Maximum regrowth lengths were measured and the percent differences to the respective controls were calculated for each experiment. Bars represent the total mean values from all experiments (*, $P \leq 0.05$; **, $P \leq 0.01$), error bars denote s.e.m., and n indicates the total number of animals used in each case.

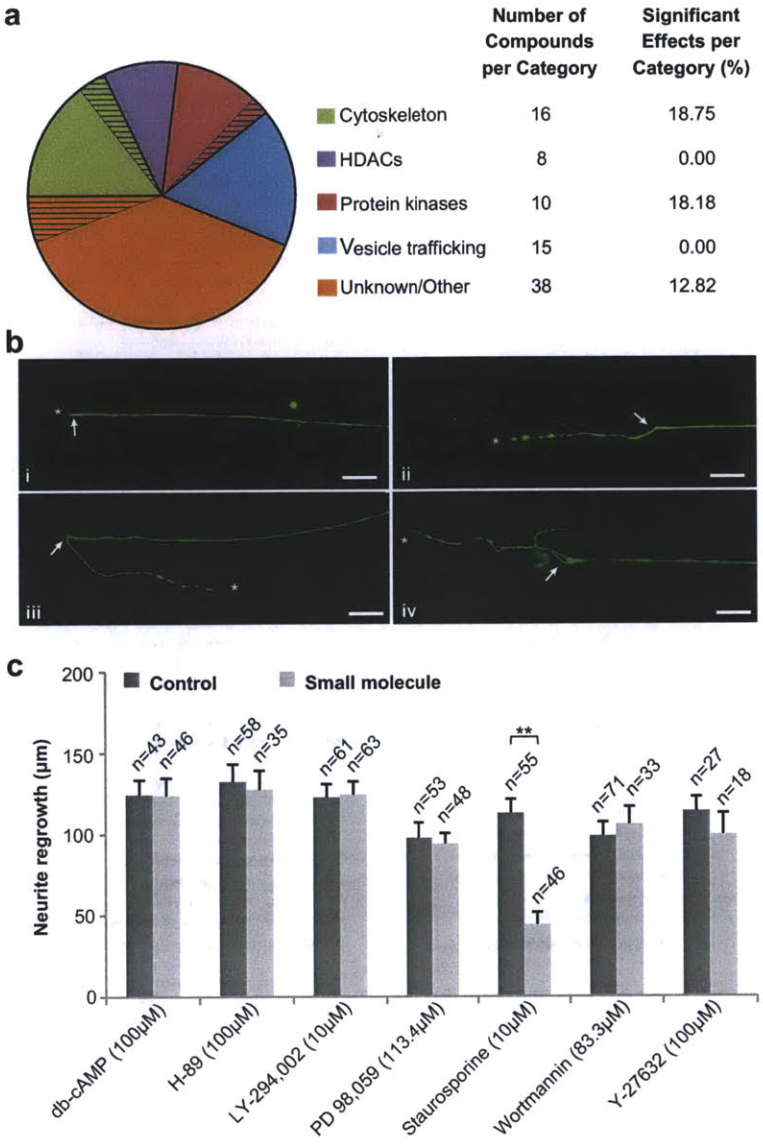

Figure 4-3: *In vivo* chemical screen for small molecules affecting axonal regeneration. (a) Primary target-categories of the screened compound library. The dashed parts of the pie chart represent the percentage of compounds in each category affecting regeneration. (b) Common regeneration phenotypes observed 72 h following axotomy and compound exposure: (i) No axon regrowth, (ii) forward regrowth, (iii) backward regrowth, and (iv) regrowth with branching. Arrows and asterisks indicate start and end points of regenerated axons respectively. For regrowth with branching, indicated start and end points are for the longest regrown branch. Scale bars: 20 µm. (c) Effects of protein kinase modulators in the regeneration of PLM neurites after laser axotomy. PLM neurons of L4 nematodes were axotomized 50 µm away from the cell body. Animals were incubated in the presence of kinase modulators for 48 h, and the lengths of the longest regrowing neurites were measured (**, $P \leq 0.01$). Error bars denote the s.e.m., and n indicates the total number of animals used in each case, while the bars show one representative screen with its controls.

Table 4.2: Chemical library of small molecules screened for effects on neuronal regeneration in *C. elegans* part 1: Major compound categories. The names of the small molecules used in our preliminary chemical library screen are listed along with their respective target category and molecular structure. Chemical structures are represented by SMILES (Simplified Molecular Input Line Entry Specification)

Target Category	Name	Molecular Structure
Vesicle trafficking	YF-1	OC(C=C1)=C(OC)C=C1/C=N/NC2=NC=NC3=C2C(CCCC4)=C4S3
	YF-2	O=C(N/N=C/C1=CC=CO1)C2C(C3=CC=CC=C3)(C4=CC=CC=C4)C2
	YF-3	O=C(NC1=CC=CC=C1)NNC2=CC=C(C=C2N)[N+]([O-])=O
	YF-4	O=S(NC(C(C(NC1=CC(Cl)=C(Cl)C=C1)=O)=C2)=CC=C2Cl)(C3=CC=CC=C3)=O
	YF-5	O=S(NC1=C(C=C(Br)C=C1)C(NC(C(C(C2=CC=C(Cl)C=C2)=O)=C3)=CC=C3Cl)=O)(C4=CC=C(Cl)C=C4)=O
	YF-6	O=C(OC1=C(C2=CC(OC)=C(OC)C=C2)[NH+]=CC=C1)C3(CC4C5)CC5CC(C4)C3
	YF-7	CC(C)(C)C(C=C1)=CC=C1CCC2OCC(CN3CCCCC3)O2
	YF-8	O=C(CC1=CC=CC=C1)N/N=C/C2=CC=C(C(C=C3Cl)=CC=C3C)O2
	YF-9	O=C(N/N=C/C1=CC=C(C=C1)C(C)(C)C)COC(C(Cl)=C2)=C(Cl)C=C2Cl
	YF10	O=C(C1=CC=NC=C1)/C=C/C2=CNC3=CC=C(Br)C=C23
	YF-11	ClC1=C(C=CC=C1)/C=N/NC2=NC(NCC3=CC=CC=C3)=NC(N4CCOCC4)=N2
	YF-12	IC1=CC=CC(/C=N/NC2=NC(N(C3=CC=CC=C3)C4=CC=CC=C4)=NC(N5CCOCC5)=N2)=C1
	YF-13	O=C(N/N=C\C1=CC=CC=C1O)C2=C(OC)C=C3C=CC=CC3=C2
	YF-14	O=C(C1=C2C=CC=C1)C3=C2N=NC(C4=CN=CC=C4)=C3
	Exo-1	COC(=O)C1=CC=CC=C1NC(=O)C2=CC=C(C=C2)F
Protein kinases	H-9	C1=CC2=C(C=CN=C2)C(=C1)S(=O)(=O)NCCN
	Dibutyryl camp (db cAMP)	CCCC(=O)NC1=NC=NC2=C1N=CN2C3C(C4C(O3)COP(=O)(O4)O)OC(=O)CCC
	Staurosporine	CC12C(C(CC(O1)N3C4=CC=CC=C4C5=C6C(=C7C8=CC=CC=C8N2C7=C53)CNC6=O)NC)OC
	LY29002	C1COCCN1C2=CC(=O)C3=C(O2)C(=CC=C3)C4=CC=CC=C4
	Wortmannin	CC(=O)OC1CC2(C(CCC2=O)C3=C1C4(C(OC(=O)C5=COC(=C54)C3=O)COC)C)C
	H89	C1=CC2=C(C=CN=C2)C(=C1)S(=O)(=O)NCCNCC=CC3=CC=C(C=C3)Br
	PD98059	COC1=CC=CC(=C1N)C2=CC(=O)C3=CC=CC=C3O2
	W7	C1=CC2=C(C=CC=C2Cl)C(=C1)S(=O)(=O)NCCCCCCN
	50-E12	C1(C2=CC=NC=C2)=CNC3=C1C=CC=C3
	Y-27632	CC(C1CCC(CC1)C(=O)NC2=CC=NC=C2)N
	ML-7	C1CNCCN(C1)S(=O)(=O)C2=CC=CC3=C2C=CC=C3I
HDACs	Tubacin	C1C(OC(OC1C2=CC=C(C=C2)CO)C3=CC=C(C=C3)NC(=O)CCCCCCC(=O)NO)CSC4=NC(=C(O4)C5=CC=CC=C5)C6=CC=CC=C6
	SAHA	C1=CC=C(C=C1)NC(=O)CCCCCCC(=O)NO
	HC-toxin	CC1C(=O)NC(C(=O)N2CCCC2C(=O)NC(C(=O)N1)C)CCCCCC(=O)C3CO3
	ITSA-1	C1=CC=C2C(=C1)N=NN2C(=O)C3=C(C=C(C=C3)Cl)Cl
	CG-M15	OC1=C(C2=CC=CC=C2C=C1)/C=N/C3=CC=C(OC)C=C3[N+]([O-])=O
	Sirtinol	CC(NC(C1=CC=CC=C1/N=C/C2=C(O)C=CC3=CC=CC=C23)=O)C4=CC=CC=C4
	Valproate	CCCC(CCC)C(=O)[O-]
	3-A3	O=C1OC2=C(CCC=C2)C3=C1C4=CC(O)=C(O)C=C4O3
Cytoskeleton	PRA-3	O=C(O[C@H](C1=CC=CC=C1)[C@@H](C)N(C)C(CC/C=C/2)=O)[C@@]3([H])[C@]2([H])O[C@@]4([C@]53[H])[C@](C(N(CC6=CC=CC=C6)CC=C4)=O)([H])N(CC7=CC=C(OC)C=C7)C5=O
	PRA-15	O=C([C@@]1([H])[C@](C=C[C@H]2[C@@]3([H])C(O[C@@H](C4=CC=CC=C4)[C@H](C)N(C(CCC=C)=O)C)=O)(O2)[C@@]3([H])C(N1CC5=CC=C(OC)C=C5)=O)N(CC=C)CC6=CC=CC=C6
	PRA-16	O=C([C@]1([H])[C@@](C=C[C@@H]2[C@]3([H])C(O[C@H](C4=CC=CC=C4)[C@@H](C)N(C(CCC=C)=O)C)=O)(O2)[C@]3([H])C(N1CC5=CC=C(OC)C=C5)=O)N(CC=C)CC6=CC=CC=C6
	PRA-17	O=C([C@@]1([H])[C@](C=C[C@H]2[C@@]3([H])C(O[C@H](C4=CC=CC=C4)[C@@H](C)N(C(CCC=C)=O)C)=O)(O2)[C@@]3([H])C(N1CC5=CC=C(OC)C=C5)=O)N(CC=C)CC6=CC=CC=C6
	PRA-18	O=C(O[C@@H](C1=CC=CC=C1)[C@H](C)N(C)C(CC/C=C/2)=O)[C@@]3([H])[C@]2([H])O[C@@]4([C@]53[H])[C@](C(N(CC6=CC=CC=C6)CC=C4)=O)([H])N(CC7=CC=C(OC)C=C7)C5=O
	4-C11	C[C@]12C(CC(O[Si](C)(C)(C)C)C)CC2)=CC=C3C1CC[C@@]4(C)C3CC[C@@]4(O)CNCC5=CC=CC=C5
	Blebbistatin	CC1=CC2=C(C=C1)N=C3C(C2=O)(CCN3C4=CC=CC=C4)O
	N-Wasp 187-1	cyclo(LKDFDPDFLFDPLQ)2
	Monastrol	CCOC(=O)C1=C(NC(=S)NC1C2=CC(=CC=C2)O)C
	5249269	CCOC(C1=C(C)NC(NC1C2=CC=C(O)C=C2)=S)=O
	5666823	S=C1NC(C)=C(C(OCC)=O)C(C2=CC=CC(OC)=C2)N1
	Nocodazole	COC(=O)NC1=NC2=C(N1)C=C(C=C2)C(=O)C3=CC=CS3
	Latrunculin B	CC1CCC2CC(CC(O2)(C3CSC(=O)N3)O)OC(=O)C=C(CCC=C1)C
	Cytochalasin D	CC1CC=CC2C(C(=C)C(C3C2(C(C=CC(C1=O)(C)O)OC(=O)C)C(=O)NC3CC4=CC=CC=C4)C)O
	4-F5	CCCCNC(C1=CC(OC(C)=O)=C(C#C[Si](C)(C)C)C=C1)=O
	3-B1	BrC1=C[C@H]2C(C3=CC=CC=C3)C[C@@H]1[C@@]4(CO4)C2=O

Table 4.3: Chemical library of small molecules screened for effects on neuronal regeneration in *C. elegans* part 2: Minor or unknown compound categories. The names of the small molecules used in our preliminary chemical library screen are listed along with their respective target category and molecular structure. Chemical structures are represented by SMILES (Simplified Molecular Input Line Entry Specification)

Target Category	Name	Molecular Structure
Other or unknown	JY-1 (01B12)	NC1=CC=C(NCC)C(C)=C1C
	JY-2 (02P07)	O=C(C(C)(C)O)/C=C/C1=CC=CC=C1
	JY-4 (07C15)	O=C(NC1=NN(C2=CC=CC=C2)C=C1)C(Cl)(Cl)Cl
	JY-6 (14G04)	CC1=CC2=C(C=C1)NC3=C2CCCC3NCC4=CC=CC=C4
	JY-7 (16A17)	OC(COC1=CC=C(C=C1)C(C)C)CNC2CC(C)(C)NC(C)(C)C2
	JY-8 (16J09)	CN1CCN(CC1)C(C=C2)=CC=C2NC3=C(C=CC=C4)C4=NC5=C3C=CC=C5
	JY-9 (16L07)	O=S1(CC(CC1)N(C)C(SNC(C=C2)=C(C=C2[N+]([O-])=O)[N+]([O-])=O)=S)=O
	JY-10 (27E12)	O=C(NC1=CC=C(C(Cl)=C1)Cl)C(C2=CC=CC=C2)(O)C3=CC=CC=C3
	JY-11 (29K13)	O=S(C1=NC(C=CC=C2)=C2S1)(C(C=C3)=C(Cl)C=C3[N+]([O-])=O)=O
	JY-12 (29M18)	[O-][N+](C(C=C(OCO1)C1=C2)=C2C(N3CC4=CC=CC=C4)N(CC3)CC5=CC=CC=C5)=O
	JY-13 (29D16)	S=C(N)N/N=C(C1=C2C=CC=C1)/C(C2=N3)=NC4=C3C=CC=C4
	JY-14 (30I10)	O=S(C(C=C1)=CC=C1Cl)(CCC(C)=O)=O
	JY-15 (32A17)	[O-][N+](C(C=C1)=CC=C1C(OC2=C(CNC(C3=CC=CC=C3)=O)C(Cl)=C(Cl)C=C2Cl)=O)=O
	JY-16 (32G06)	[O-][N+](C1=C2C=CC=C1)=C(C=C2)/C=C/C3=CC=CC=C3
	JY-17 (38J10)	O=C1C2=C(CCC1Br)C(C(OCC)=O)=C(NC(CC)=O)S2
	JY-18 (42B02)	[H]C1(NCCC2=CC=CC=C2)C3=C(CCC1)C(C=C4C5CCCCC5)=C(C=C4)N3
	JY-19 (43M01)	OC(C=C1)=CC=C1\C=C/NC2=NC(C3=CC=CC=C3)=CC(C4=CC=CC=C4)=N2
	JY-20 (43M06)	O=C1C(C)=CC(N1CCC2=CNC(C=C3)=C2C=C3OCC4=CC=CC=C4)=O
	JY-21 (51K12)	[O-][N+]1=C2C(C=C(NC(C=C3)=CC=C3OC)C=C2)=NC14CCCCC4
	JY-22 (48B01)	C1(N2N=CC=C2)=NC(C3=CC=CC=C3)=CC(C4=CC=CC=C4)=N1
	JY-24 (51E11)	CC(NC1=CC=CC(C2=NC(C3=CC=CC=C3)=NC(C4=CC=CC(NC(C)=O)=C4)=C2)=C1)=O
	JY-26 (48I06)	O=C(CC)OC1(C2=CC=CC=C2)CC(N(C)CC1C)(C)C
	JY-27 (51P15)	O=C(CNC1CCCCC1)C2=CC(O)=C(O)C=C2
	JY-28 (46K03)	O=C(C)OC(CCC1)C2C1NCCC2
	JY-29 (51L02)	O=C1N(C)C(C2=CC=C(NC(C)=O)C3=CC=CC1=C32)=O
	JY-30 (50H04)	O=C1C=C(CC(C)(C)C1)NC2=C(C=CC=C3)C3=CC=C2
	JY-42 (28A15)	OC(CN(C)CCO)CN1C2=CC=C(Cl)C=C2C3=C1C=CC(Cl)=C3
	JY-43 (31N07)	S=C(S1)N(NC(NC(C=C2)=CC=C2Cl)=O)C(C1(C)C)N(O)C(NC(C=C3)=CC=C3Cl)=O
	JY-44 (48B09)	[O-][N+](C(C=C1)=CC=C1N/N=C/C(C(C)=C2COC(C)=O)=C(C)C=C2C)=O
	JY-45 (51J17)	O=C(/C=C/C1=CC=CC=C1)NC2=NN=CN2
	JY-46 (51G05)	O=C(C1=C2C=CC=C1)C(C(OCC)=O)=C(C3=CC=C(CC)C=C3)C2=O
	JY-63 (46E7)	[O-][N+](C1=C(O)C(/C=N\NC2=NC(NC3=CC=C(C=C3)[N+]([O-])=O)=NC(OC(C(F)(F)F)C(F)(F)F)=N2)=CC=C1)=O
	C-PAF (carbamyl-platelet-activating factor)	CCCCCCCCCCCCCCCCOCC(COP(=O)([O-])OCC[N+](C)(C)C)OC(=O)NC
	29-D16	S=C(N)N/N=C(C1=C2C=CC=C1)/C(C2=N3)=NC4=C3C=CC=C4
	SMIR4	O=C(C1=CC(C(N(C2=CC=C(C(NC3=CC=C(Br)C=C3)=O)C=C2)C4=O)=O)=C4C=C1)NC5=CC=C(Br)C=C5
	CSA (cyclosporin A)	CCC1C(=O)N(CC(=O)N(C(C(=O)NC(C(=O)N(C(C(=O)NC(C(=O)NC(C(=O)N(C(C(=O)N(C(C(=O)N1)C(C(C)CC=CC)O)C)C(C)C)C)CC(C)C)C)CC(C)C)C)C)C(C)C)C)C
	FK-506	CC1CC(C2C(CC(C(O2)(C(=O)C(=O)N3CCCCC3C(=O)OC(C(C(CC(=O)C(C=C(C1)C)CC=C)O)C)C(=CC4CCC(C(C4)OC)O)C)O)C)OC)OC
	ATRA (all trans-retinoic acid)	CC1=C(C(CCC1)(C)C)C=CC(=CC=CC(=CC(=O)O)C)C
	LPA	CCCCCCCCC=CCCCCCCCC(=O)OCC(COP(=O)(O)O)O.[Na]

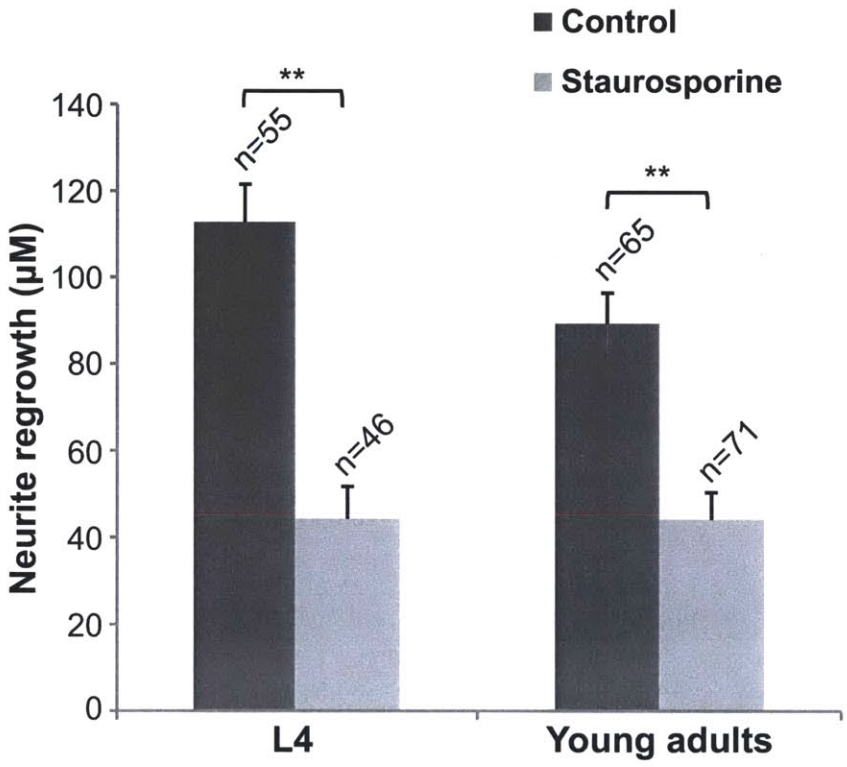

Figure 4-4: Effect of staurosporine on regeneration at different developmental stages of *C. elegans*. PLM neurons of L4 or young adult zdIs5 nematodes were axotomized 50 µm or 60 µm away from the cell body respectively, and regrowth was scored after 48 h (**, $P \leq 0.01$). Error bars indicate the s.e.m., n indicates the number of animals used in each case. Nematodes were incubated in the presence of either 0.47% DMSO (control) or 10 µM staurosporine in 0.47% DMSO, both of which caused significant toxicity and death in L3 or younger stage animals (hence, data is not provided for these stages).

Table 4.4: Effects of kinase modulators on the regeneration of C. elegans PLM neurons. Note that at higher concentrations staurosporine also inhibits Myosin light chain kinase (MLCK), PKA, PKG, and CaMKII, and that Mitogen-activated protein kinase (MAPK) and MLCK are also inhibited at higher concentrations of Wortmannin.

Small molecule	**Molecular target**	**Regeneration effect vs. control (%)**	***P*-value**
db-cAMP	cAMP-dependent protein kinase (PKA)	-0.388	0.973
H-89	PKA	-0.680	0.781
LY-294,002	Phosphatidylinositol 3-kinase (PI3K)	+1.271	0.894
PD 98,059	MAPKK	-30.549	0.765
Staurosporine	PKC	-60.796	1.623×10^{-7}
Wortmannin	PI3K	+7.258	0.606
Y-27632	ROCK	-12.790	0.367

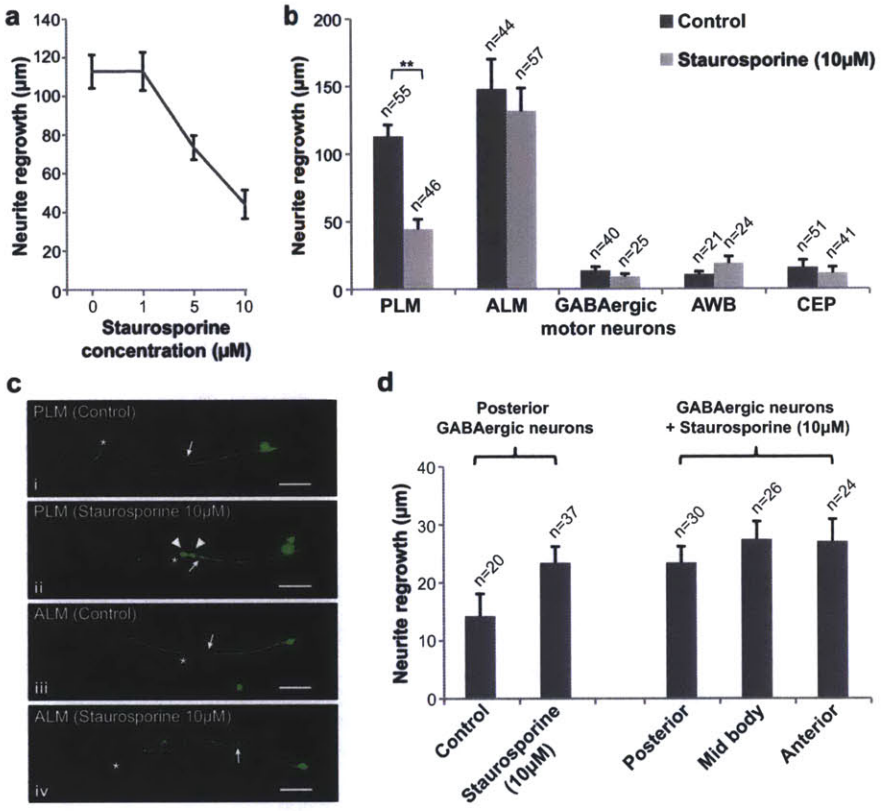

Figure 4-5: Effect of staurosporine on neurite regrowth is dependent on staurosporine concentration and neuronal type. (a) PLM neurons of L4 nematodes were axotomized, and regeneration was measured after 48 h. Staurosporine inhibited regrowth at concentrations of 5 µM or higher. Toxicity was observed at concentrations higher than 10 µM. (b) Laser microsurgeries were performed on different neuronal types of young adult nematodes, and regeneration was measured 48 h later. Staurosporine had a significant effect only in PLM neurons (**, $P \leq 0.01$). (c) Regeneration phenotypes observed 48 h after axotomy of PLM (i and ii) or ALM (iii and iv) neurons in staurosporine-treated and control animals. Arrows and asterisks indicate start and end points of regenerated axons respectively. Arrowheads in (ii) indicate terminal retraction bulb and axonal swellings formed in PLM neurons after staurosporine treatment. Scale bars: 30 µm. (d) Effect of staurosporine on GABAergic motor neurons at different parts of the nematode body. GABAergic neurons were axotomized in L4 animals and regeneration was measured after 48 h. Treatment of nematodes with 10 µM staurosporine did not significantly alter the regrowth of posterior GABAergic neurons when compared to non-treated animals. The regeneration response was similar among anterior, mid-body or posterior GABAergic neurons after exposure to staurosporine. Error bars in (a), (b) and (d) denote the s.e.m., and n indicates the total number of animals used.

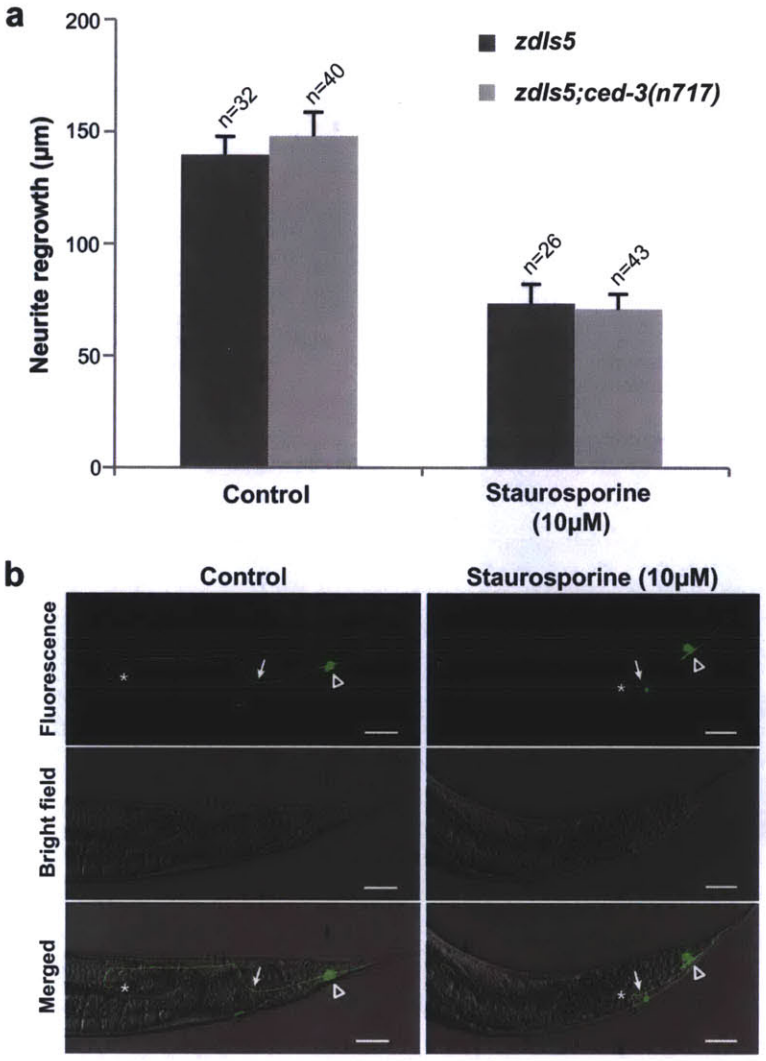

Figure 4-6: Suppression of neurite regeneration by staurosporine is not due to induction of apoptosis. (a) PLM neurons of L4 nematodes were axotomized, and animals were incubated for 48 h with or without stauroporine. The apoptosis-defective *ced-3(n717)* genetic background affects neither regeneration nor the effect of staurosporine on the regrowth of PLM neurites after laser surgery. Error bars denote the s.e.m., and n indicates the total number of animals used. (b) Axotomized L4 nematodes were incubated for 5 days in the presence of 10 µM staurosporine. We did not observe formation of apoptotic bodies in either non-treated or in staurosporine-treated animals, as shown in the Hoffman and fluorescence images. Persistent expression of GFP in both cases indicates that neurons survive and are functional. Arrows and asterisks indicate start and end points of regenerated axons respectively. The empty arrowhead points to the GFP-expressing cell body of the axotomized neuron in an animal that was exposed to staurosporine for 5 days. Scale bars: 30 µm.

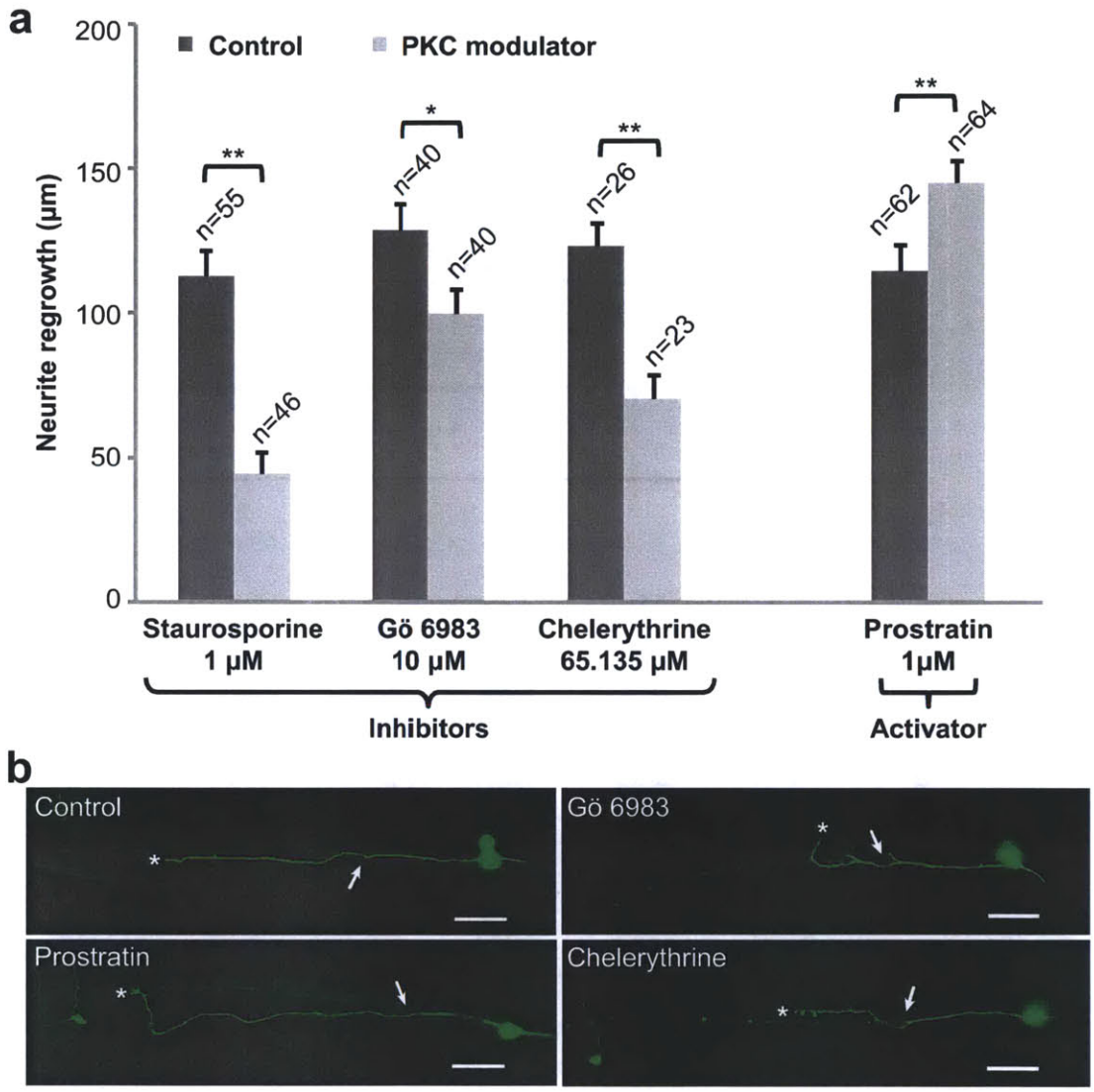

Figure 4-7: Enhancement and inhibition of regeneration by structurally different chemical modulators of PKC activity. (a) PLM neurons of L4 nematodes were axotomized, and animals were incubated for 48 h in the presence of staurosporine, Gö 6983, chelerythrine, or prostratin. The lengths of the longest regrowing neurites were compared (*, $P \leq 0.05$; **, $P \leq 0.01$). Error bars indicate the s.e.m., and n indicates the total number of animals used. (b) Representative images of regenerating PLM neurites as observed 48 h after laser microsurgery in non-treated (i), Gö 6983- (ii), chelerythrine- (iii), or prostratin-treated (iv) animals. Arrows and asterisks indicate start and end points of regenerated axons respectively. Scale bars: 30 µm.

a

Staurosporine targets	IC_{50} (nM)	Inhibitors used in the screen	Specific inhibitors
CaMK-II	20	-	KN-93
MLCK	1.3	Wortmannin	MLCK(342-352) amide
PKA	7	H-89	KT5720
PKG	8.7	-	sc-201161

b

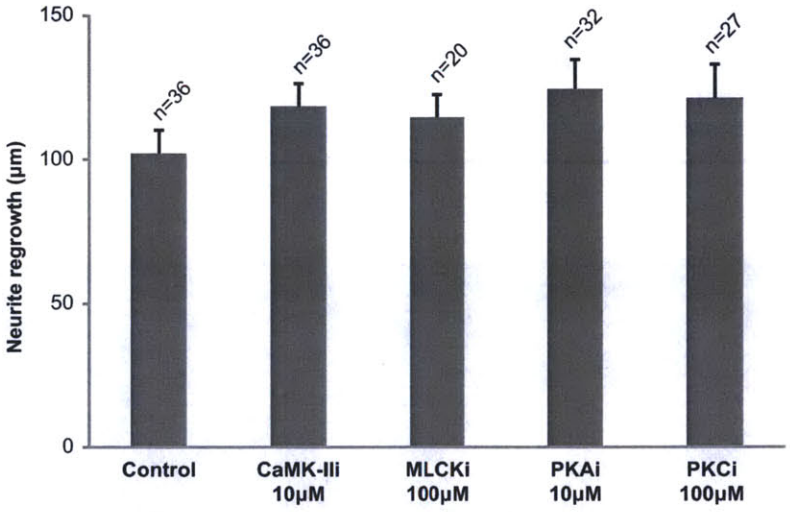

Figure 4-8: Effect of secondary staurosporine targets on regeneration. Specific inhibition of the secondary staurosporine targets Ca^{2+}/calmodulin-dependent protein kinase (CaMK-II), Myosin light-chain kinase (MLCK), Protein Kinase A (PKA) and Protein Kinase G (PKG) did not affect regrowth of the PLM axons following laser axotomy.

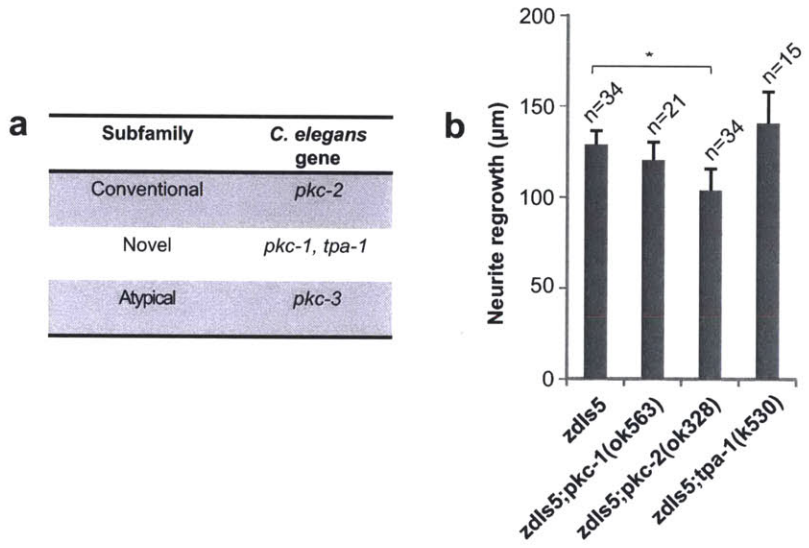

Figure 4-9: PKC subfamilies in *C. elegans* and the effects of their genetic inactivation on neural regeneration. (a) Identified *C. elegans* PKC genes. (b) Effects of genetic inhibition on the regrowth of PLM axons following laser microsurgery.

Chapter 5

Screening via temperature modulation[†]

Abstract

High-resolution *in vivo* time-lapse assays require repeated immobilization and imaging of whole animals. Here we report a technology for screening *Caenorhabditis elegans* at cellular resolution over its entire lifespan inside standard multiwell plates using repeated immobilization, imaging and optical manipulation. Our system does not use any fluidic or mechanical components, and can operate for tens of thousands of cycles without failure. It is also compatible with industrial high-throughput screening platforms and robotics, and it allows both chemical, and forward- and reverse-genetic screens. We used this technology to perform subcellular-resolution femtosecond laser microsurgery of single neurons *in vivo*, and to image the subsequent regeneration dynamics at subcellular resolution. Our single-neuron *in vivo* time-lapse analysis shows that neurite regrowth occurring over short time windows is significantly greater than that predicted by ensemble averaging over many animals.

Key words: Caenorhabditis elegans, femtosecond laser microsurgery, immobilization, time-lapse imaging, screening, multiwell plates.

[†]**This chapter is an adaptation of the material found in [129]. Author contributions: C.B.R. and M.F.Y. designed experiments and wrote the manuscript; C.B.R. performed the experiments.**

5.1 Motivation

Despite the capabilities of the microfluidic devices we and others have designed, these types of systems are complex to manufacture, operate, and maintain. Integration of these techniques into existing HTS platforms using multiwell plates for large-scale incubation of *C. elegans* has not been demonstrated, and is challenging due to well-known "world-to-chip" fluidic interface issues [130]. Microfluidic devices for long-term isolation of *C. elegans*, similar to the incubation chambers previously shown, have been demonstrated [131], yet the scalability of these devices for large-scale assays has not yet been shown, due to the significant overhead required for incubation of large numbers of animals. Although *C. elegans* can be anesthetized in multiwell plates for immobilization and imaging, the effects of anesthesia are slow and variable, and removal of the anesthetic media without losing animals is challenging. Additionally, exposure to anesthetics has side effects [80]. Here, we demonstrate a simple method to rapidly and noninvasively immobilize *C. elegans* in standard multiwell plates at multiple time points by modulating the temperature of individual wells. This method is compatible with existing instruments, robotics, and protocols used in high-throughput screening. Furthermore, this system does not use any fluidic or mechanical components, and can operate for tens of thousands of cycles without failure. It can perform both chemical, and forward and reverse genetic screens at cellular resolution in vivo. In total, only a few minutes are needed to immobilize the animals when screening an entire plate, and animals are immobilized only during for the brief period in which they are imaged, thus minimizing stress. Using this technology, we study the regeneration dynamics of single neurons in individual animals over time using laser microsurgery in multiwell plates. Our single-neuron *in vivo* time-lapse analysis shows that neurite regrowth occurring over short time windows is greater than that predicted by ensemble averaging over many animals.

5.2 Materials and methods

5.2.1 Device construction and operation

Individual cooling elements consist of a 6.6×6.6-mm TEC (NL1011T-01AC, Marlow Industries) and aluminium and coppers pins cut from 1/4" square rod. The aluminium pin is

attached to the cooled surface of the TEC and the copper pin is attached to the opposite side of the TEC using a thermal adhesive (Arctic Alumina, Arctic Silver). A 1/4" thick copper backplane with 1/4" square holes cut into it is used to array the cooling elements and provide additional heat dissipation. The individual TECs are powered by a DC power supply set to 1.1 V (CS13005X III, Circuit Specialists), which draws a current of ~0.6 A per active TEC. The entire device is placed in a 96-well plate with thin glass bottom (MGB096-1-2-LG-L, Matrical) so that wells can be imaged by a standard inverted epi-fluorescence microscope (Eclipse Ti-U, Nikon). Anti-fog drops (FogTech) are used to prevent condensation on the underside of the glass during cooling.

5.2.2 Well temperature measurements

Fine wire thermocouples (5TC-TT-T-40-36, Omega) were immersed into multiwell plates at various positions. Wells were filled with 150 µl of liquid nematode growth medium (NGM) and cooled using the described cooling technology. Thermocouple measurements were recorded using a temperature logger (HH147U, Omega).

5.2.3 Nematode handling

Nematodes were grown at 15 °C in NGM agar plates, unless otherwise stated. Standard procedures were followed for *C. elegans* maintenance [99]. Nematode strains used in this study included SD1726: Is[phis-72GFP;punc-54H1::mCherry;ppha-4mCherry], SK4005: zdIs5[pmec-4GFP]I and CX3553: lin-15B(n765)ky Is104[pstr-1GFP]X. The first strain was a gift from the laboratory of Stuart Kim and the latter strains were obtained from the Caenorhaditis Genetics Center. Age synchronizations were performed by transferring ~25 gravid adults to a fresh NGM agar plate and allowing them to lay eggs for 6 h at 20 °C. Following egg laying, the adults were removed and the plates were maintained at 15 °C for the animals to grow normally. Animals were loaded into the individual wells using a pick.

5.2.4 Lifespan analysis

Two populations of animals were incubated in 96-well plates, with six animals and 150 µl of liquid NGM supplemented with OP50 per well. The first population was cooled for 5 min every hour over a 24-h period and was maintained at room temperature for the remaining time. The control population was not cooled and was maintained at room temperature.

Subsequently, both populations were transferred to agar plates with OP50 feeding bacteria in order to recover. Animals were observed once per day to assess mortality, and transferred to new plates when needed.

5.2.5 Measurement of immobilization and image acquisition times

Animals were incubated in 96-well plates with one animal per well in 100 µl of liquid NGM supplemented with OP50. The time required to immobilize and capture an image of an animal were recorded. The time reported for positioning/focusing includes the time required to move the position stage from well to well, locate an animal using a $\times 2/0.1$ NA objective lens, switch to a $\times 20/0.75$ NA objective lens and focus on the animal. The majority of this time was spent automatically centring the animal within the field of view and subsequent focusing. The time reported for imaging includes the time required to capture the image with 750-ms exposure, save it to the disk and switch back to the $\times 2$ objective lens. For the first well of the plate, an additional time is required for the cooling to halt the movement of the animals because the first well does not benefit from the pipelined cooling (see Section 5.3.1). A Photometrics CoolSNAP HQ2 camera was used to acquire images. The field of view of this camera was 4.66×3.355 mm, using the $\times 2$ objective lens.

5.2.6 Laser surgery

The optical path was set up as described in Appendix A. To perform femtosecond laser microsurgery, a Mai-Tai HP (Spectra-Physics) femtosecond laser beam with 800-nm wavelength and 80-MHz repetition rate was delivered to the specimen by means of an inverted microscope (Eclipse Ti-U, Nikon). ALM and AWB axons were axotomized by pulses with 7 nJ energy for 1.5 ms, using a $\times 20/0.75$ NA objective lens. For laser surgery on glass slides, synchronized nematodes were immobilized on 2% agarose pads using a drop of 10 mM NaN_3. Measurements of axon regeneration were recorded and analyzed using a MATLAB program.

5.2.7 Effects of immobilization methods on regeneration

We performed surgery both on animals anaesthetized on agar pads, and on animals immobilized using in-well cooling. We cut one ALM axon per animal, 50 µm from the soma, using the laser parameters described above. Following surgery, we split the animals that

were axotomized under anaesthesia into two populations, both maintained at 20 °C. One population recovered on agar plates whereas the other population recovered in a 96-well plate with six animals per well in 150 µl of liquid NGM supplemented with OP50. The animals that were axotomized using in-well cooling were maintained in a 96-well plate with six animals per well in 150 µl of liquid NGM supplemented with OP50. Regeneration length was measured either 24 or 48 h following injury.

5.2.8 Effects of repeated immobilization on regeneration

Surgeries were performed on young-adult animals 50 µm from the ALM soma or 30 µm from the AWB soma. Animals were immobilized by cooling in 96-well plates with six animals per well in 100 µl of liquid NGM supplemented with OP50. Following surgery, both populations recovered at 20 °C in well plates, and one population was also cooled for 5 min per well every 6 h using the device. Regeneration length was measured 48 h post surgery.

5.2.9 Multitime-point imaging and analysis

Surgeries were performed on young adult animals 50 µm from the ALM soma. Animals were incubated in 96-well plates with 100 µl of liquid NGM supplemented with OP50 per well at 20 °C. The animals were immobilized by in-well cooling and imaged at multiple time points (4, 8, 12, 18, 24, 30, 36, 42 and 48 h post surgery). Regeneration length at 6 h was calculated by averaging data at 4 h and 8 h. Growth rates from 6-42 h were calculated from the regrowth length using a centre difference method and the 48-h growth rate was calculated using a backwards difference method. The centroids of the time windows were calculated as

$$T = \frac{\sum v_i t_i}{\sum v_i}$$

where v_i is growth rate data from the time points t_i that make up the time window.

5.2.10 Statistical analysis

Comparisons of regeneration lengths were performed using a two-tailed Student's t-test. Lifespan analysis was performed with the Logrank (Mantel-Cox) test using the GraphPad Prism software package.

5.3 Fabrication, operation, and results

5.3.1 In-well cooling apparatus and its operation

It is well known that cooling reduces the motion of *C. elegans* [81]. Our device consists of an array of individually addressable cooling elements that rapidly decrease the temperature of wells. Each individual cooling element consists of a small square thermoelectric cooler (TEC) bonded to an aluminum pin (which is inserted into the well) and a copper pin (which is used to dissipate heat; Figure 5-1a). The copper pins of the individual cooling elements are slotted into a copper backplane that is passively cooled, and the individual pins are inserted into the wells (Figure 5-1b). This design is easily scalable to different well numbers and dimensions. Independent control of well temperatures allows much faster screening of wells by pipelining: While animals in one well are being imaged using inverted epi-fluorescence microscopy, the neighboring wells that have yet to be imaged can be gradually cooled to immobilize the animals in preparation for subsequent imaging and optical manipulation (Figure 5-1c). Once the animals within the first well are imaged, the cooling element is immediately turned off, allowing the animals to return to room temperature while the already-cooled animals in the next well are imaged. This prevents the animals from being exposed to low temperatures over the entire duration for which the multiwell plate is imaged. During the cooling period, the temperature of the wells reaches 3-4 °C, with little cooling of the adjacent wells (Figure 5-2) and negligible cooling of the wells beyond these. At the centre of the adjacent wells, the temperature stays above 16 °C (even after prolonged cooling), which is within the normal temperature range used for *C. elegans* culture. A temperature of 3-4 °C was found to be the threshold temperature required to immobilize *C. elegans*; higher temperatures did not sufficiently slow the animals' movement. On average, <20 s (thus ~32 min per plate) is required for all steps needed to image animals in the subsequent wells, including the time required to locate the animal, move the multiwell plate to centre the animal within the field of view, change objectives for high-resolution imaging, store images and switch back to a low-magnification objective (Figure 5-3). Following screening, the pins can be sterilized via heating by running the TEC in reverse (Figure 5-4).

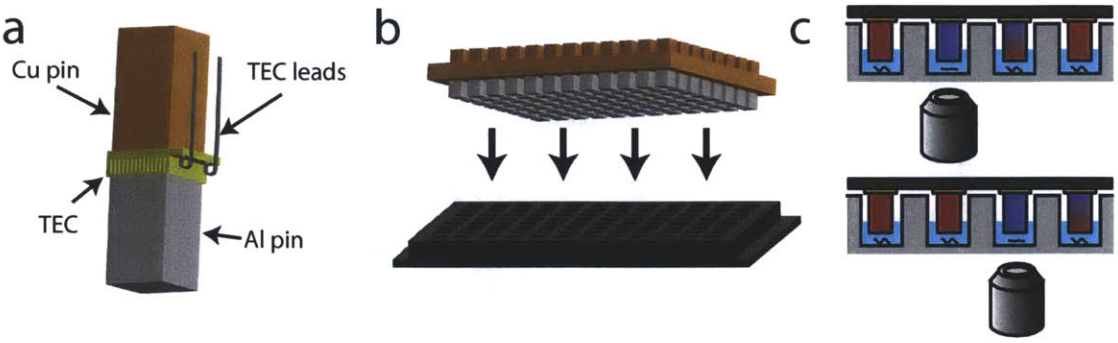

Figure 5-1: Immobilization of *C. elegans* in standard multiwell plates. (a) In-well cooling device and its operation. (a) Individual cooling elements consist of an aluminum pin bonded to a thermoelectric cooler (TEC) with a copper pin bonded to the opposite side to dissipate heat. (b) Cooling elements can be arrayed to match various well configurations. (v) Pipelined cooling. Thermoelectrically-cooled pins are inserted into wells containing animals. Once activated, a cooling element reduces the temperature of the well, immobilizing the animal(s) within that well. Immobilized animals are imaged or optically manipulated using inverted epi-fluoresence microscopy. Concurrently, neighboring wells are cooled such that the animals to be subsequently imaged are immobilized in advance.

5.3.2 Stable immobilization and imaging in multiwell plates

During the low-temperature period, cellular-resolution fluorescence images of entire animals can be acquired (Figure 5-5a). Figure 5-5b shows an animal before and after cooling and highlights the drastic improvement in image resolution. In addition to L4-stage and adult animals, this system can successfully immobilize early-larval stage animals (Figure 5-6). The reliability and reusability of this technology is very high because it does not use any moving parts or microfluidic components. Cycling a cooling element continuously for 25,000 cycles (1 min on, 30 s off) had no impact on the cooling performance (Figure 5-7). This is equal to the number of cycles the system would perform if plates were imaged continuously at a rate of one plate per hour for 2.7 years.

5.3.3 In-well cooling does not affect animal health

We recorded several measurements to assess how our technique influences animal physiology under frequent immobilization conditions. The difference between the lifespan of the repeatedly cooled animals (cooled for 5 min every hour for 24 h) and the lifespan of the control group (Figure 5-8) was nonsignificant (Logrank test; $P = 0.61$). Similarly, repeated cooling did not affect the morphology of the animals nor their progeny count.

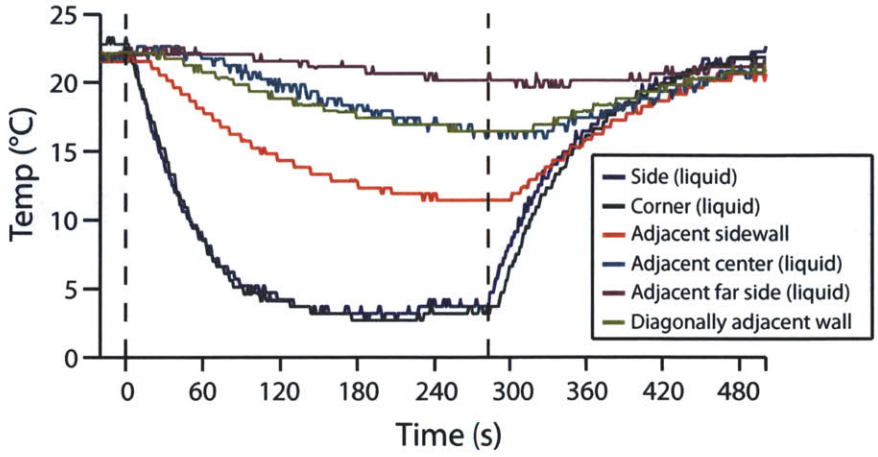

Figure 5-2: Temporal and spatial dependency of the temperature inside the well being cooled (near the sides and corners), in an orthogonally adjacent well (near the wall adjacent to the well being cooled, near the adjacent-well centre and near the side of adjacent well that is furthest from the well being cooled) and in a diagonally adjacent well (near the corner closest to the well being cooled). Thermoelectric cooling was started at t=0 s (first dashed line) and stopped at t=280 s (second dashed line). See Methods for measurement technique.

Frequent cooling for time-lapse imaging also did not affect neurite regeneration, which is a highly dynamic process: Our technique enables the use of subcellular-resolution optical manipulation methods in multiwell plates, such as femtosecond laser microsurgery in multiwell plates. Precise targeting of axons by a laser for microsurgery becomes possible when the animals are immobilized by cooling (Figure 5-9a). Following surgery, axons regenerate (Figure 5-9b) as we previously showed in the first observation of axonal regeneration in *C. elegans* [72, 73]. We first determined whether cooling affects regeneration by examining three different surgery conditions in young-adult animals. We performed surgery both on anesthetized animals on glass slides, and on animals immobilized using in-well cooling. After surgery, the animals axotomized under anesthesia were split into two populations, one population recovered on agar plates, and the other population recovered in a 96-well plate with liquid culture in the wells. Regeneration was observed 24 and 48 h following injury, and no significant difference was found between the regeneration observed in animals immobilized by in-well cooling and those immobilized by anesthesia (Figure 5-10a). We also examined whether frequent immobilizations following femtosecond laser microsurgery affect regeneration: There was no significant difference (Student's t-test $P = 0.52$) in the regeneration observed 48 h post-surgery between a population that was cooled for 5 min

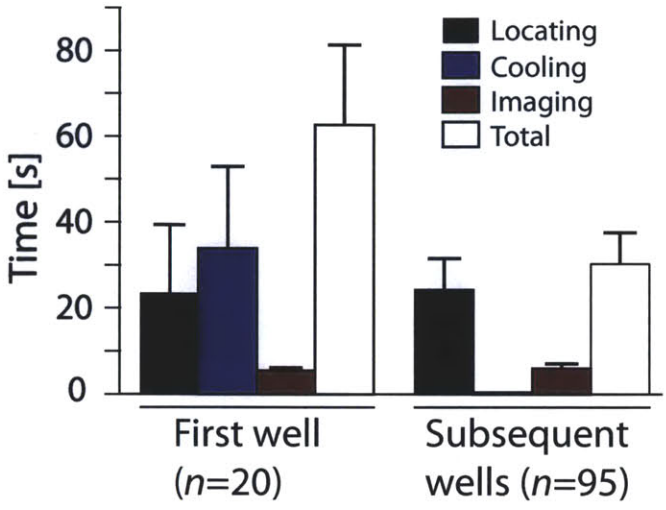

Figure 5-3: Effects of pipelining on time required for *C. elegans* immobilization and imaging inside a well plate with single animal per well, including time required to change objectives, move the stage, and store the image data. Error bars show STD.

every 6 h and a control population that was not cooled but was maintained under otherwise identical conditions (Figure 5-10b). Repeated cooling similarly did not affect the regeneration of the olfactory amphid wing 'B' (AWB) neurons in the head (Student's t-test; $P = 0.33$; Figure 5-10b).

5.3.4 Multi-time-point analysis of neural regeneration

Following surgery, we examined the axonal regeneration dynamics by frequently immobilizing and imaging several animals (Figure 5-11 and Figure 5-12a) over a 48-h time window. Analysis of single neurons showed that the majority of regeneration (75±5.5%) occurs within a short 18-h window (Figure 5-12b). In the absence of repeated single animal immobilization and imaging, only statistical averages can be obtained from end-point measurements on many animals. Such averaging (red dashed line in Figure 5-12a and b) underemphasizes the growth that occurs after the first 24 hours post axotomy, obscuring that the period of largest growth in some instances can occur later (Figure 5-12c). Use of the average regeneration rate also incorrectly predicts a significantly smaller amount of regrowth during any 18-h window (58 versus 75%, Student's t-test; $P = 0.008$).

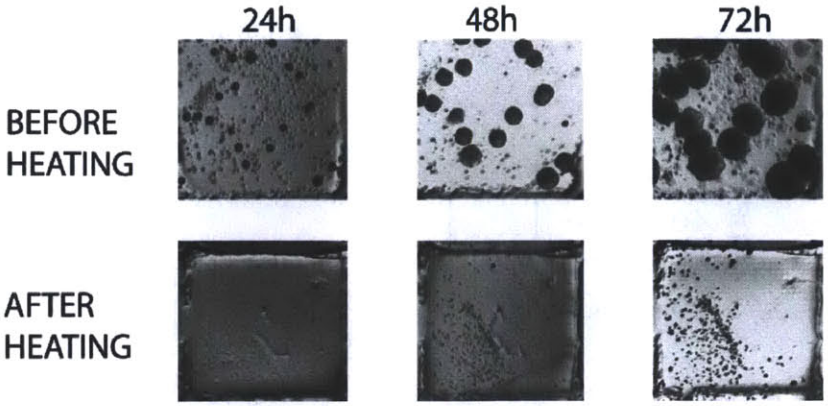

Figure 5-4: Pin sterilization via thermoelectric heating. Following insertion of the cooling into a well containing 150 µL of liquid NGM medium supplemented with OP50, the end of the pin was pressed into an agar plate. The TEC was then run as a heater by biasing it at 2.5 V opposite to its normal (cooling) configuration. At this voltage, the temperature at the end of the pin was approximately 120 °C. After being heated for 10 min, the TEC was deactivated and after waiting 1 min the pin was pressed into another agar plate. Both plates were incubated for 3 days at 37 °C and observed every 24 h.

5.4 Discussion

Performing screens entirely within multiwell plates confers several significant benefits. Because multiwell plates are commonly used, there already exists a wealth of equipment, robotics and protocols for screening in this format. As a result, our technology can expand the use of existing HTS systems to perform high-content multicellular organism screens at subcellular resolution. High-speed precise liquid handling equipment can be used to rapidly dispense precise volumes of screening compounds, and multiwell plates also simplify isolation of animals for multitime-point tracking of single animals throughout the experiments. Screening *C. elegans* entirely within multiwell plates also eliminates the complexity, cost and unreliability associated with microfluidics, as well as the "world-to-chip" fluidic interface issues for large-scale incubation of animals. Our cooling apparatus could could be manipulated with high-throughput robotics, and also does not require any fluidic components; thus, it is not susceptible to clogging or loss of animals. No side effects on animal lifespan, neurite regrowth, progeny count or animal morphology are observed even after frequent immobilization and imaging of animals at multiple time points. Each well of a 96-well plate has sufficient volume of media to ensure that *C. elegans* is healthy over its entire lifespan, and 96-well plates were previously used to enable large-scale screening of *C. elegans* from

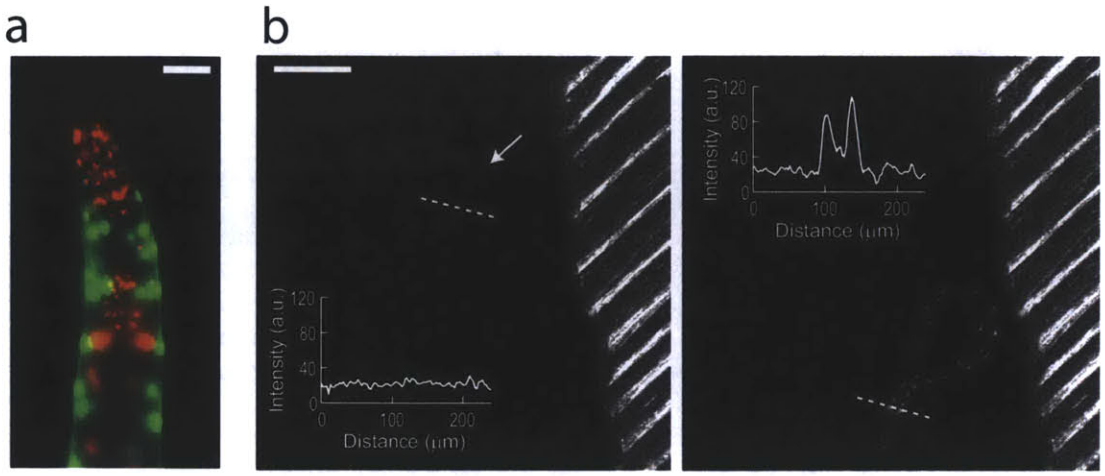

Figure 5-5: Subcellular resolution imaging of *C. elegans* immobilized in standard multiwell plates. (a) Multi-channel fluorescence image of an animal immobilized using in-well cooling. Green: his-72, red: unc-54 & pha-4. Scale bar: 30 μm. (b) Fluorescence image of an animal before and after cooling. (Left) Before cooling, the animal is moving too rapidly for visualization at 10 frames/sec. (Right) Following cooler activation, the animal's movement slows drastically allowing high-resolution imaging. Insets show fluorescence intensity across the section of the animal indicated by the dotted lines in each image. Cooling pin is visible on the right side of both images. Scale bar: 250 μm.

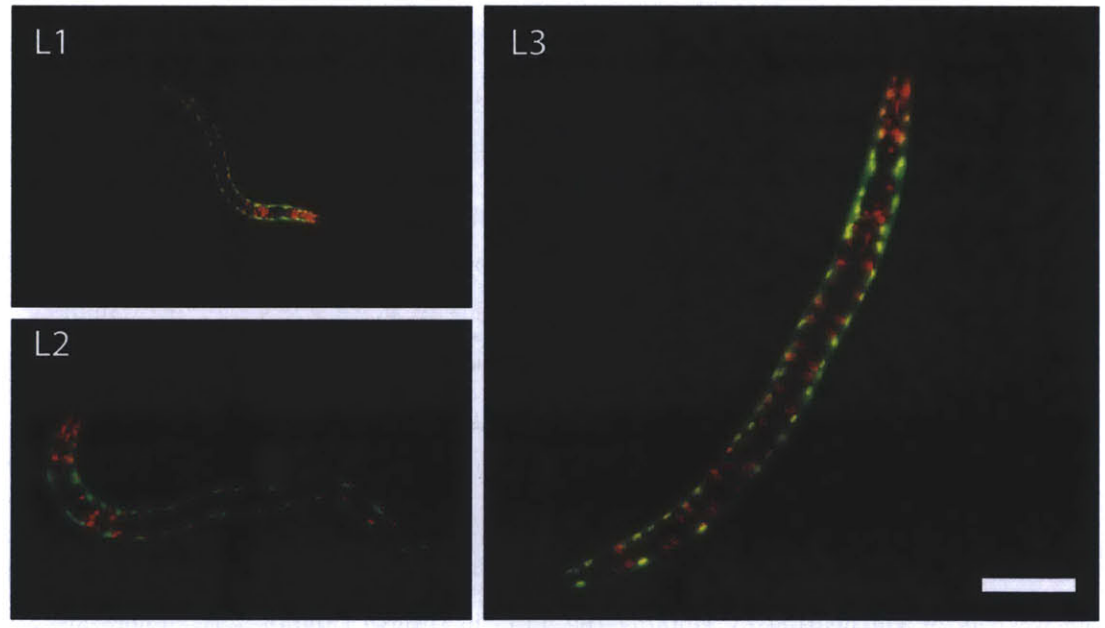

Figure 5-6: Immobilization of early-larval stage *C. elegans*. L1-L3 animals are immobilized with sufficient stability to image cellular features. Green: his-72, red: unc-54 & pha-4. Scale bar: 40 μm.

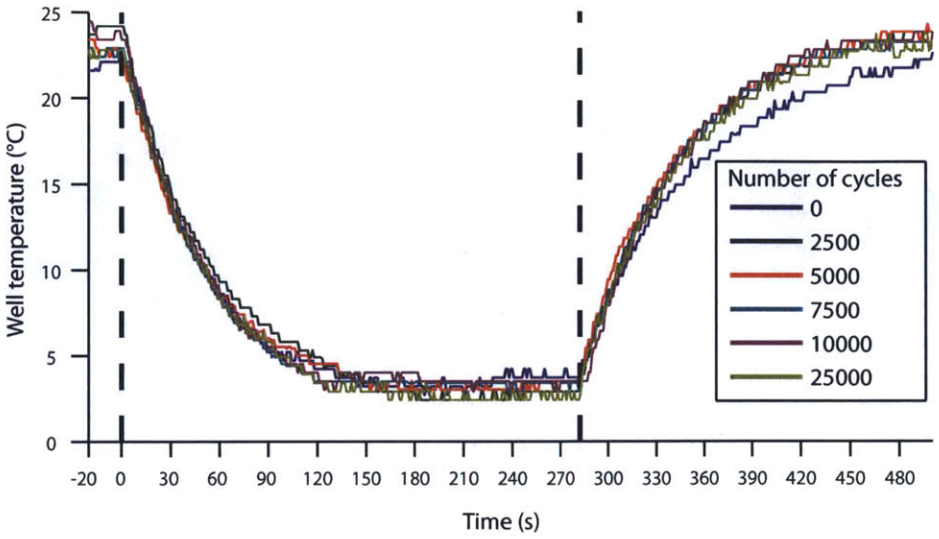

Figure 5-7: Device lifespan. A single cooling element was repeatedly cycled for 60 s on, 30 s off a total of 25000 times (i.e. 625 h or ~26 d). After the indicated number of cycles a well with 100 µl of water was cooled for 280 seconds and the temperature during cooling was recorded.

L1 stage until death to identify chemicals that extend lifespan [132]. As *C. elegans* can produce significant numbers of progeny inside the wells, fluorodeoxyuridine is commonly used to induce sterility while still allowing animals to develop normally [132–134]. Absence of progeny simplifies tracking of animals throughout their entire lifespan, and reduces both the amount of feeding bacteria required and the buildup of waste inside the wells.

Subcellular-resolution forward- and reverse-genetic assays, as well as chemical assays, are possible in high-throughput-compatible multiwell plate formats using our technology. Animals can be dispensed into multiwell plates either by flow sorters [24], or by manual or automated liquid dispensers. Our device subsequently allows immobilization of animals in the individual wells for imaging at multiple time points. Forward genetic screens can be performed if mutagenized animals are dispensed into the wells. Reverse-genetic screens or chemical screens can be performed if the animals are incubated in wells containing either chemicals or dsRNA-expressing bacteria. The pins can be sterilized either by commercial pin washers or via heating by running the TEC in reverse (Figure 5-4). There are also a number of powerful image processing algorithms that, combined with our technology, can further enhance the ability to perform high-throughput and high-content screens on *C. elegans*. Using a low-magnification objective, an entire well can be imaged and the

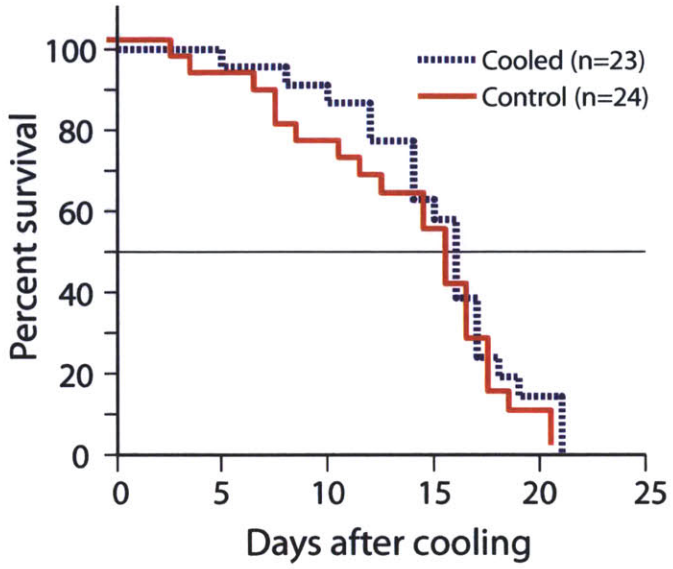

Figure 5-8: Effects on *C. elegans* lifespan after cooling for 5 min every hour. There was no significant difference between the lifespans of the cooled (blue dashed line) and control (red solid line) populations ($\bar{t}_{cooled} = 15.2$, $\bar{t}_{control} = 14.3$ days, Logrank test; $P = 0.61$).

location of individual animals can be determined automatically [59]. Higher resolution images of individual animals can be automatically straightened in 3D [58], which simplifies animal comparison and results in smaller file sizes. Automated cell-lineage tracing [66], three-dimensional nuclei segmentation [135], and cell-body ablation [100] have all been demonstrated for *C. elegans*. Our work enables the use of these advanced image processing techniques in a HTS-compatible format.

C. elegans is a useful model for studying neuronal regeneration as its stereotypic anatomy and hermaphroditic reproduction allow repeated studies of the same type of neural injuries in isogenic animal populations, significantly enhancing the reproducibility of assays. Previous studies combining laser microsurgery and *C. elegans* have identified how several factors, including animal age, neuronal type, synaptic branching and axon guidance signalling, influence regeneration [74–76]. Laser microsurgery screens, as well as screens using nematodes exhibiting spontaneous neurite breaks due to dysfunction of β-spectrin, have also revealed that axon regrowth depends on the activity of MAP kinase pathways [76–78]. In the previous chapter we demonstrated the use of microfluidics in combination with femtosecond laser microsurgery to perform chemical screens on neural regeneration in *C. elegans*. This screen identified a role for protein kinase C in the regeneration of the posterior lat-

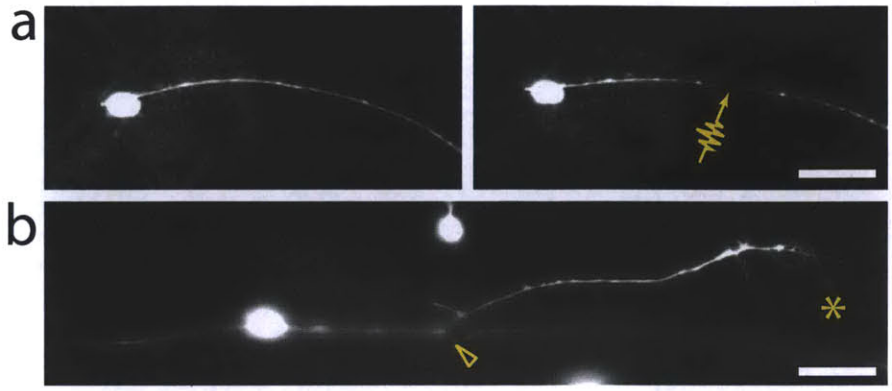

Figure 5-9: *In vivo* femtosecond laser microsurgery in multiwell plates. (a) Localized ablation and regeneration of anterior lateral mechanosensory (ALM) axon in mec-4::GFP animal. Arrow (⚡) indicates point of surgery. (b) Regeneration 48 h after surgery. Triangle (△) indicates starting point of regeneration, asterisk (*) indicates end of maximum-length branch 48 h post surgery. Scale bars: 20 µm.

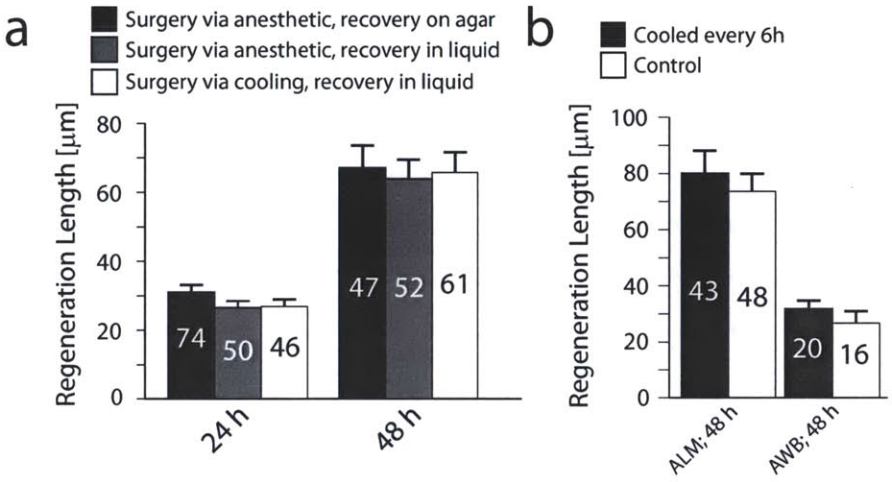

Figure 5-10: Effects of cooling on regeneration following *In vivo* femtosecond laser microsurgery in multiwell plates. (a) Effect of immobilization method and recovery conditions on regeneration following axotomy. Graph shows length of the longest regenerating branch from the cut point following axotomy of ALM neurons in young-adult animals. There is no significant difference between the cooled (black bar) population and the anesthetized control groups (gray bar for recovery in liquid, white bar for recovery on agar) either 24 h (Student's t-test; $P = 0.91$, 0.18 for the animals that recovered in liquid or on agar, respectively) or 48 h ($P = 0.88$, 0.82, respectively) post-surgery. The total number of animals in each experiment is indicated on the bar. (b) Effect of multiple immobilizations (every 6 h for 48 h) on regeneration of ALM and AWB neurons. There is no statistically significant difference between the regeneration measured in the cooled (black bars) and control (white bars) populations (Student's t-test; $P = 0.52$ and $P = 0.33$, respectively). The total number of animals in each experiment is indicated on the bar.

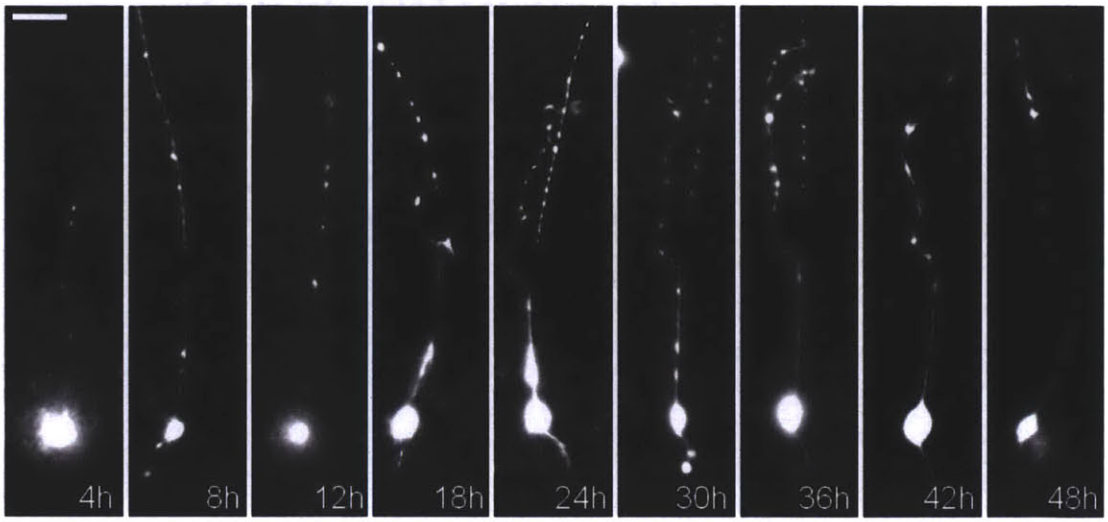

Figure 5-11: Time-lapse fluorescence imaging of neuronal regeneration in multiwell plates. Scale bar: 15 µm.

eral mechanosensory (PLM) neurons following surgery and showed that the small molecule prostratin enhances regeneration. Our new in-well cooling technology can drastically scale up these investigations on neural degeneration and regeneration by using a format entirely compatible with existing HTS systems. In addition, time-lapse analysis can yield significant insight into many physiological processes that cannot be gained through end-point assays, as we illustrated here for neuronal regeneration following injury. Similarly, using our system to image and screen time-resolved expression patterns of many genes using fluorescent reporters such as elt-3::GFP, ugt-9::GFP, and col-144::GFP [136] can facilitate the study of the aging process under variety of dietary, genetic, and environmental conditions.

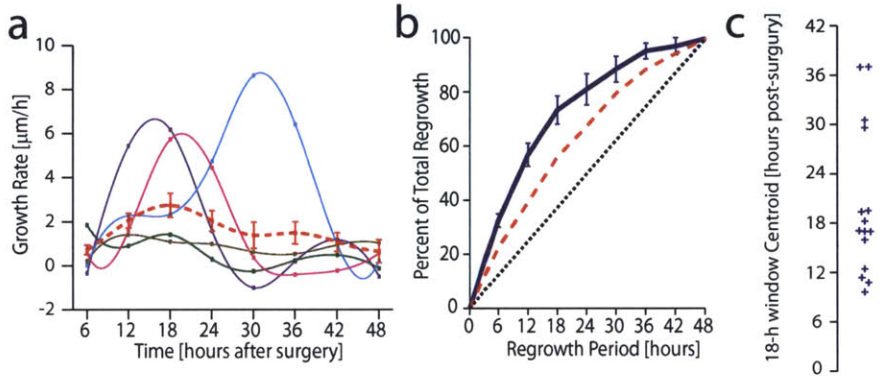

Figure 5-12: Analysis of neuronal regeneration dynamics. (a) Representative curves of calculated growth rate of regenerating branch versus time. Each solid colored line shows a measurement of the regrowth of a single neurite in an animal. Dashed red line shows mean growth rate averaged over n = 15 animals. (b) Percentage of total regeneration occurring over a moving time window. Solid blue line shows the percentage of 48-h regeneration versus the time window calculated from multitime-point measurements on individual animals (n = 15). Dashed red line shows the same calculation using the average growth rate measurements (red line in Figure 5-12a), and black dotted line shows the case if regeneration rate were constant. (c) Distribution of the center of the 18-h window in which most of the regeneration occurs. All error bars SEM.

Appendix A

Construction of the femtosecond laser microsurgery system†

Abstract

Femtosecond laser microsurgery is a powerful method for studying cellular function, neural circuits, neuronal injury and neuronal regeneration because of its capability to selectively ablate sub-micron targets *in vitro* and *in vivo* with minimal damage to the surrounding tissue. Here, we present a step-by-step protocol for constructing a femtosecond laser microsurgery setup for use with a widely available compound fluorescence microscope. The protocol begins with the assembly and alignment of beam-conditioning optics at the output of a femtosecond laser. Then a dichroic mount is assembled and installed to direct the laser beam into the objective lens of a standard inverted microscope. Finally, the laser is focused on the image plane of the microscope to allow simultaneous surgery and fluorescence imaging. We illustrate the use of this setup by presenting axotomy in *Caenorhabditis elegans* as an example. This protocol can be completed in 2 d.

Key words: femtosecond laser microsurgery, Caenorhabditis elegans

†**This chapter is an adaptation of the material found in [94]. Author contributions: C.L.G. and C.B.R. developed the laser axotomy techniques described in this protocol. M.A.S. and J.D.S. developed the beam expander structure. M.A., C.B.R. and C.L.G. developed the other elements of the system. M.A.S. developed the laser alignment technique. J.D.S., C.L.G. and C.P.-M. wrote the manuscript, and M.A. and M.F.Y. commented on the manuscript at all stages.**

A.1 Introduction

Here we detail a procedure to add a femtosecond laser microsurgery capability to a standard fluorescence microscope using commercially available components. The femtosecond laser microsurgery system (Figure A-1 and corresponding component descriptions in Table A.1) is designed to take up minimal space while allowing access to facilitate easy and reproducible alignment. The design provides flexibility in the choice of objectives, filter cubes, laser wavelengths and laser-pulse repetition rates while requiring no modification of the fluorescence microscope. The protocol begins with the installation of major components including the optical table, the microscope and the laser. Next, beam-conditioning optics (optical isolator, electro-optic modulator (EOM), Glan-Thompson polarizer and half-wave plate) are assembled and mounted. The construction and installation of a dichroic mounting adapter, an assembly that brings the laser beam in line with the optical axis of the objective, is then described. The protocol then details the installation of a periscope to raise the beam from the table to the microscope input port and a laser beam expander to resize the beam to fill the back aperture of the objective. The protocol concludes with step-by-step instructions for axotomy in *C. elegans*, which is included as an example application of the system. Adapting the system for other microsurgical applications, such as those mentioned above, involves modifications only to the standard sample preparation steps [137–142] and use of different objective lenses [88]. For example, although an air objective lens with a numerical aperture (NA) of 0.75 is sufficient for axonal ablation in *C. elegans*, for axotomy in zebrafish larvae, researchers have used water-immersion objective lenses with 0.8 or higher NAs [143]. For ablation of cytoskeletal filaments of cells *in vivo*, oil-immersion objective lenses with higher NAs of 1.4 are used [142]. In addition, different laser-pulse repetition rates have been used in the literature [74, 88, 142], where the lower pulse repetition rates yield reduced heat accumulation in specimen [88], and therefore less collateral damage. The high speed EOM and the high pulse-repetition rate laser used in this protocol provide the ability to choose any pulse repetition rate ranging from sub-KHz to 80 MHz, thus providing sufficient flexibility.

The system described here does not include a two-photon imaging capability. However,

Table A.1: Component list for the optical system layout of Figure A-1.

Component	Description
A	Femtosecond laser
B	Optical isolator
C	Half-wave plate
D	Glan-Thompson polarizer
E	Electro-optic modulator (optional)
F	Safety shutter and beam block
G	Kinematically mounted mirror
H	Ø1" Iris
I	Periscope
J	Ø1" Lens L1 on z-adjustable stage
K	Two Ø1" irises
L	Ø2" Lens L2
M	Beam expander
N	Dichroic mounting adapter
O	20× 0.75 Numerical aperture (NA) objective
P	Epifluorescence filter turret
Q	Lower half of microscope body
R	Camera

this capability can be easily added by replacing the top periscope mirror with scanning mirrors and by adding a photomultiplier tube to one of the camera ports of the microscope [144]. To adapt the laser system for simultaneous use by multiple microscopes simply requires the addition of a beam splitter, EOM, periscope, beam expander and dichroic mounting adapter for each additional microscope. If necessary, a regenerative amplifier or a higher-power laser can be used to ensure that sufficient power is delivered to each setup.

A.2 Materials

A.2.1 Reagents

- Experimental animals[1]. Although transgenic strains of cells/animals expressing fluorescent reporter proteins are not required for successful surgery, they do ease in the identification and targeting procedures. (*C. elegans*: the SK4005 strain can be used for visualization and axotomy of GFP-expressing mechanosensory neurons.)

[1] **Caution:** All animal experiments must comply with the relevant institutional and national animal care guidelines.

- Cover glass (0.175 mm × 25 mm × 50 mm)
- Microscope cover slides (1 mm × 25 mm × 50 mm)
- Agarose gel 1.5%
- Sodium azide 10 mM

A.2.2 Equipment

General equipment

- Femtosecond laser (Spectra Physics Mai Tai HP Ti:Sapphire, tunable-wavelength Class IV laser). More cost-effective femtosecond lasers with a fixed wavelength can also be used including: Polarynox femtosecond fiber lasers, Del Mar Photonics Ti:Sapphire custom made kit, model TISSA100 and HighQLaser FemtoTrain, model IC-1045-3000. Minimum recommended pulse energy is ~20 nJ (i.e., average power 1.6 W for a laser with 80 MHz pulse repetition rate)
- Laser warning sign and safety equipment which meet requirements set by institutional as well as local and national safety standards. Laser goggles with minimal safety rating of OD7+ are recommended (Diode/Nd:YAG 42F goggle, Kentek, cat. no. KGG-42F)
- Optical table with sufficient surface area (1) (3.0 m × 1.5 m) and set of four air-damped legs (Newport, cat. nos. RS-4000-510-12 and I-2000-413.5, respectively)
- Inverted fluorescence microscope system (1) (Nikon Eclipse TI or similar model, Nikon) including a 70-mm stage-up kit to provide sufficient clearance for the rear-entry of the laser beam and a stage plate capable of holding a standard glass slide
- Image acquisition software (1) (NIS-Elements 2.0) and compatible computer.
- High-resolution CCD camera (1) (Photometrics Coolsnap HQ2)
- RMS-threaded IR and VIS alignment disk (400-640 nm and 800-1700 nm) (1) (Thorlabs, cat. no. RMSIR)
- RMS 45 to CFI 60 objective adapter (1) (Nikon, cat. no. MXA20750)
- IR card (1) (Newport, model no. F-IRC4)

- Infrared viewer (1) (Newport, cat. no. IRV1-2000)
- Optical power meter and detector (1) (Newport, part nos. 1918-C and 818P-010-12, respectively)
- Ø1/2" Post (2") (1) (Thorlabs, cat. no. TR2)
- Ø1/2" Post holder (2") (1) (Thorlabs, cat. no. PH2-ST)
- Standard base (1) (Thorlabs, cat. no. BA2)
- Function generator with single-pulse generation capability[2] (1) (BK Precision, model no. 4030)
- Oscilloscope (Tektronix, TDS2024)
- 3/8" corded drill driver (1) (RIDGID, model# R70002)
- Drill set (Ryobi, model# AR2074)
- 1/4"-20 cap and set screws and #8-32 cap and screws (ThorLabs, cat. nos. HW-KIT2 and HW-KIT3, respectively)

Laser setup

- Optical isolator (1) (Conoptics, cat. no. 712TGG)
- Half-wave plate for 600-1050 nm high power applications (1) (Thorlabs, cat. no. AHWP05M-950)
- High-precision rotation mount for Ø1" Optics (1) (Thorlabs, cat. no. PRM1)
- Glan-Thompson polarizer with 600-1050 nm anti-reflection coating (1) (Thorlabs, cat. no. GL10-B)
- Polarizing prism mount (1) (Thorlabs, cat. no. SM1PM10)
- Kinematic mount for thin Ø1" Optics (1) (Thorlabs, cat. no. KM100T)

[2] **Critical:** If another model or device is used, ensure that the function generator, or any source in general driving the high-voltage (HV) amplifier, is capable of driving the input load of the high voltage amplifier. For example, if the input impedance of the HV amplifier is 50 Ω and the maximum input voltage is 1 V, the function generator must be able to supply at least 20 mA to have access to the full input range.

- EOM (1) and requisite HV amplifier (Conoptics, cat. no. 350-160 EOM with amplifier)[3]
- Optical isolator mount (1) (Conoptics, model M102, modified to hold the isolator)
- EOM mount-labjack (1) (Conoptics, model M102) (optional, see Steps 10-12)
- Safety shutter (1) (Electro-Optical Products SH-10 Interlock safety shutter with silver coated mirror, for NIR and DSH-10-110 V controller)
- Beam block (includes TR3 post) (7) (Thorlabs, cat. no. LB1)
- 2" High universal post holder (for use with beam blocks) (7) (Thorlabs, cat. no. UPH2)
- Ø1/2" post (2") (3) (Thorlabs, cat. no. TR2)
- Ø1/2" post holder (2") (3) (Thorlabs, cat. no. PH2-ST)
- Standard base (3) (Thorlabs, cat. no. BA2)
- 50-Ω BNC cables of sufficient length (2) to connect the function generator to the oscilloscope and to the HV amplifier (or high-speed shutter controller if that option is used). T-joint BNC-cable connector (http://Cablesnmore.com, cat. nos. N23713 and X15305, respectively)

Dichroic mounting adapter

- IR dichroic mirror (1) (Chroma, cat. no. 670dcspxr)
- Nikon adapter plate ('dust cover') (70 mm stage-up kit, Nikon)
- Ø1" (1") pedestal pillar post (1) (Thorlabs, cat. no RS1P)
- Compact kinematic mount (1) (Thorlabs, cat. no KMS)
- BA1 Standard base (1) (Thorlabs, cat. no. BA1)

[3]**Caution:** The cables connecting EOM to the HV amplifier carry high voltage. Only the appropriately rated cables from the EOM manufacturer should be used. (Optional, see Steps 10-12) A high-speed mechanical shutter capable of providing a 2.2 ms pulse can be substituted for the EOM; however, the EOM enables the added benefit of two-photon excitation targeting (see Step 93).

- Dichroic cube holder (1) (large aluminum filter cube, Nikon)
- High-performance epoxy (1) (Loctite Fixmaster, Loctite, part no. L08FA12920)
- #8-32 screw × 1/4" with low-profile head (1) (McMaster-Carr, cat. no. 91770A190)

Periscope and beam expander

- 40 mm focal length, Ø1", NIR achromatic doublet lens (1) (Thorlabs, cat. no. AC254-040) (dependent on back aperture of objective lens; see Step 43)
- 200 mm focal length, Ø2", NIR achromatic doublet lens (1) (Thorlabs, cat. no. AC508-200) (dependent on back aperture of objective lens; see Step 43)
- Single-axis position stage with micrometer (1) (Newport, cat. no. 460P-X)
- Ø1.5" post clamp adapter plate (1) (Thorlabs, cat. no. C1520)
- 14" tall Ø1.5" mounting post (3) (Thorlabs, cat. no. P14)
- Ø1.5" post mounting clamp (4) (Thorlabs, cat. no. C1501)
- Right-angle kinematic cage mount (2) (Thorlabs, cat. no. KCB1)
- Ø1" gold mirror (3) (Thorlabs, cat. no. PF10-03-M01)
- 12" optical rail (1) (Thorlabs, cat. no. RLA1200)
- Ø2" lens mount (1) (Thorlabs, cat. no. LMR2)
- Ø1" optics, translating lens mount (1) (Thorlabs, cat. no. LM1XY)
- Ø1" iris (4) (Thorlabs, cat. no. ID25)
- Rail carrier (4) (Thorlabs, cat. no. RC1)
- Ø1/2" post (2") (7) (Thorlabs, cat. no. TR2)
- Ø1/2" post holder (2") (6) (Thorlabs, cat. no. PH2-ST)
- Standard base (5) (Thorlabs, cat. no. BA2)
- Ultra-stable kinematic Ø1" mirror mount (1) (Thorlabs, cat. no KS1)

Microscope optics

- High-NA objective lens for laser surgery (1). NA greater than 0.7 recommended. Examples: Mag: 20×, NA: 0.75, air lens (Nikon, cat. no. MRD00200). For work in *C. elegans* and *Danio rerio* axotomy, a 20×, NA: 0.75 objective provides a suitable balance between field of view and NA for rapid and reliable axotomy. If a different objective is used, the focal lengths of lenses L1 and L2 may need to be altered as discussed in Step 43 of the protocol below.

- Fluorescence filter cube for use with the fluorescent reporter protein expressed by the organism (1) (For GFP, Nikon HQ:F, Nikon)

- Optical notch filter at the laser wavelength (1) (Thorlabs, cat. no. FES0700)

- Standard square cage plate, SM1 threaded inner bore (1) (Thorlabs, cat. no. CP02)

- Epi and bright-field shutters (1) (Sutter, cat. no. LB-SC and IQ25-SA)

A.3 A note on laser safety

Before initiating the protocol, ensure that the appropriate 'Laser in Use' safety signs are installed at the proper locations. In addition, the laser warning system as well as the laser system itself must comply with the relevant institutional, local and national laser safety guidelines. It is important to observe good laser safety practice, including not wearing reflective items such as jewelry and wristwatches when working near the laser. Do not look through the microscope eyepieces when the laser is on and when either the internal laser shutter or the safety shutter is open. Use beam blocks to safely terminate the laser beam while aligning. The laser should be shuttered while inserting components into the beam path. When installing a component into the beam path, use the IR card and/or IR viewer to visualize the location of the beam. Close either the internal laser shutter or the safety shutter (depending on the component location) and then place the component in the path. Following this, open the shutter and view the location of the beam in relation to the component being aligned. Close the necessary shutter and make more adjustments. If necessary, repeat this on/view-off/adjust cycle multiple times to obtain satisfactory alignment.

A.4 Procedure[4]

A.4.1 Setting up the optical table, laser, power meter, microscope and optical isolator

Timing: 6 h

1. Install the optical table (this should be done by the manufacturer).

2. Install the femtosecond laser system such that the beam is aligned down the center of the optical table (this should be done by the manufacturer).

3. Install the microscope body and supporting equipment at least 1.5 m from the output of the laser to allow sufficient room for the beam-conditioning optics (installation of the microscope should be done by the manufacturer).

4. Attach the optical power detector to the power meter. Mount the detector on one of the Ø1/2" posts and insert the post into a Ø1/2" post holder mounted on a standard base (BA2) for easy insertion and positioning of the detector in the beam path. Turn on the attenuator in front of the optical power detector to avoid damage (see manufacturer's manual for details). The optical power meter should be brought to zero to calibrate it for ambient radiation[5].

5. Turn on the laser, leaving the internal shutter closed and allow it to warm up. Set the laser wavelength to 800 nm.

6. Set the output power of the laser to a low yet stable level (~150 mW) and ensure that the laser is not pulsing. This state of the laser is used for aligning optical components in steps below[6].

7. Install the optical isolator[7] (Component B in Figure A-1) with its mounting hard-

[4]**Important note: These steps are time independent and may be stopped and started when necessary; however, it is imperative that the laser is either properly shuttered or turned off when not in use.**

[5]**Caution:** It is critical both for user and equipment safety that the power meter is accurately calibrated.

[6]**Caution:** Do not allow the output power of the laser to exceed 200 mW.

[7]**Caution:** The optical isolator contains a powerful magnet that can attract metallic tools such as screwdrivers during installation, thus causing damage. It is also imperative that sufficient beam block assemblies, composed of one beam block with post (LB1) and one 2" high universal post holder, are placed around the isolator to absorb any beams reflected from the crystal surfaces of the isolator as shown in Figure A-1 by the dashed orange lines. The placement and number of beam blocks is dependent to the alignment of the optical isolator.

ware in front of the laser to eliminate back reflections (follow the instructions of the manufacturer for alignment). The optical isolator prevents reflection back into the femtosecond laser, which can result in instabilities in the output power and disrupt mode-locking.

A.4.2 Installing the equipment to control the laser power

Timing: 2 h

8. Install the half-wave plate (Component C in Figure A-1) using the high precision rotation mount, one Ø1/2" post, one Ø1/2" post holder and a standard base (BA2) at the output of the optical isolator. Rotate the half-wave plate mount to the 0 position.

9. Install the Glan-Thompson polarizer (Component D in Figure A-1) using the polarizing prism mount, the kinematic mount for thin Ø1" optics, one Ø1/2" post, one Ø1/2" post holder and a standard base (BA2). Place a beam block assembly to absorb the rejected beam.

10. Install the EOM (Component E in Figure A-1) (or high-speed shutter; see equipment list), and place a beam block assembly to absorb the rejected beam. Follow the installation instructions of the manufacturer[8].

11. Install the HV amplifier (if using EOM), but do not turn it on. Connect the HV amplifier to the EOM using the included HV-rated cables[9].

12. Use a T-joint connector and two 50- BNC cables to connect the output of the function generator both to the input port of the HV amplifier (or high-speed shutter controller) and also to the input of the oscilloscope. To visualize single electrical pulses on the oscilloscope screen, set the oscilloscope to trigger and hold on the rising edge at 0.5 V. Consult the oscilloscope manufacturer's manual for detailed operation instructions.

13. Set the function generator to produce a square pulse with a 2.2 ms duration and 1.0 V amplitude (or the voltage required by the high-speed shutter control). Consult the

[8]**Caution:** When aligning the EOM, 200 mW or less average laser power must be used to avoid damage.
[9]**Caution:** The HV-rated cables look similar to standard low-voltage-rated BNC cables. Using improperly rated cables increases the risk of electrocution and may damage equipment.

function generator manufacturer's manual for detailed operation instructions.

14. Mount the safety shutter using one Ø1/2" post, one Ø1/2" post holder and a standard base (BA2) as well as a beam block assembly to serve as a rejected beam dump (Components F in Figure A-1). Using the IR card and IR viewer, adjust the position of the safety shutter and the beam block such that the beam is not clipped when the safety shutter is open and the beam is reflected into the center of the beam block when the safety shutter is closed.

15. Close both the internal laser shutter and the safety shutter.

16. Turn the laser to its maximum emission power and ensure that it is pulsing. For the Mai Tai HP laser the expected maximum emission power is approximately 3.0 watts at 800 nm.

17. Place the optical power detector at the output of the EOM. Turn on the HV amplifier. Open the internal laser shutter and adjust the position of the detector to maximize the power displayed on the meter.

18. Adjust the bias voltage of the HV amplifier until the measured power reaches its minimum.

19. Turn off the HV supply.

20. Rotate the half-wave plate (Component C in Figure A-1) until the power measured is appropriate for surgery: for axotomy in C. elegans, 1.2 W is sufficient when using a 20× objective lens with NA=0.75 and a 2.2 ms exposure time. For higher NA objectves or longer exposure times, lower power levels are sufficient [88].

21. Turn on the HV amplifier and record the value on the power meter. This is the minimum amount of transmitted laser power. The ratio of the power set in Step 20 to this value gives the contrast ratio of the laser power at the sample. A ratio of at least 50 is desirable.

22. Close the internal laser shutter.

23. Remove the power detector from the beam path.

A.4.3 Assembly of the dichroic mounting adapter

Timing: 1 h and a 24-h pause

24. The dichroic mounting adapter, shown in detail in Figure A-2, is composed of the dichroic mirror, the Nikon adapter plate from the 70 mm stage-up kit for a Nikon Eclipse TI, one Ø1" (1") pedestal pillar post, one compact kinematic mount, one standard base (BA1), one dichroic cube holder. The dichroic mounting adapter directs the laser beam into the objective lens without interfering with the normal optical paths of the microscope.

25. Mount the dichroic mirror in the dichroic cube holder[10].

26. Glue the dichroic cube holder to the standard base (BA1) using two-part epoxy following the diagram in Figure A-2.

27. Glue the compact kinematic mount to the standard base using two-part epoxy following the diagram in Figure A-2[11].

28. Attach the pedestal pillar post to the compact kinematic mount using one #8-32 × 1/4" set screw.

29. Hold the dichroic cube holder so that the dichroic mirror is centered above the large hole in the Nikon adapter plate. Use a marker to draw a circle on the Nikon adapter plate around the bottom of the pedestal pillar post.

30. Using a hand-held power drill, make a 0.25" hole in the Nikon adapter plate at the center of the marked circle as shown in Figure A-2.

31. Use a low-profile #8-32 × 1/4" screw to attach the pedestal post to the dust cover through the hole drilled in Step 30.

32. Attach the completed dichroic mounting adapter (Component N in Figure A-1) to the top of the microscope's fluorescent filter turret (Component P in Figure A-1) using the screws and hardware included in the 70-mm stage-up kit.

[10]**Critical step:** Ensure that the coated side of the dichroic mirror is facing the laser.

[11]**Critical step:** To ensure that the components are glued properly, place the assembly upside-down on a flat surface overnight while the epoxy cures.

A.4.4 Assembly of the periscope

Timing: 1 h

33. Construct a periscope (Component I in Figure A-1) using one Ø1.5" mounting post, one BA2 standard base, two right-angle kinematic cage mounts, two Ø1" gold mirrors and two Ø1.5" post mounting clamps. Place the periscope assembly on the optical table as shown in Figure A-1 so that it will be able to direct the beam into the laser entry port of the microscope.

34. Install a Ø1" gold mirror in the ultra-stable kinematic Ø1" mirror mount.

35. Repeat Step 6 to lower the laser output power.

36. Turn off the HV amplifier.

37. Mount the ultra-stable kinematic Ø1" mirror mount using a one Ø1/2" post, one Ø1/2" post holder and a standard base (BA2) (Component G in Figure A-1) on the optical table. Open the internal laser shutter and the safety shutter. Coarsely align the kinematic mirror to center the laser on the periscope's lower mirror. Close the safety shutter and secure the kinematic mirror to the optical table.

38. Place a Ø1" iris at the input of the periscope (Component H in Figure A-1). This iris will ease the process of realignment when needed.

39. Coarsely align the periscope to direct the laser horizontally into the back port of the microscope.

40. Adjust the angle of the lower periscope mirror to center the laser on the upper periscope mirror.

41. It may be necessary to repeat Steps 37-40 several times iteratively to obtain a satisfactory alignment.

42. Close both the safety shutter and the internal laser shutter.

A.4.5 Assembly of the laser beam expander

Timing: 1 h

43. Determine the focal lengths of lenses L1 and L2 needed to fill the back aperture of the objective used for axotomy. In this protocol, the laser beam diameter of 3 mm must be expanded to fill the 15-mm-in-diameter back aperture of the objective lens, and therefore the beam must be expanded fivefold. The amount of expansion is determined by the ratio of the focal length of lens L2 to that of lens L1, which in this protocol is 200 mm/40 mm=5. The distance between the lenses is the sum of their focal lengths f_1 and f_2 as shown in Figure A-3, which in this protocol is 40 mm + 200 mm=240 mm.

44. Construct the beam expander following the diagram in Figure A-4 using two Ø1.5" mounting posts, two standard bases (BA2), two Ø1.5" post mounting clamps, one 12" optical rail, three rail carriers, one single-axis position stage with micrometer, one Ø1" translating lens mount, one Ø2" lens mount and four Ø1/2" post holders.

45. Place the beam expander on the optical table next to the microscope as shown in Figure A-1. Positioning of the beam expander optics close to the microscope in this manner provides two benefits: first, it allows for a single person to (re)align the setup, thus facilitating quick troubleshooting. Second, it reduces the amount of real estate on the optical table consumed by the optics and supporting hardware.

46. Use a bubble level to ensure the 12" optical rail is level. The rail carriers slide onto the optical rail and are hand-tightened with the included screws. The single-axis position stage with micrometer is mounted using cap screws.

47. Space the outer Ø1/2" post holders by a distance equal to $f_1 + f_2$. The distance between these two Ø1/2" post holders is finely adjusted below in the protocol.

48. Lower the laser power as in Step 6.

49. Completely close the iris closest to the objective. Close the remaining two irises leaving an aperture of approximately 5 mm.

50. With the aid of the IR viewer and IR card, adjust both the height and the angle of the upper periscope mirror until the laser beam passes through the two open irises.

51. Open all three irises.

52. Center the beam on the dichroic mirror by adjusting only the height of the upper periscope mirror and the position of the periscope assembly on the optical table. If the periscope assembly is displaced, repeat Steps 37-40 to recenter the beam on the lower periscope mirror.

53. Close all three irises leaving an aperture of approximately 5 mm. Adjust the height of the 12" optical rail until the laser passes through all three irises. Use a bubble level to ensure the 12" optical rail is level.

54. Close both the safety shutter and the internal laser shutter.

A.4.6 Coarse alignment of the laser

Timing: 30 min

55. Construct the IR alignment tool by drilling[12] a 1/8" diameter hole through the center of the RMS-threaded IR alignment disk and then insert the modified IR alignment disk into an RMS 45 to CFI 60 objective adapter.

56. Thread the completed IR alignment tool into the microscope nosepiece.

57. Place a cover glass on the stage plate to act as a reflecting surface for laser alignment.

58. Lower the laser power for alignment as in Step 6.

59. Tilt the condenser arm away from the stage to facilitate viewing of the IR alignment tool.

60. Open the internal laser shutter and the safety shutter.

61. Using the IR viewer, observe[13] the top of the IR alignment tool as shown in Figure A-5.

62. If the laser is not passing through the center hole then a glowing dot will appear on the surface of the IR alignment tool as shown in Figure A-5a. Use the compact kinematic mount of the dichroic mounting adapter to center the laser on the IR alignment tool.

[12] **Caution:** The alignment disk is built from brittle plastic so drilling must be done with care.

[13] **Caution:** Do not hold the IR viewer directly in the beam path as this could result in damage to the IR viewer.

63. If the laser beam is not normal to the cover glass two spots will appear on the surface of the IR alignment tool as shown in Figure A-5b: a glowing ring around the center hole (the 'transmitted beam spot') and a spot off to the side (the 'reflected beam spot').

64. Note the location of the reflected beam spot.

65. Adjust the angle of the upper periscope mirror to move the transmitted beam spot approximately half the distance towards the initial location of the reflected beam spot (from the previous step). In doing this, the reflected beam spot will itself move and may disappear, as the transmitted beam is no longer passing through to the center hole.

66. Adjust the angle of the dichroic mirror using the compact kinematic mount of the dichroic mounting adapter to bring the transmitted beam spot back to the center hole. The reflected beam spot should move back towards the center hole at approximately twice the rate as the transmitted beam spot, and they will meet in the middle as shown in Figure A-5c.

67. Close the safety shutter. Insert L2 making sure that the curved surface of the lens faces away from the objective.

68. Open the safety shutter. Using the IR viewer, observe the IR alignment tool and center the transmitted beam spot by adjusting the position and pitch of L2.

69. Close the safety shutter. Insert L1 making sure that the curved surface of the lens faces L2.

70. Open the safety shutter. Using the IR viewer, observe the IR alignment tool and center the transmitted beam spot by adjusting the position and pitch of L1 using both the Ø1/2" post and the Ø1" translating lens mount. Note that the transmitted beam spot will be larger and diffuse after inserting L1 as shown in Figure A-5d. Ensure that the beam is not clipped (i.e., the transmitted beam spot should be a full, symmetric and circular disk on the IR alignment tool).? TROUBLESHOOTING.

71. Close the safety shutter and internal laser shutter.

A.4.7 Fine alignment of the laser and image focal planes

Timing: 1 h.

72. Insert the objective to be used for surgery. Make sure that no filter cube is in the active slot of the epifluorescence filter turret. Turn on the HV amplifier and adjust the half-wave plate as discussed in Steps 17-21.

73. Close the internal laser shutter and the safety shutter.

74. Draw lines on a clean cover glass using a non-water-based permanent marker (e.g., Sharpie)[14]. Place the cover glass on the stage plate.

75. Turn on the camera and image acquisition software.

76. Open the internal laser shutter and the safety shutter.

77. Locate the image of the laser in the preview window of the image acquisition software. Center the beam in the preview window by adjusting the angle of the dichroic mirror using the compact kinematic mount of the dichroic mounting adapter.? TROUBLESHOOTING.

78. Mark the position of the laser on the computer monitor with a piece of tape[15].

79. Close the internal laser shutter and the safety shutter.

80. Insert the laser notch filter into a 30 mm-standard square cage plate.

81. Place the laser notch filter between the dichroic mirror and the microscope epifluorescence filter turret.

82. Tilt the condenser arm to its original upright position. Turn on the bright field source, adjust the exposure of the camera and focus on the edge of a marker line. Move the stage to position the edge of a marker line under the piece of tape on the computer monitor.

[14] **Critical step:** Use only a single pass with the marker, as a thick coating will not allow the laser to produce thin cuts.

[15] **Critical step:** Do not move the image acquisition software preview window after marking the beam location.

83. Open the safety shutter. Depending on the locations of L1 and L2 set in Steps 68-70 the region of marker underneath the tape will be ablated to varying degrees of sharpness, symmetry and size. While staying focused on the edge of the marker line, adjust the position of L1 along the optical rail using the micrometer to adjust the focus of the laser beam to increase the sharpness of the ablation. In addition, adjust L1 using its translating mount axes to further improve the shape of the ablation.? TROUBLESHOOTING.

84. Characterize the laser alignment by using the single-pulse button on the function generator to generate spots and compare the result to the image in Figure A-6. When the system is properly aligned, the cutting patterns shown in Figure A-6 should be ~3 µm wide and the firing patterns should be ~9 µm across. Note that these values have been found to be suitable for axotomy in *C. elegans* using a 20×, NA: 0.75 objective.

85. Close the safety shutter and the internal laser shutter.

A.4.8 *In vivo* laser axotomy on *C. elegans*[16]

Timing: 25 min

86. Prepare the microscope for fluorescence imaging and remove the laser notch filter (1 min).

87. Turn on the HV amplifier and adjust the half-wave plate as discussed in Steps 17-21 (3 min).

88. Open the internal laser shutter and the safety shutter (2 min).

89. Locate the image of the laser in the preview window of the image acquisition software and adjust the piece of tape on the monitor if necessary (2 min).

90. Close the safety shutter and return the laser notch filter to its position above the microscope filter turret (2 min).

[16] **A note on timing: These steps are strongly time dependent and must be completed within 2 h once the anesthetic has been administered to ensure minimal toxic effects (*C. elegans*). The rapid development cycle of the animals may influence the biological process under study, so care should be taken to ensure that the animal is in the proper developmental stage.**

91. Immobilize an animal on a cover glass using standard procedures [145]. Place the cover glass on the stage plate. Ensure that the animal is as close to the cover glass as possible (5 min).

92. Using fluorescence imaging, locate the animal and move the stage to bring the axon or cell to be ablated directly under the piece of tape. Bring the target axon or cell into focus (< 30 s).

93. Open the safety shutter and adjust the focus to achieve two-photon fluorescence of the target axon, indicative of proper focusing. Adjust stage position and focus if necessary (< 30 s).

94. Press the single-pulse button on the function generator to ablate the target axon or cell. Immediately close the safety shutter to avoid damaging the organism/cell (< 10 s).? TROUBLESHOOTING.

95. Recover the animal using standard procedures [145] (5 min).

96. At the end of the experiment, close the safety shutter and internal laser shutter. Turn off the laser and the fluorescence and bright field sources (3 min).

A.5 Timing

A.6 Troubleshooting

Troubleshooting advice can be found in Table A.3.

Table A.2: Time required for assembly of femtosecond laser system.

Steps	Description	Time Required
1-7	Setting up the optical table, laser, power meter, microscope and optical isolator	6 h
8-23	Installing the equipment to control the laser power	2 h
24-32	Assembly of the dichroic mounting adapter	1 h + 24 h pause
33-42	Assembly of the periscope	1 h
43-54	Assembly of the laser beam expander	1 h
55-71	Coarse alignment of the laser	30 min
72-85	Fine alignment of the laser and image focal planes	1 h
86-96	*In vivo* laser axotomy on *C. elegans*	25 min

Table A.3: Troubleshooting table.

Step	Problem	Possible reason	Solution
16	Laser is not pulsing	Optical isolator is not functioning properly, allowing back reflections into the laser	Check optical isolator manual and ensure the component is aligned correctly

Continued on Next Page...

Table A.3 – Continued

Step	Problem	Possible reason	Solution
		Laser power is set too low	Check the power output of the laser
21	Power ratio at electro-optic modulator (EOM) is insufficient	EOM is misaligned or damaged	Realign and/or consult manufacturer
		Bias voltage for high-voltage (HV) amplifier is incorrect	Repeat Step 18
53	The laser beam will not pass through all three irises	The 12" optical rail is not parallel to the beam path	Carefully rotate the entire beam expander structure to bring the 12" optical rail parallel to the beam path
62	Cannot find laser spot on the infrared (IR) alignment tool	Dichroic mirror is severely misaligned	Adjust the rotation of the Ø1" pedestal post holding dichroic and/or compact kinematic mount on the adapter plate and realign

Continued on Next Page...

Table A.3 – Continued

Step	Problem	Possible reason	Solution
65, 66	Transmitted beam spot disappears as it is moved	The beam is being clipped	Adjust the position and/or rotation of the Ø1" pedestal pillar post; if insufficient, realign the periscope, beam expander and dichroic mounting adapter
68	The beam spot cannot be properly centered using only L2	The laser beam is not passing through the center of L2	Adjust the beam expander hardware, in particular the height of the 12" optical rail from the table
70	Expanded beam shape is asymmetric or irregular in shape	Clipping of the beam and/or poor orientation of the lenses	Check alignment using IR viewer and IR card and correct the misaligned components
77	Cannot find laser in preview window	Beam may not be falling on the CCD of the camera	Rotate the camera in its mount if the sensitive area is particularly small
		Filter cube may be in the active slot of the epifluorescence filter turret and may be blocking the laser beam	Remove the filter cube

Continued on Next Page...

Table A.3 – Continued

Step	Problem	Possible reason	Solution
83	Cannot obtain sharp cuts on the permanent marker	Imaging and laser plane of focus are mismatched	Find both planes of focus; if the laser plane of focus is below the imaging plane, move L1 closer to L2 with the micrometer; if laser focus is above, move lenses apart
		Laser is not pulsing	Change the settings of the laser to pulsing mode or go to troubleshooting of Step 16
84	Firing pattern is asymmetric or large	Clipping of laser beam	Trace the beam path using the IR card to determine the point of clipping and correct the misalignment
		Misalignment of lenses	Realign the lenses
		Laser is not focused on the image plane	Adjust the position of L1 along the 12" optical rail using the micrometer
		Power level is too high	Verify the high-power level using Steps 17-21

Continued on Next Page...

Table A.3 – Continued

Step	Problem	Possible reason	Solution
		Laser is not centered on or overfilling the back aperture of the objective lens	Redo Steps 63-71 to correctly align the incoming beam on the back aperture of the objective
	The position of cuts shifts when focusing	Non-normal incidence of laser beam onto the back aperture of the objective	Redo Steps 62-66 to correctly orient the incoming beam
89	Laser spot has moved significantly since last usage	The alignment of components have changed	Check alignment using IR viewer and IR card and correct the misaligned components
94	Failure to successfully ablate the target	Laser is not focused on the image plane	Repeat Steps 72-85
		Energy of the laser is too low	Check maximum power of the beam using power detector at the output of the EOM; see Step 17

Continued on Next Page...

Table A.3 – Continued

Step	Problem	Possible reason	Solution
		Target is too deep in the tissue for efficient cutting; excessive scattering	Reorient the sample
		Numerical aperture (NA) of the objective is too low	Use objectives with higher NA
		Laser is not pulsing	Change the settings of the laser to pulsing mode or go to troubleshooting of Step 16
		Significant laser pulse dispersion	Analyze the entire beam path for portions which may be causing significant dispersion and adjust/replace components with ones suited for high-speed near infrared (NIR) lasers
	Specimen is damaged at low power, even when not firing	Minimum transmitted power is too high	Check/correct EOM bias voltage and the rotational angle of the half-wave plate

A.7 Anticipated results

A.7.1 Characterization of the femtosecond laser surgery system

The setup described in this protocol produces a circular laser spot with a full-width at half-maximum (FWHM) of 1.7 µm at the focal plane (see Figure A-7). An objective with a higher NA can be used to generate a smaller laser spot size at the expense of the working distance and/or the field of view. Using the components described in this protocol, the total power loss between the output of the EOM and the sample is 47.5%.

A.7.2 Axotomy of *C. elegans* mechanosensory neurons

With a 20× (NA=0.75) objective, we use a 1.20 W (measured at the output of the EOM, which corresponds to 0.63 watts at the sample), 2.2 ms-long laser pulse train to carry out axotomy on *C. elegans* zdIs5 strain (GFP-labeled mechanosensory neurons) (see Figure A-8). Although low-magnification objective lenses have smaller NAs, they allow simultaneous visualization of the cell body and large portions of the axons, enabling surgery of the axons at precisely measured distances from the soma.

Lower laser power and shorter pulse trains can be used; however, the reproducibility of surgery decreases at lower powers in part because of increased sensitivity to laser focus [88]. In addition, it becomes difficult to distinguish photodamage from photobleaching. Photobleaching is often followed by spontaneous recovery of fluorescence in the axon at the site of injury within a few minutes, whereas photodamage leads to permanent non-fluorescent regions. The threshold power levels for photobleaching versus photodamage can be characterized using dye-filling techniques [72, 73]. Conversely, higher laser powers and/or longer pulse trains often result in extensive scarring, causing widespread injury to the animal [73, 88, 146].

Upon ablation, we often briefly observe fluorescent protein leaking from the axon terminals and diffusing into the surrounding area. The brightness of the axon terminals decreases initially, and recovers within several minutes, leaving a non-fluorescent region at the site of surgery. Within several minutes both the proximal and distal axon terminals retract by several microns (arrow 2 in Figure A-8b). Within a few hours, the proximal axon terminal starts regrowing (arrow 3 in Figure A-8b) [73]. The regrowing proximal axon terminal may also fuse with the distal axon terminal [73].

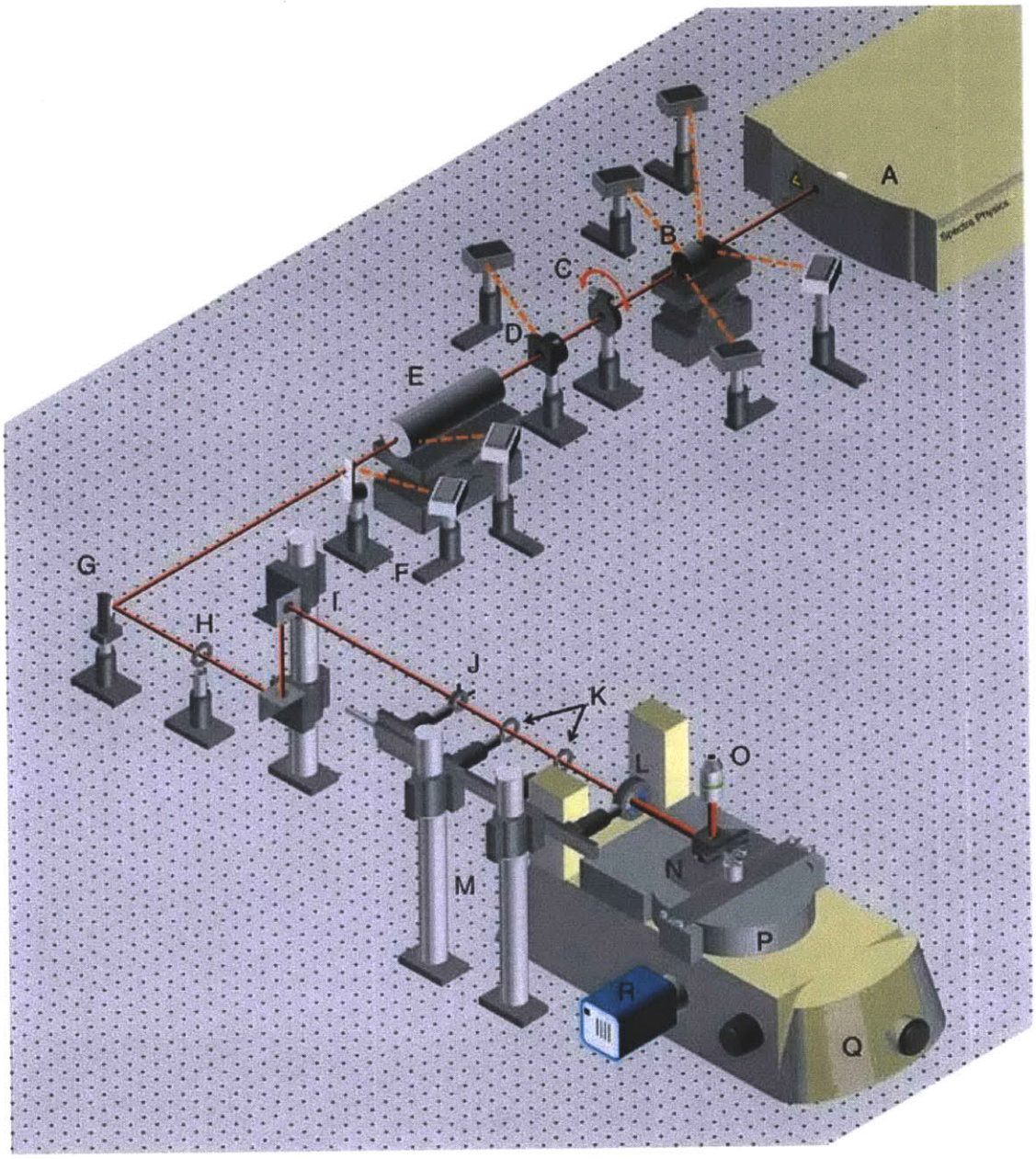

Figure A-1: Optical system layout. See Table A.1 for full component list.

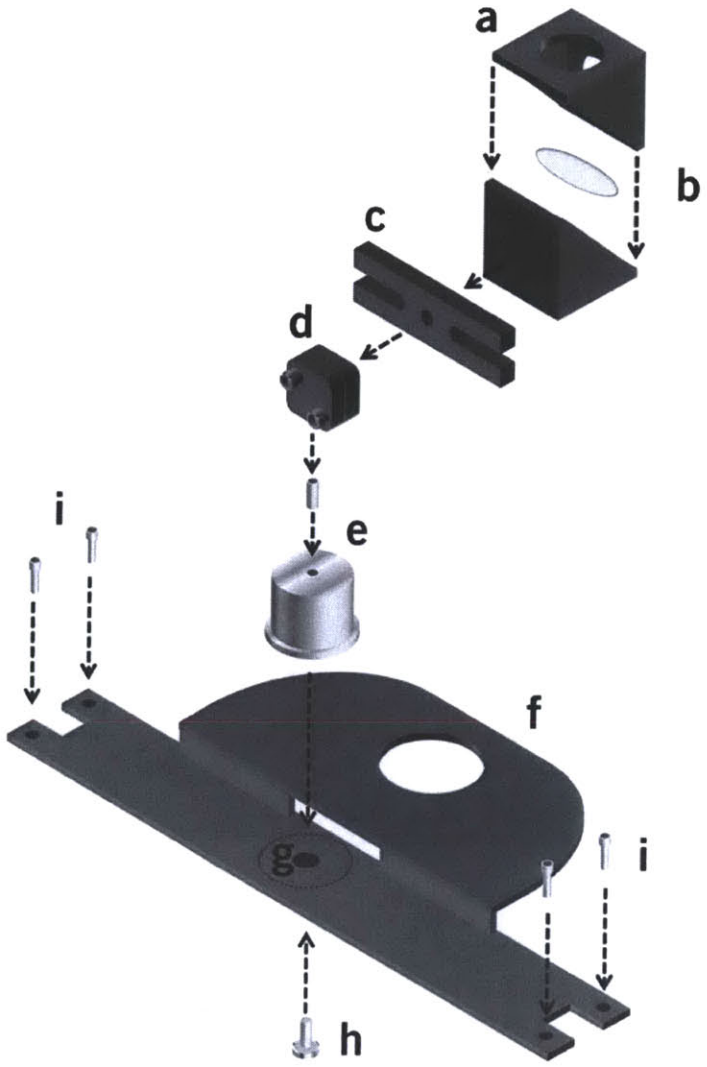

Figure A-2: An exploded view of the dichroic mounting adapter. (a-b) (a) The dichroic mounting adapter is composed of a metal filter cube, which contains an infrared (IR) dichroic mirror (b). (c) The filter cube is attached to a BA1 standard base using glue. (d) The opposite face of the BA1 standard base attaches to a two-axis compact kinematic mount also using glue. (e) The compact kinematic mount is attached to a Ø1" (1") pedestal pillar post with a #8-32 × 1/4" set screw. (f) The assembly comprising components a-e mounts to a Nikon adapter plate from a 70 mm stage-up kit so that the dichroic mirror sits in the beam path. (g-h) (g) This is accomplished by drilling a hole and using a #8-32 × 1/4" screw (h) to position the dichroic mirror over the opening in the adapter plate. (i) The entire assembly is affixed to the microscope using screws included in the 70 mm stage-up kit. Figure A-1 shows the location of the dichroic mounting adapter on the microscope.

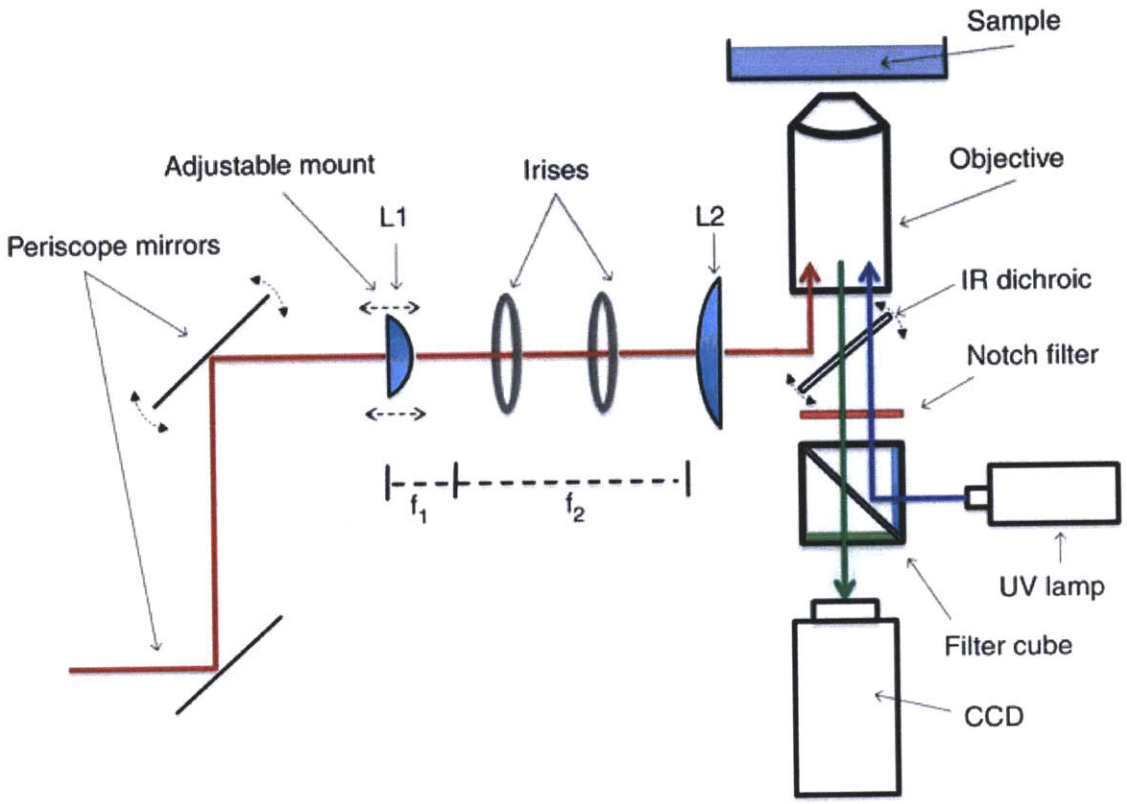

Figure A-3: Optical path for simultaneous epifluorescence imaging and laser axotomy. The femtosecond laser, indicated by the red line, passes through beam conditioning optics before being directed up by the near infrared (NIR) dichroic mirror into the back aperture of the objective lens. The epifluorescence excitation, indicated by the blue line, is simultaneously directed into the back aperture of the objective lens by the filter cube. The fluorescence emission, indicated by the green line, passes through multiple filters and is captured by the camera.

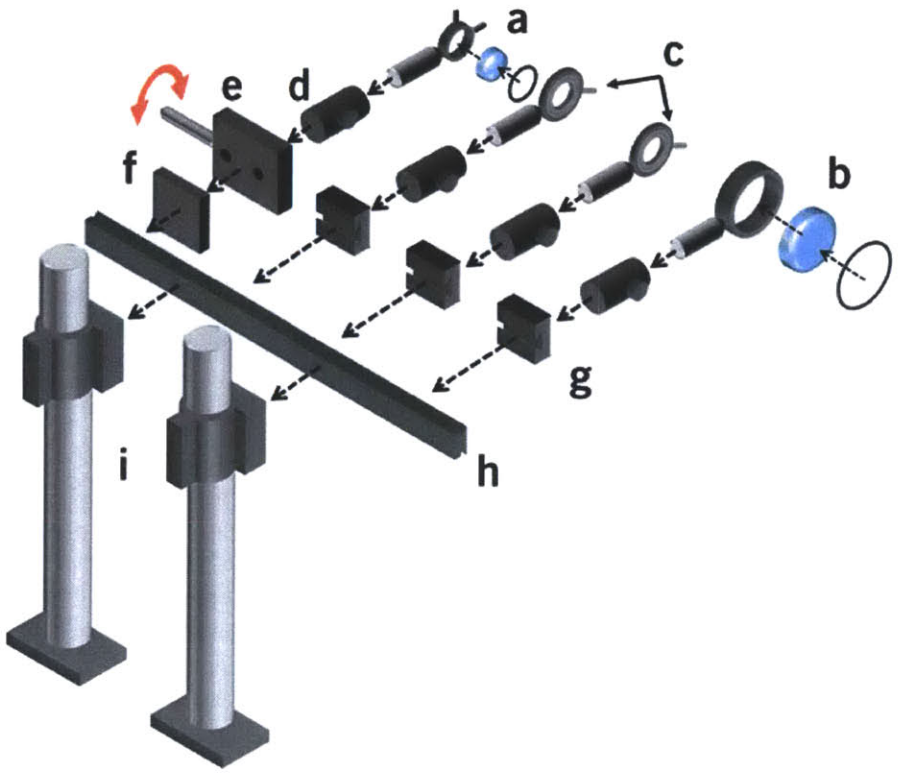

Figure A-4: An exploded view of the beam expander. Lenses L1 and L2 (a and b, respectively) sit in their mounts that are attached to Ø1/2" posts. Two Ø1" irises (c) are also attached to Ø1/2" posts. All four posts sit securely in Ø1/2" post holders (d), one of which is attached to a single-axis stage (e) with rotatable micrometer and Ø1.5" post clamp adapter plate (f), whereas the remaining three are attached to rail carriers (g). These four assemblies firmly attach to the 12" optical rail (h) which is mounted to the two Ø1.5" posts by two Ø1.5" post mounting clamps (i). The entire assembly is mounted using BA2 standard bases.

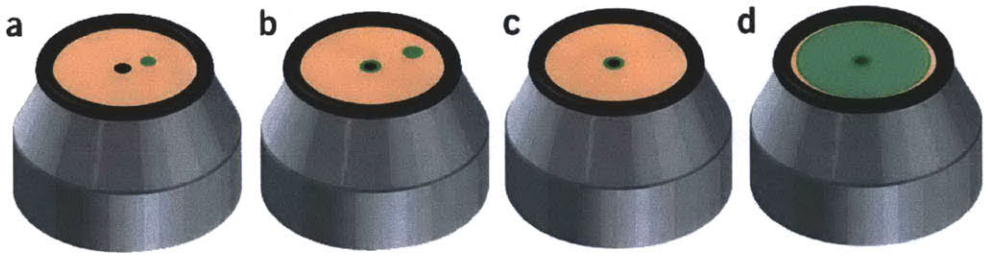

Figure A-5: Use of the infrared (IR) alignment tool. The IR alignment tool is composed of an RMS IR-aligning disk and an RMS 45 to CFI 60 objective adapter. (a) Without lenses L1 and L2, the transmitted beam is directed to the center of the dichroic mirror, thus resulting in a glowing spot on the field of the disk. (b) Adjusting the dichroic mirror causes the transmitted beam to pass through the center hole and an additional spot caused by the reflection of the beam from the cover glass appears on the field of the disk. The reflected spot is caused by the non-normal incidence of the transmitted beam on the cover glass. Moving the transmitted spot half-way towards the initial location of the reflected spot by adjusting the upper periscope mirror and then moving the transmitted spot back to the center hole by adjusting the angle of the dichroic mirror, achieves normal incidence of the beam on the cover glass. (c) Normal incidence is indicated by both reflected and transmitted beams passing through the center. (d) Inserting both lenses L1 and L2 into the beam path (Steps 68-70), results in a large, symmetric circular illumination on the IR alignment tool.

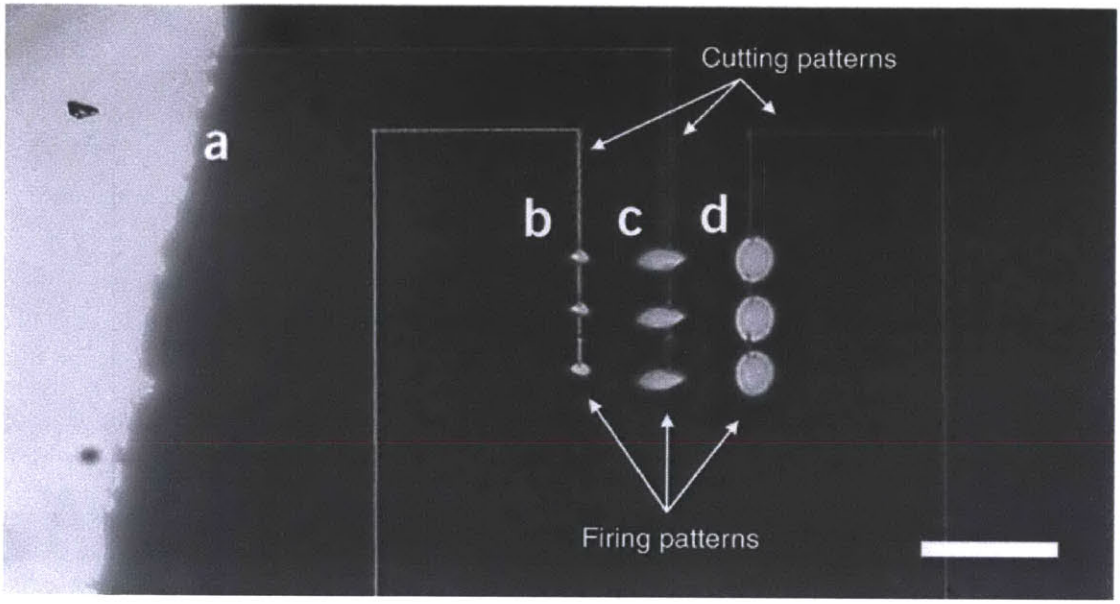

Figure A-6: Ablated patterns in permanent marker on cover glass under different alignment conditions. (a,b) When the image plane is focused on the boundary of the marked and unmarked glass surfaces, and when the system is properly aligned, the resulting cutting pattern is narrow and symmetric (a), whereas the firing pattern is relatively small and also symmetric (b). If the beam is clipped and/or lenses L1 and L2 are misaligned, the cutting pattern is wider in one direction than the orthogonal direction (c). In addition, the firing pattern becomes asymmetric. If the laser is out of focus, the cutting pattern is blurred and the firing pattern is larger (d). Scale bar: 50 μm.

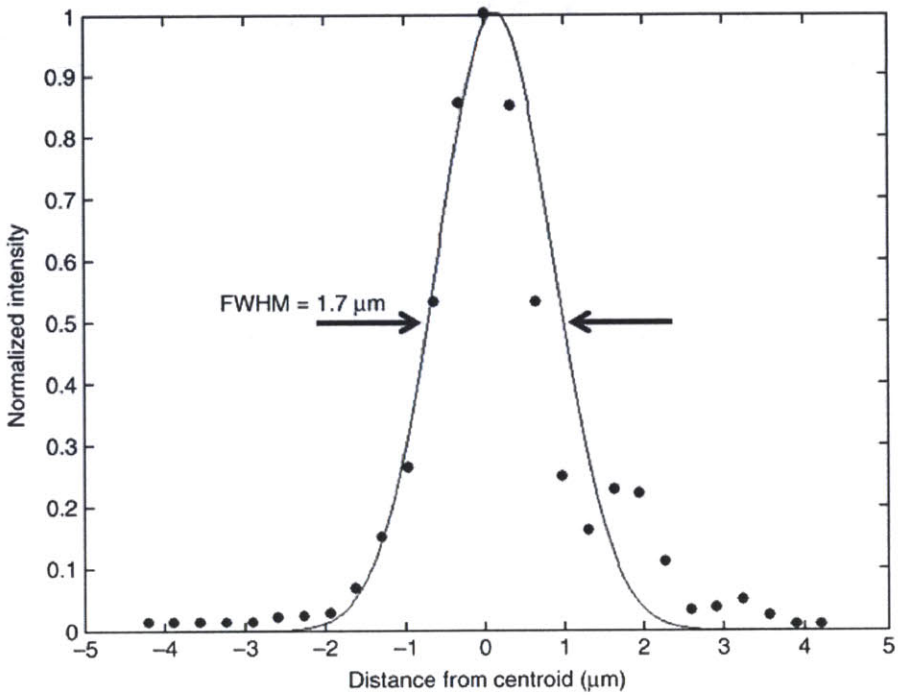

Figure A-7: Point spread function of the laser at the focal plane. The system described in this protocol generates a circular laser spot at the sample with a full width at half-maximum of 1.7 µm.

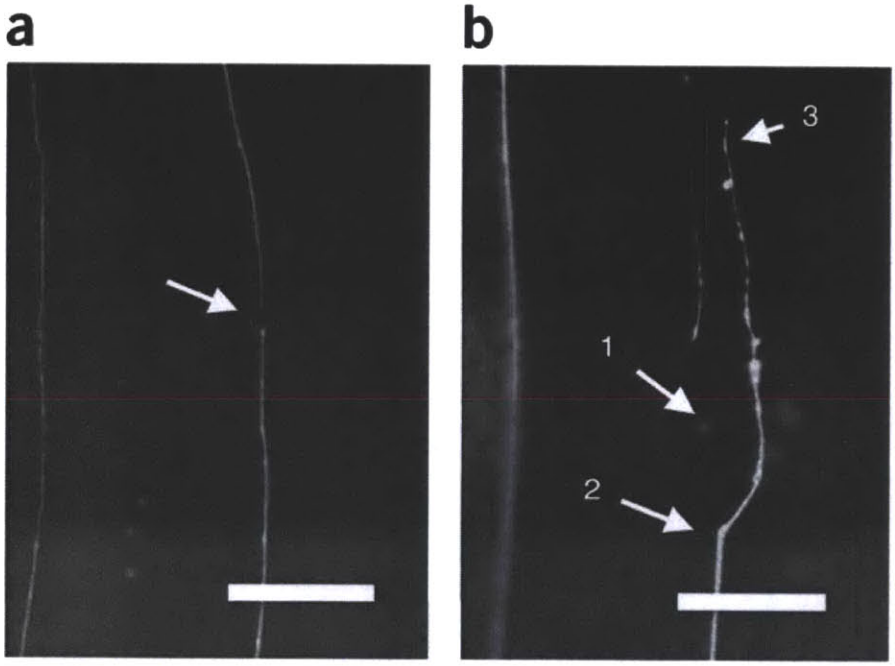

Figure A-8: Femtosecond laser microsurgery. (a) A highly localized region (arrow) of a *Caenorhabditis elegans* mechanosensory neuron is ablated using the system described in this protocol. (b) Following surgery at point 1, the ablated process first retracts to point 2 and then regenerates to point 3. Scale bar: 10 µm.

Appendix B

Construction of simplified devices for microfluidic immobilization of physiologically active *C. elegans*[†]

Abstract

We present a procedure for building and operating a microfluidic device for mechanical immobilization of *Caenorhabditis elegans* in its physiologically active state. The system can be used for *in vivo* imaging of cellular processes such as neuronal regeneration, intracellular Ca^{2+} signaling, cell division and migration, as well as for laser microsurgery and multiphoton microscopy. The system consists of a transparent, two-layer silicone device, in which *C. elegans* is first linearly oriented, and then its motion is completely restrained by pressurizing a thin flexible membrane against the animal, and without using potentially harmful anesthetics, gases, or cooling procedures. The system can be installed on any microscope and operated by only one syringe and one external valve making it accessible to most laboratories. The devices can be fabricated and assembled with external fluidic

[†]**This chapter is an adaptation of the material found in [147]. Author contributions: C.B.R. and F.Z. developed and characterized the microfluidic immobilization procedure. C.L.G. engineered the immobilization technique for manual operation, developed troubleshooting techniques and wrote the paper. C.L.G. and C.B.R. developed the other elements of the system. M.F.Y. supervised the project at all stages.**

connectors within 3 d.

Key words: Caenorhabditis elegans, microfluidics, femtosecond laser microsurgery, immobilization and time-lapse imaging.

B.1 Introduction

The nematode *Caenorhabditis elegans* (*C. elegans*) is an extensively studied multi-cellular model organism, mainly due to its small size, optical transparency, rapid development, and amenable genetics. Many assays and manipulations on *C. elegans* require reversible immobilization of the animals. The most common and broadly used immobilization methods anesthetize nematodes on agarose pads with water-soluble chemicals [145]. However, anesthesia may affect the physiology of the animal [80] as well as cellular processes such as cell division, neurite growth, and calcium signaling. Cooling [81] and anesthesia by CO_2 [82] have also been used, although the physiological effects of these methods remain uncharacterized for many biological processes. Therefore, there is significant need for non-invasive and reversible immobilization techniques that enable imaging and manipulation of cellular processes at subcellular resolution.

The physiology of *C. elegans* and its ability to be cultured in liquid make it highly amenable to manipulation in microfluidic devices, and this procedure details the fabrication of such a device. The technique presented here also aligns animals in a linear orientation, simplifying cell tracking, image processing and comparisons between animals. In addition, this device allows the animals to be loaded and unloaded rapidly, and to be recovered quickly and reliably. The devices can immobilize animals at different ages during development by simply adjusting the pressure levels to accommodate animal sizes from L4 larval stage to fully-grown adult. For smaller animals, the dimensions of the device must be scaled down. Suggestions for this are given in the Experimental design section.

The system presented in this chapter can be installed on any inverted microscope and can be operated by only one syringe and one external valve, making it accessible to most laboratories. The animal to be immobilized is first loaded into the device (Figure B-1), which is composed of two PDMS (polydimethylsiloxane) layers i.e. **flow layer** and **compression layer**. These PDMS layers are bonded to each other, and the combined layers

are bonded to a dish with a cover glass bottom. The animal is transported within the **flow layer**, which contains a narrow channel array that allows fluid to pass while not letting the animals flow through. Thus, the animal is linearly oriented by the flow through the **channel array**. The **compression layer** contains a channel above the thin membrane that separates the two layers [148]. When the pressure in the **compression layer** is raised, the **immobilization membrane** expands into the **flow layer**, wrapping around the animal and completely restraining its movement. The animal can then be imaged and optically manipulated through the cover glass at the bottom of the chip via an inverted microscope. Afterwards, the pressure in the **compression layer** can be released, and the animal can be pushed out of the chip by reversing the flow through the channel array.

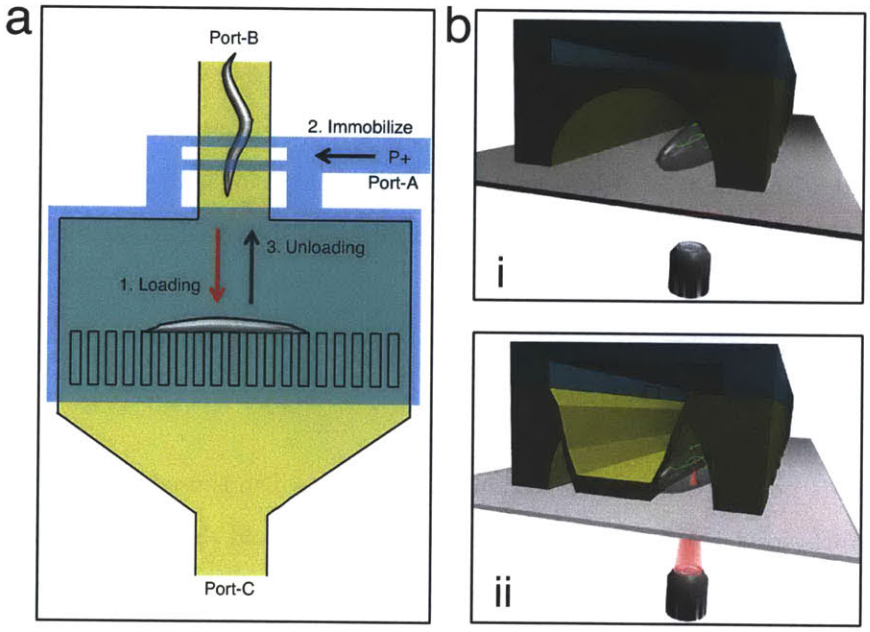

Figure B-1: Microfluidic chip for mechanical immobilization of *C. elegans*. (a) Diagram of the chip with numbered arrows showing *C. elegans* manipulation steps. 1: Loading of a nematode from the input/output **port-B** into the **flow layer** (yellow) and its restraint by a narrow **channel array**. 2: The animal is immobilized by pressurizing the **compression layer** (blue) via **port-A**, causing the **immobilization membrane** to flex into the **flow layer** (yellow). 3: Release and unloading from the chip. (b) Cross-section of the chip showing the immobilization method when (i) the **compression layer** (blue) is not pressurized, allowing the animal to be positioned and (ii) the **compression layer** is pressurized, restraining the animal's motion within the **flow layer** (yellow) enabling laser microsurgery through the cover glass.

B.1.1 Comparison with other methods

Alternative microfluidic methods for immobilizing *C. elegans* include flowing animals into narrow channels [96], cooling [97], and CO_2 [98]. The use of narrow channels to laterally trap animals has not been shown to provide sufficient immobilization stability for repeatable imaging at cellular resolution. Cooling affects dynamic cellular processes and the effects of CO_2 remain unknown. Guo *et al.* [95] also adapted a similar immobilization technique employing a membrane but three-dimensional imaging of cellular processes was not shown. The method described in this protocol allows immobilization of whole animals with subcellular-level stability, and three-dimensional two-photon images can be acquired even at slow acquisition rates [87]. The stability of the presented technique is due to the extensive optimization in thicknesses, flexibilities, and roundness of the channels and the membrane [87]. A simple immobilization technique employing agarose and polystyrene spheres [149] is also available. However, rapid and reliable recovery of animals without loss is challenging and the animals are also held in random orientations, complicating cell tracking and image analysis. Additionally, motility of physiologically-active animals was not quantified for applications requiring high immobilization stability such as three-dimensional confocal and two-photon imaging.

B.1.2 Experimental design

The procedure begins with the fabrication of **mold-C** (which is used to mold the aforementioned compression layer) and **mold-F** (which is used to mold the flow layer) by patterning silicon wafers with photoresists using optical masks (Figure B-3) along with tools and materials available in most university cleanrooms (Figure B-2a). Following photolithography, a thin layer of PDMS is spun onto **mold-F** (to form the **flow layer** (yellow) in Figure B-1a, and B-2b) and a thick layer of PDMS is poured onto the **mold-C** (to form the **compression layer** in Figure B-1a (blue), and B-2b). These PDMS layers are partially cured in an oven. The **compression layer** is peeled from **mold-C** and a hole is punched into the **compression layer** to provide fluidic access to the channels in that layer (Figure B-2c). The **compression** and **flow layers** are then aligned and bonded to each other by further thermal curing (Figure B-2c). Once these layers have bonded and then peeled from **mold-F**, two holes are then punched to access the channels in the **flow layer** (Figure B-2d).

The layers are then plasma bonded to a cover glass and thermally cured overnight (Figure B-2d). Finally, steel pins and tubing interface the completed chip to a manual valve for pressurizing the **compression layer** and to a syringe for loading and unloading animals (Figure B-2e). The steps involving photoresist patterning, PDMS, and plasma bonding include time dependent sequences as detailed in the Timing section.

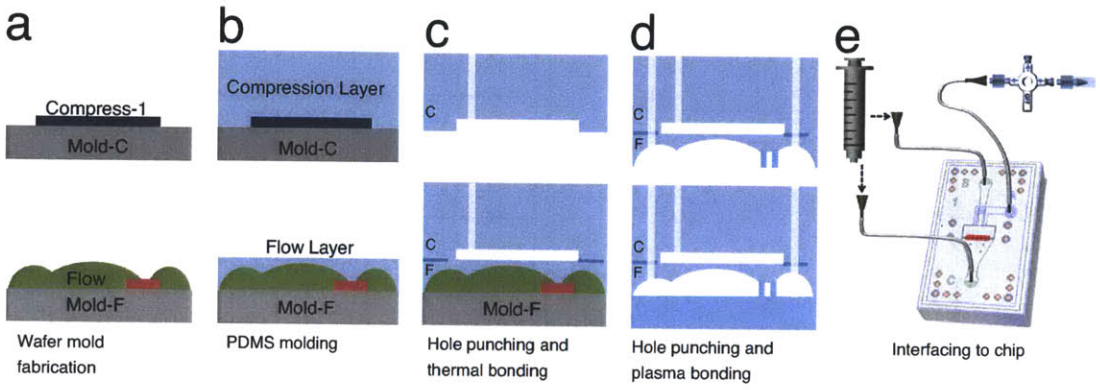

Figure B-2: Procedure overview. (a) Photolithography techniques are used to generate photoresist patterns on silicon wafers creating **mold-C** and **mold-F**. (b) Structures are then molded into PDMS layers using the wafer molds by pouring a thick layer onto **mold-C** and spin-coating a thin layer onto **mold-F** followed by curing in oven. (c) The PDMS layer is peeled from **mold-C** and a hole is punched to access the **compression layer**. This layer is then aligned onto the PDMS layer on **mold-F**. The PDMS layers are then baked in an oven overnight forming a strong thermal bond. (d) The combined PDMS layers are then peeled from **mold-F** and two holes are punched to access the **flow layer**. The combined PDMS structure is then plasma bonded to a dish with a cover glass bottom and baked overnight. Finally, the chip is interfaced with steel pins and connected with tubing to a syringe and a manual valve.

Three optical masks (either negative or positive) will be used to make the molds by optically patterning a thin layer of a light-sensitive polymer (i.e. photoresist) that is spin coated onto a silicon wafer as shown in Figure B-4a-c:

1. Negative masks **flow-1** (red) and **compress-1** (blue) will be used to pattern negative photoresist (i.e. the areas of photoresist exposed to UV light through the optical masks will be cross-linked. The regions that are not cross-linked will be dissolved during the photoresist development step). The negative masks should be transparent in the areas where the photoresist will remain on the wafer surface forming the mold.

2. Positive mask **flow-2** (green) will be used to pattern positive photoresist (i.e. the regions of photoresist exposed to UV light will be chemically broken and dissolved

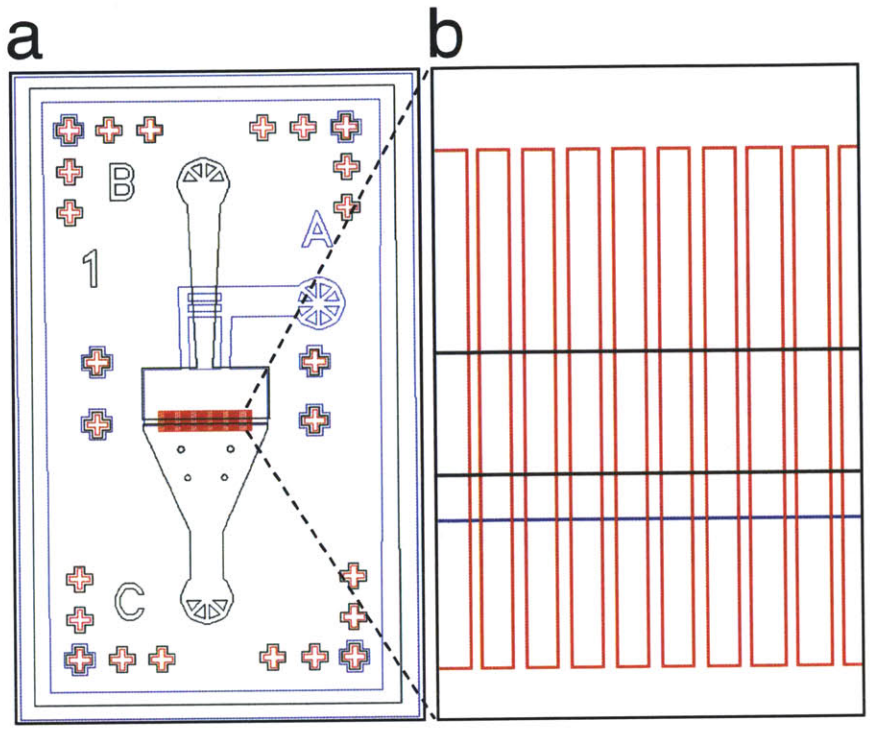

Figure B-3: Layout showing the masks used to fabricate the compression and flow layers of the chip. (a) Mask **compress-1** (blue) is for the 65 µm thin **compression layer**. Mask **flow-2** (green) is for the 100 µm thick region of the **flow layer** where the animals flow. Mask **flow-1** (red) is for the 10 µm thin region comprising the **channel array** within the **flow layer**. (b) Expanded view of the mask regions showing the overlap of Mask **flow-1** and Mask **flow-2** to form the **channel array**.

during the photoresist development step). The positive mask should be dark (opaque) in the areas where the photoresist will remain on the wafer surface forming the mold.

Both negative and posititive photoresists will be used to form structures with square edges (**flow-1**) and rounded edges (**flow-2**), respectively, on the same wafer mold. Negative resist retains the square edges during the reflow process while the positive resist becomes rounded. The **flow-2** photoresist layer (comprising the regions of the flow layer where *C. elegans* is transported) is too thick to be reliably coated in a single step using SIPR-7123 photoresist. To create this thick layer (Steps 18-22), two separate layers of 50 µm will be spin-coated to achieve the desired thickness of 100 µm. Reflowing the positive **flow-2** photoresist layer improves the immobilization stability achieved by these devices. Additionally, rounded channels allow incorporation of microfluidic valves [148] to integrate fluidic control directly into the device [79, 87], as in Chapters 2-4.

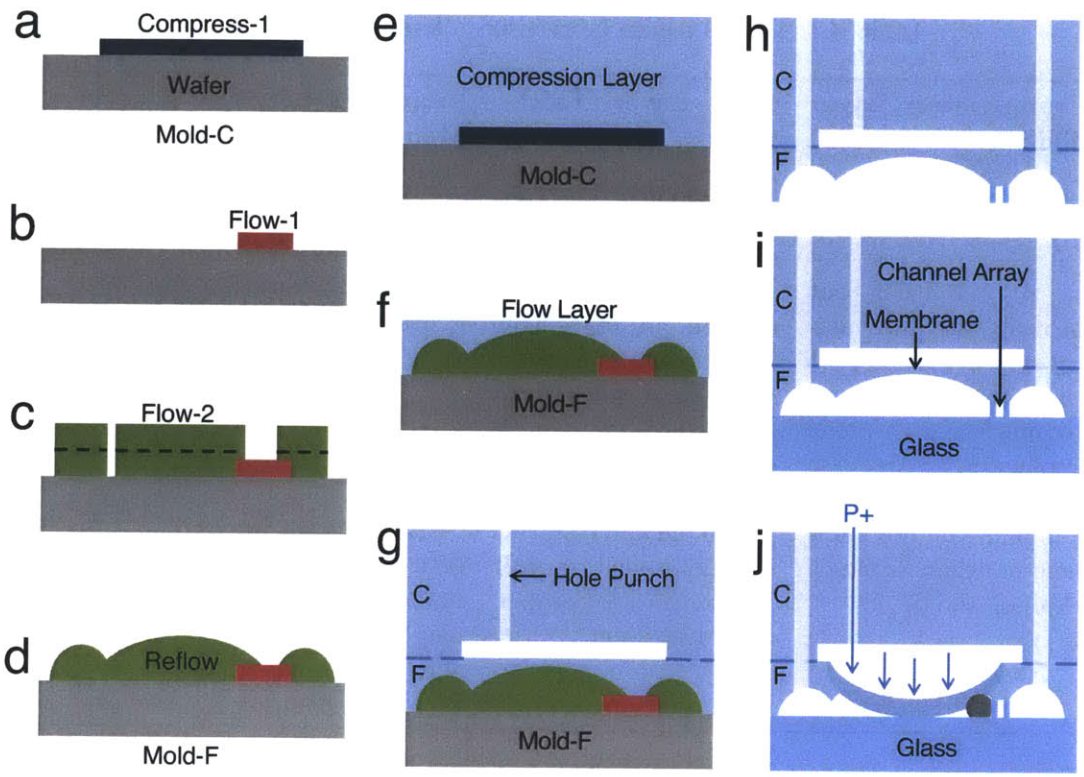

Figure B-4: Fabrication of photoresist molds and PDMS layers. The patterning of **mold-C** (a) and **mold-F** (b-d). Molding (e-f) and bonding (g) of the PDMS layers. Bonding of the released PDMS layer to glass (h-i). Actuation of the **immobilization membrane** when pressurized (j). These illustrations are referenced throughout the fabrication procedure.

The masks for photolithography can be ordered from various companies including Fineline Imaging (Colorado Springs, CO, USA), Micro Lithography Services Ltd (UK), and Advanced Reproductions (Andover, MA, USA). To place a mask order, send the company the AutoCAD file containing the mask patterns. Specify in your order whether each mask is negative or positive.

Once the PDMS layers are molded, they will be thermally bonded together since plasma bonding forms a less reliable bond. This is due to the variability of the plasma treatment process (unless automated) and high sensitivity to particulates and surface defects. Additionally, alignment of PDMS layers is critical for the compression layer to function properly. Prior to thermal bonding the PDMS layers are pressed together and can be aligned multiple times under a stereo microscope to achieve perfect alignment before the layers are baked to thermally bond them together. Such alignment is more challenging using the plasma

Table B.1: PDMS device fabrication tolerances of Figure B-4.

Compression Layer Thickness	**Flow Layer Thickness**	**Immobilization Membrane Thickness**
~6 mm thickness	~120 µm	~15-20 µm
< 6 mm will not provide the mechanical stability to support the steel pins inserted to interface with tygon tubing.	< 120 µm will result in an extremely thin membrane structure that will likely tear apart or stretch during fabrication.	< 15 µm will cause fabrication failure.
> 6 mm, will not allow hole-puncher to punch through the device	> 120 µm will result in a membrane that will be too thick for proper immobilization.	> 20 µm will require high pressures for immobilization which may injure the animals and/or delaminate the PDMS layers.

bonding technique.

We recommend the following design rules for scaling down the chip to accommodate animals in the L1-L3 larval stages:

1. The **flow-1 layer** thickness and spacing in the channel array should be scaled to 1/5 of the animal width.

2. The **flow-2 layer** thickness should be scaled to 1/2 the animal width.

3. The thin PDMS layer spin-coated on **mold-F** should be scaled such that the **immobilization membrane** thickness remains the same for robustness and fabrication reliability.

4. The **compress-1 layer** thickness should remain the same.

5. The thick PDMS layer formed on **mold-C** should remain the same thickness to provide rigidity to support interfacing with steel pins and tubing.

For those looking for more information on soft lithography techniques, a recent protocol by Qin *et al.* [13] also gives a general overview. However, unlike the protocol presented here,

Qin *et al.* does not discuss fabrication of devices with multiple PDMS layers.

B.2 Materials

B.2.1 Reagents

- Experimental animals (*C. elegans*)[1]. The cellular process to be visualized should be labeled with a fluorescent dye or reporter protein for imaging. The animals can be cultured on and transferred from either agar plates or liquid [145]. For imaging mechanosensory neurons for femtosecond laser microsurgery, the SK4005 strain (which expresses GFP in the touch neurons) can be used.

- *C. elegans* M9 buffer solution [145]

B.2.2 Equipment

General equipment

- Inverted fluorescence microscope (1) (Nikon Eclipse TI or similar model) including a stage plate capable of holding a standard 50 mm dish with cover glass bottom

- Image acquisition software (1) (NIS-Elements 2.0) and compatible computer

- High resolution CCD camera (1) (Photometrics Coolsnap HQ2)

- Powder-free gloves (VWR)

- Microscope ruler (1) (Ted Pella Inc., Cat. No. 6085)

Master Mold Fabrication

- Silicon wafers (2) with 4" diameter (University Wafer Corp.)

- Photomasks. The procedure for ordering a photomask is detailed in the Experimental Design section

[1] **Caution:** All animal experiments must comply with the relevant institutional and national animal care guidelines.

- Alignment and UV exposure tool[2]. This is expensive equipment and is typically shared by multiple laboratories at the microfabrication facilities available at most universities. (Lamp power rating 200 mW/cm^2). UV exposure time is dependent upon source intensity. Adjust exposure time to accommodate differences in source intensity if not using the recommended source.
- Spinner with vacuum chuck (1) (Headway Research Corp.)
- Negative Photoresist[3] SU-8 2075 (Microchem Corp.)
- Negative Photoresist SU-8 2025 (Microchem Corp.)
- Negative photoresist developer, PM acetate (propylene glycol monomethyl ether acetate) (Eastman)
- Isopropyl alcohol (IPA) (VWR, Cat. No. BDH1133-1LP)
- Positive Photoresist SPIR-7123 (Micro-Si Corp.)
- Positive photoresist developer AZ440 (AZ Photoresists Group of Hoechst Celanese Corp.)
- HMDS (Hexamethyldisilazane)[4] (SPI-Chem Corp.)
- F13-TCS (Tridecafluoro-1,1,2,2-Tetrahydrooctyl)-1-Trichlorosilane[5] (United Chemical Technologies, Cat. No. T2492-KG)
- Hotplates set to 65 °C, 95 °C and 140 °C with temperature ramp capability (2) (PMC, Cat. No. Dataplate 730)
- Petri dish (4) 150 x 15 mm (Falcon, Cat. No. 35-1058)
- Glass Pasteur pipette and rubber bulb (1) (VWR, Cat. Nos.14673-010, 56310-002)
- Cotton Swabs (VWR, Cat. No. 10806-005)
- Eyedropper bulb, 5 ml (2) (VWR, Cat. No. 56335-022)

[2]**Caution:** Use protective eyewear for UV light.
[3]**Caution:** Photoresists and developers are toxic chemicals. Proper protective equipment should be worn according to the institutional regulations.
[4]**Caution:** HMDS is toxic, corrosive, and highly flammable.
[5]**Caution:** F13-TCS is toxic and corrosive.

PDMS Device Fabrication

- PDMS RTV615A base, RTV615B curing agent (GE Silicones)
- Vacuum desiccator (2) 230 mm (Bel-Art, Cat. No. 420250000) connected to a vacuum line
- Chemical fume hood
- Oven set to 80 °C (1) (Yamato, Cat. No. DX-400)
- PDMS mixer/degasser machine (1) (Thinky Corp., Cat. No. ARE-250) (*optional*)
- Plastic mixing cups (2) (Thinky Corp., match to ARE-250 mixer) (*optional*)
- Hole-punchers with 0.75 mm (1) and 0.5 mm (1) diameters and cutting mat (1) (Ted Pella Inc., Cat. Nos. 15071, 15072, 15097)
- Plasma chamber (1) (Harrick, Cat. No. PDC-001) and its vacuum pump (Leybold vacuum products inc., Cat. No. Trivac D2.5E)
- Clear adhesive tape (2) (Scotch brand, 3M)
- Glass slide (1) 75 × 50 × 1 mm (Fisher Scientific, Cat. No. 12-550C)
- Aluminum foil (Reynolds Wrap)
- Lint-free fabrication wipes (VWR, Cat. No. HP-9310-4828)
- Laboratory scale (1) (Ohaus, Cat. No. sp202)
- Dish with cover glass bottom, 50 mm OD × 7 mm High, Glass Area: 40 mm diameter (Ted Pella Inc., Cat. No. 14026-20) or (Electron Microscopy Sciences, Cat. No. 70674-52)

Off-chip system

- Tygon Tubing (VWR, 1/16" ID × 1/8" OD × 50 ft length)
- Pressure Gauge (1) 1/8" NPT 30" (Noshok, Cat. No. 15-100)
- Pressure regulator (1) (Minuteman Controls, Cat. No. R-800-300-W/K)

- Right-angle threaded tee (1), nylon, 1/8" NPT(F) × 1/8" NPT(F) × 1/8" NPT(M) (Cole Parmer, Cat. No. C-06349-20)
- Female luer to 1/8" NPT (2) (Cole Parmer, Cat. No. C-31200-60)
- Male luer to 200 series barb (3) (Value Plastics, Cat. No. MTLL230-1)
- Male luer plug (3) (Value Plastics, Cat. No. LP4-1)
- Dispensing-needle-tips (3) (McMaster-Carr Corp., 23 gauge, 0.5" long, type 304, ID 0.017", OD 0.025")
- Tygon tubing (VWR, 0.02" ID, 0.06" OD, 50 ft, 0.02" wall)
- Steel pins for chip-to-tube interface (New England Small Tube Corp., 0.025" OD × 0.017" ID, 0.500" length, s/s tube, type 304, cut, deburred, passivated)
- Manual 3-way valve (1): Stopcock with 2 female luer connections and male lock (Cole Parmer, Cat. No. C-30600-02)
- Syringe (1) 3 ml luer-lok tip (BD, Cat. No. REF 309585)
- Teflon thread tape, 1.3 cm × 7.6 m (VWR, Cat. No. 60490-100)

Microscope Optics (suggested)

- High numerical aperture (NA) objective lens (1) for high-resolution imaging and laser microsurgery. NA greater than 0.7 recommended. Example: Mag: 20×, NA: 0.75, air lens (Nikon, Cat. No. MRD00200)
- Fluorescence filter cube for use with the fluorescent reporter protein expressed by the organism (1) (For GFP, Nikon, HQ:F)
- Optical notch filter at the laser wavelength (1) (Thorlabs, Cat. No. FES0700)
- Standard square cage plate, SM1 threaded inner bore (1) (Thorlabs, Cat. No. CP02)
- Epi and brightfield shutters (1) (Sutter, Cat. Nos. LB-SC and IQ25-SA)

B.3 Procedure

B.3.1 Fabrication of the molds.

Timing: These steps are time dependent and should be completed within 4 hours followed by baking overnight to reflow the positive photoresist.

Fabrication of mold-C for the compress-1 layer with 65 µm thickness (Figure B-4a)

1. Dehydrate a silicon wafer by placing it on the hotplate at 135 °C for 10 min. Allow the wafer to cool for 2 min before proceeding to next step.

2. Center the wafer on the spinner chuck and apply vacuum. Spin wafer at 1000 rpm and place 2 ml of HMDS onto the spinning water using an eyedropper bulb and continue spinning for 10 s.

3. Coat a 65 µm layer of SU-8 2075 negative photoresist onto the wafer (Figure B-4a). Center the wafer on the spinner chuck, and turn on the spinner-chuck vacuum to hold the wafer. Pour sufficient photoresist onto the wafer to cover a 5 cm circle. Turn on the spinner at 500 rpm for 5 s, ramp the spin rate from 500 to 3500 rpm in 5 s, and then spin for 30 s at 3500 rpm.

4. Place aluminum foil on top of the hotplate. Bake the wafer for 3 min at 65 °C followed by 8 min at 95 °C to make the photoresist more rigid for mask alignment and UV exposure.

5. Edge bead removal[6]: Center the wafer on the spinner chuck and apply vacuum. Dip cotton-tipped swab into PM acetate (developer) and apply gently but firmly to the edge of wafer while spinning at 50 rpm to remove the excess material from the edge of wafer.

6. UV light exposure: Load the **compress-1 mask** into the mask aligner, and place the wafer on the base of alignment tool. Position the **compress-1 mask** on the wafer to pattern the negative photoresist. Ensure that the mask is flat against the photoresist.

[6] **Caution:** If the edges are raised due to the edge bead, the mask will not make proper contact with the photoresist resulting in a misaligned pattern.

Remove UV block. Expose to UV light for 40 s[7] when using the recommended 200 mW/cm^2 source. Reinsert UV block.

7. Bake the wafer on the hotplates for 1.5 min at 65 °C followed by 6.5 min at 95 °C. Allow the wafer to cool for 5 min.

8. Center the wafer on the spinner chuck and apply vacuum. Develop the negative photoresist by applying PM acetate onto the spinning wafer using an eyedropper at 500 rpm, followed by rinsing with IPA at 1000 rpm, and drying with nitrogen air gun. Ensure that the pattern is fully developed.

9. Cover the wafer with a petri dish or place in wafer carrier to protect from dust.

Fabrication of mold-F for the flow layer (see Figure B-4b-d) containing two layers fabricated sequentially (flow-1 and flow-2)

10. Repeat Steps 1 and 2 to pre-treat a new wafer.

11. Coat a 10 µm thick layer of SU-8 2025 negative photoresist onto the wafer. Center the wafer on the chuck and turn on the vacuum. Set the spinner to start at 500 rpm. Pour[8] sufficient photoresist onto the wafer to cover a 5 cm circle. Turn on the spinner at 500 rpm for 5 s, ramp from 500 to 4000 rpm in 5 sec, then allow wafer to spin for 30 s at 4000 rpm.

12. Bake the wafer on the hotplates for 1 min at 65 °C followed by 5 min at 95 °C to make the photoresist more rigid for mask alignment during UV exposure.

13. Remove the edge bead as in Step 5.

14. UV exposure: Load the **flow-1 mask** (red) into the mask aligner and place the wafer on the base of the alignment tool. Position the **flow-1 mask** on the wafer to pattern the negative resist. Ensure that the mask is flat against the photoresist. Remove

[7]**Critical step:** UV exposure time is dependent upon source intensity. Adjust exposure time to accommodate differences in source intensity if not using the recommended source.

[8]**Critical step:** Remain close to the surface while pouring the photoresist to prevent bubbles from forming that may result in fabrication failure.

UV block. Expose to UV light for 40 s[9] when using the recommended 200 mW/cm^2 source. Reinsert UV block.

15. Bake the wafer on the hotplates for 1 min at 65 °C followed by 5 min at 95 °C.

16. Develop the negative photoresist with PM acetate as in Step 8.

17. Bake the wafer at 140 °C for 10 min. Allow the wafer to cool for 5 min before proceeding to the next step[10].

18. Center the wafer on the spinner chuck and apply vacuum. Coat the first 50 µm thick layer onto the wafer: Center the wafer on the spinner chuck and set speed to 600 rpm. Pour sufficient positive photoresist (SIPR-7123) onto the wafer to cover a 5 cm circle. Spin at 600 rpm for 100 s[11].

19. Bake the wafer on the hotplates while ramping the temperature[12] from 40 °C to 100 °C at a rate of 36 °C/hr (10 min).

20. Bake the wafer on a hotplate at 140 °C for 10 min[13].

21. Center the wafer on the spinner chuck and apply vacuum. Remove the edge bead with IPA while using the same method as in Step 5.

22. By repeating Steps 18 through 21, coat an additional 50 µm thick layer of photoresist onto the wafer to achieve a total of 100 µm thick coating.[14]

23. UV light exposure: Load the **flow-2 mask** (green) into the mask aligner and place the wafer on the base of the alignment tool. Position the **flow-2 mask** on the wafer.

---

[9]**Critical step:** UV exposure time is dependent upon source intensity. Adjust exposure time to accommodate differences in source intensity if not using the recommended source.

[10]**Critical step:** If the wafer is not cooled before proceeding to the next step, bubbles will form in the photoresist causing fabrication failure.

[11]**Critical step:** The **flow-2** photoresist layer (comprising the regions of the **flow layer** where *C. elegans* is transported) is too thick to be coated in a single step. This is the first of two separate layers of 50 µm that will be spin-coated to achieve the desired thickness of 100 µm.

[12]**Critical step:** The temperature ramping is key to ensure thorough and even hardening of the thick layer.

[13]**Critical step:** Allow the wafer to cool for 10 min before proceeding to the next step. If wafer and photoresist are not cooled before proceeding to the next step, air bubbles will form due to the heat in the newly poured photoresist, causing fabrication failure.

[14]**Critical step:** The **flow-2** photoresist layer (comprising the regions of the flow layer where *C. elegans* is transported) is too thick to be coated in a single step. This is the second of two separate layers of 50 µm that will be spin-coated to achieve the desired thickness of 100 µm.

Ensure that the photoresist pattern of **flow-1 layer** on the wafer is properly aligned with the **flow-2 mask** using the fiducial crosses. Ensure that the mask is flat against the photoresist. Remove UV block. Expose to UV light for 4.5 min[15] when using the recommended 200 mW/cm^2 source. Reinsert UV block.

24. Develop the positive photoresist[16]: Place in beaker with AZ440 developer for 30 min. Swirl the beaker gently to allow fresh developer to reach the photoresist.

25. Reflow[17] the **flow-2 layer** by ramping the temperature from 20 °C to 150 °C at rate of 10 °C / h using a hotplate. This process can take place overnight.? TROUBLESHOOTING.

B.3.2 Fabrication of the PDMS devices.

Timing: These steps are time dependent due to the critical and sensitive thermal bonding of PDMS layers. A batch of devices can be made within 2 h followed curing overnight.

Cleaning and pre-treatment of mold-C and mold-F

26. Use dry nitrogen gun to remove any dust particles from **mold-C** and **mold-F** (Figure B-5a). Place wafers in petri dishes to protect them from dust particles when not in use.? TROUBLESHOOTING.

27. Place wafer in vacuum desiccators beside a folded aluminum foil reservoir with a 5 cm diameter and 1.5 cm raised edges. Put two drops of F13-TCS ((Tridecafluoro-1,1,2,2-Tetrahydrooctyl)-1-Trichlorosilane)[18,19] on the aluminum foil using a glass Pasteur pipette with a rubber bulb. Remove the rubber bulb from the pipette and leave the pipette in the desiccator. Close the desiccator and turn on vacuum for 3 min.

[15]**Critical step:** UV exposure time is dependent upon source intensity. Adjust exposure time to accommodate differences in source intensity if not using the recommended source.

[16]**Critical step:** If the photoresist is overdeveloped, features will not have the correct dimensions. This will result in immobilization failure. See Figure B-6a showing the device cross-section.

[17]**Critical step:** The reflow process rounds the edges of the photoresist (Figure B-4d) and results in proper roundness of the **immobilization membrane**, which is necessary for stable immobilization.

[18]**Critical step:** F13-TCS is used on the newly fabricated molds and can be used at least 20 times before this F13-TCS coating step should be repeated.

[19]**Caution:** F13-TCS is toxic and corrosive. This step should be done with the desiccator placed inside a chemical hood. Use a separate desiccator in later PDMS fabrication steps to avoid cross contamination. Latex gloves should be worn when dispensing F13-TCS and discarded after use.

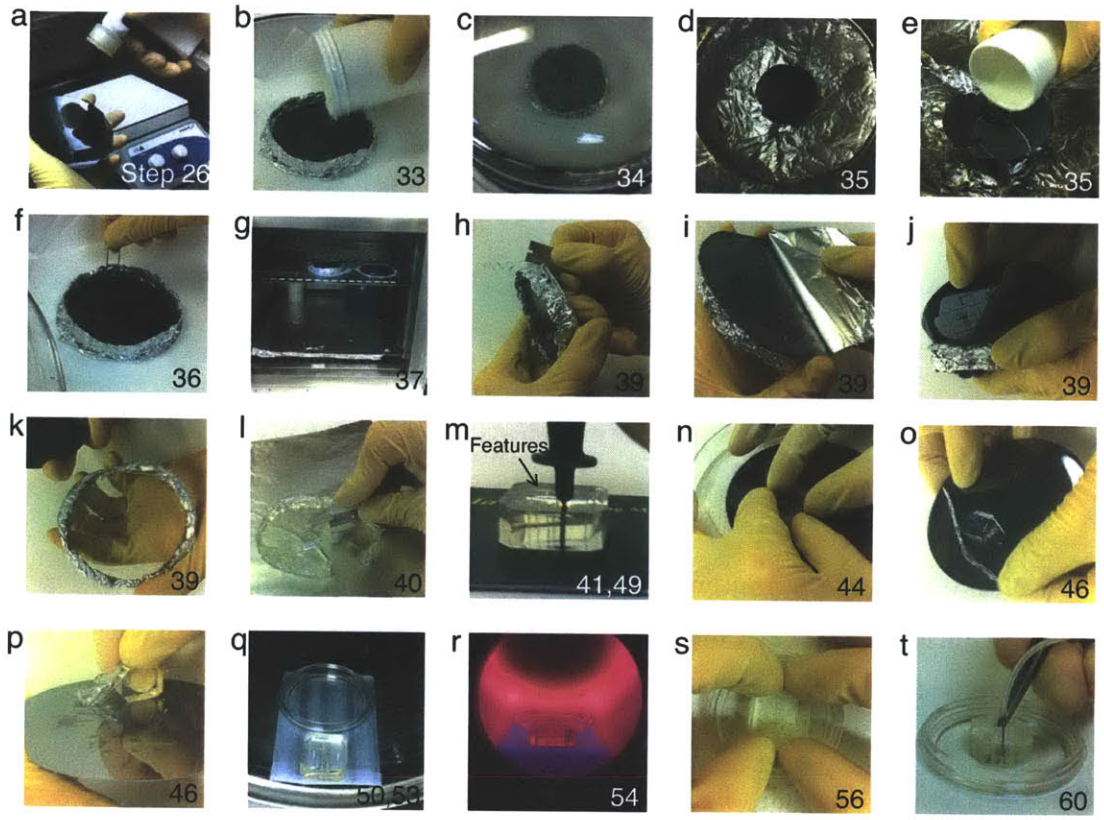

Figure B-5: Images of PDMS fabrication, hole-punching, plasma bonding, and interfacing with steel pins and tubing as detailed in Steps 26-60. The corresponding step is labeled in each image.

Figure B-6: Cross-section of the microfluidic device showing the immobilization region. The device is vertically cut along the line from **port-B** to **port-C**. The thermally bonded **compression layer** and **flow layer** are visible. The PDMS **channel array** is molded from the **flow-1 layer** with 10 µm thickness. A 15-20 µm thin PDMS membrane is formed between the **compress-1** and **flow-2** layers. This device would later be plasma bonded to a cover glass. The fabrication tolerances are listed in Table B.1. Scale bar: 50 µm.

Molding of the PDMS layers (see Figure B-4e-h and B-5b-m)

28. Prepare 5:1 ratio PDMS by combining 50 g of RTV615A base with 10 g of RTV615B curing agent into a **mixing cup** labeled "**C**" indicating that the PDMS is for constructing the **compression layer**.

29. Prepare 20:1 ratio PDMS by combining 15 g of RTV615A base with 0.75 g of RTV615B curing agent into a **mixing cup** labeled "**F**" indicating that the PDMS is for constructing the **flow layer**.

30. Mix the contents of the **mixing cup-C** using the recommended mixer/degasser machine (Thinky Corp. Cat. No. ARE-250) or by stirring manually as a more cost-effective method.

    (a) Weigh the **mixing cup-C** and holder. Place **mixing cup-C** in mixer/degasser machine (Thinky Corp. Cat. No. ARE-250) and set for 2 min of mixing followed by 3 min of degassing at 2000 rpm (or 400 G) at room temperature (20 - 25 C). Set the weight counterbalance and start mixer.

    (b) Stir the contents of **mixing cup-C** using a plastic stirring stick for 3 min while scraping the sides of the container to ensure all contents are integrated. Degas **mixing cup-C** for 60 min in a vacuum desiccator and remove any bubbles using a paper clip.

31. Repeat the Step 30 to mix and degas **mixing cup-F**.

32. Wrap the bottom of the **mold-C** with aluminum foil, sealing firmly around the edges of the wafer with the foil. Curl up the remaining foil providing a 1 cm high reservoir for pouring PDMS onto the wafer (Figure B-5b).

33. Pour the contents of **mixing cup-C** onto **mold-C** (Figure B-3e and B-5b). Ensure that the mixing cup is close to the wafer surface to prevent unwanted bubbles from being trapped in the poured PDMS (Figure B-5b).

34. Place **mold-C** in the desiccator for 10 min under vacuum to remove air from PDMS (Figure B-5c).

35. Coating of 120 µm layer (Figure B-3f) of 20:1 ratio PDMS onto **mold-F**: Center **mold-F** on the vacuum chuck, turn on the spinner-chuck vacuum, and set spin speed

to 710 rpm (Figure B-5d). Pour[20] the contents of **mixing cup-F** onto the center of **mold-F** in a 5 cm circle (Figure B-5e). Spin for 60 s.

36. Remove bubbles from the PDMS on **mold-C**. Carefully vent the desiccator and remove the lid. Use a paperclip to move the remaining bubbles on the surface of the PDMS to the edge of the wafer. Ensure that there are no bubbles on the wafer surface (Figure B-5f).? TROUBLESHOOTING.

37. Bake both **mold-C** (Figure B-4e) and **mold-F** (Figure B-4f) in an oven for 30 min at 80 °C to provide rigidity to the PDMS layers (Figure B-5g).

Thermal Bonding of PDMS compression and flow layers: (see Figure B-4e-h and B-5b-m)

38. Remove **mold-C** (Figure B-4e) and **mold-F** (Figure B-4f) from the 80 °C oven and allow both to cool for 10 min. Touch the PDMS surface of each wafer at the edge to verify that the surface is relatively sticky for adhesion and not completely rigid from over-curing to enable strong thermal bond.? TROUBLESHOOTING.

39. Use a razor blade to trim the foil from the edge of **mold-C** (Figure B-5 h) and peel the foil from the backside of the wafer (Figure B-5i). Carefully and slowly peel the PDMS layer from the wafer surface[21] (Figure B-5j-k) and place it on a piece of clean foil with molded side down.

40. Use the razor blade to cut out the device components from the PDMS **compression layer**. Cut around the outermost box surrounding each device (Figure B-5l).

41. Place device components cut from **compression layer** on the **hole-punching mat** with the molded feature side of PDMS facing up. Use scotch tape to remove any debris that may be on the PDMS surface. Punch the access point (labeled "**A**" in Figure B-3a) to the compression layer starting from the molded side using the 0.5 mm **hole-puncher**. Ensure that the **hole-puncher** is sharp and free of debris. Press firmly and punch through the PDMS until contacting the mat (Figure B-5m). Then

[20]**CRITICAL STEP**: Avoid introducing bubbles by keeping the mixing cup close to the wafer surface while pouring.

[21]**Critical step:** Avoid touching the molded surface of the layer by handling only from the sides of the layer since any residue from gloves can interfere with thermal bonding in subsequent steps.

lift up the device and depress the plunger to eject the PDMS. Repeat for each device.? TROUBLESHOOTING.

42. Inspect each device component thoroughly under stereo microscope. Press tape firmly on the molded side of PDMS to remove any debris that can result in device failure (Figure B-10b).? TROUBLESHOOTING.

43. Clean the top surface of PDMS layer on **mold-F** using scotch tape. Ensure that the device is free of residues from accidental finger prints.

44. Using a stereo microscope, align the PDMS device components from **compression layer** over the PDMS device components in **flow layer**. Ensure that the molded side of the **compression layer** is aligned to the fiducial crosses (Figure B-3). Press firmly on top to remove any air bubbles trapped between the two layers (Figure B-4g and B-5n).

45. Bake the combined compression and flow layers by placing them in the 80 °C oven overnight to achieve thermal bond (Figure B-4g).

46. Gently peel the combined PDMS layers from the wafer surface (Figure B-4h). Begin by rolling the edge of the thin **flow layer** (Figure B-5o) to the base of the thick **compression layer** and lift up both layers up together[22] (Figure B-5p). Use a razor blade to trim the edges around the combined PDMS layers (Figure B-5q).

    (a) If this is the first time that the molds were used to fabricate a PDMS device, proceed to Step 47 (PDMS device characterization) in order to ensure that the molds are properly fabricated.

    (b) If the mold fabrication has already been characterized, proceed to Step 49.

B.3.3 Characterization of the PDMS device fabrication

TIMING: These steps are not time dependent and should take about 20 min to complete.

47. Cut a cross-section of the PDMS device vertically along **port-B** and **port-C** using a razor blade (as in the cross-section shown in Figure B-4h). Place the cross-section onto a microscope slide to measure the thickness of each layer (Figure B-6).

[22]**Critical step:** The thin PDMS layer may stretch or tear if it is not lifted at the same time with the thick layer.

48. Record an image of the cross section. Measure the dimensions of each layer and membrane thicknesses with the aid of a standard microscope ruler (Figure B-6).

B.3.4 Hole-punching and plasma bonding of the device to cover glass

TIMING: These steps are not time dependent and should take about 20 min to complete followed by baking overnight.

49. Punch two **holes** (labeled "**B**" and "**C**" in Figure B-3a) to create **port-B** and **port-C** (Figure B-3a) for off-chip access to the **flow layer** as in Step 41, but using the 0.75 mm **hole-puncher** rather than the 0.5 mm **hole-puncher** used in Step 41 (Figure B-5m).

50. Wrap a double-width glass slide (1 mm × 50 mm × 75 mm) with transparent adhesive tape to form a support base[23] (Figure B-5q).

51. Place lint-free fab wipes on the table to provide a padded surface (Figure B-5s).[24]

52. Inspect the PDMS device and the dish (with cover glass bottom) for particles and use clear adhesive tape to remove debris.

53. Place the PDMS device and the dish (with cover glass bottom) onto the support base (created in Step 50) inside the plasma chamber[25] with the molded side of the **flow layer** facing up and the raised edge of the cover glass dish also facing up (Figure B-5q).

54. Turn on the vacuum for 2 min. Turn on the **plasma source** and slightly lower the vacuum in the plasma chamber until the purple glow in the chamber turns light pink in color (Figure B-5r) and continue plasma exposure for 1 min.

55. Turn off the **plasma source** followed by the **vacuum pump**. Gently vent the chamber to release the vacuum and avoid disturbing the items in the chamber. Remove the treated samples from the chamber using the support base without touching the treated surfaces that are to be bonded together.

---

[23] **Critical step:** This tape will also protect the surface of these glass slides from plasma treatment in Steps 53-55, and prevent the PDMS device or dish from bonding to them. Ensure that the glass surface is completely covered with tape.

[24] **Critical step:** This padded surface will protect the delicate cover glass bottom of the dish during the bonding process in Step 56 and when inserting steel pins in Step 60.

[25] **Critical step:** The dish and PDMS device should not be in contact with each other inside the plasma chamber.

56. Place the dish with cover glass bottom (with the raised edge facing up) on top of the fab wipes (from Step 51) to provide cushioning. Immediately place the device with the molded side of the **flow layer** facing down and center it on the dish. Press firmly but gently on the device to remove air bubbles but avoid cracking the cover glass (Figure B-5s). Continue pressing for 20 s to ensure good contact between the PDMS **channel array** and cover glass.

57. Inspect the completed device (Figure B-4i) under a stereo microscope to ensure that the device is bonded to the cover glass with no air bubbles trapped between the PDMS layers. Air bubbles may disrupt the fluidic channels or the **channel array** (Figure B-7).? TROUBLESHOOTING.

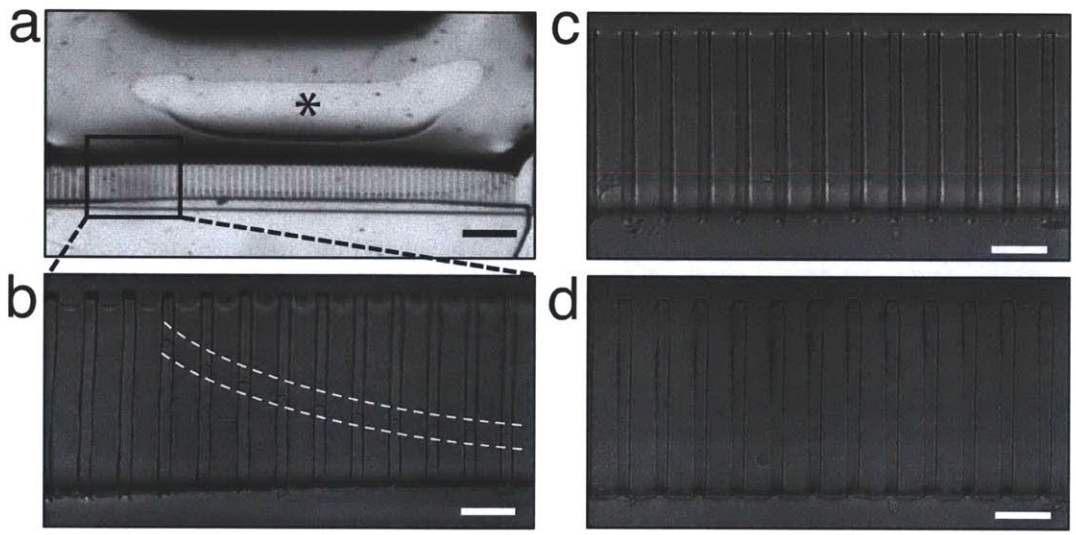

Figure B-7: Comparison of failed and successful fabrication of **channel array**. (a) The **immobilization membrane** is too thin and has collapsed/sagged (*). The membrane has bonded either to the cover glass below during plasma bonding or to the **compression layer** above during thermal bonding. The boxed region shows the pillars of the **channel array** that did not plasma bond properly to the glass. Scale bar is 100 µm. (b) Magnified image of the boxed area in (a) that shows the region (between the dashed white lines) where the pillars did not properly bond to the cover glass. (c) Proper bonding when the **immobilization membrane** not pressurized. (d) Proper bonding when pressurized. Scale bar: 25 µm.

58. Bake the device in the 80 °C oven for 24 h to complete thermal bonding.

B.3.5 Assembly and connection of off-chip components (Figure B-8)

TIMING: These steps are not time dependent and should take about 20 min to complete.

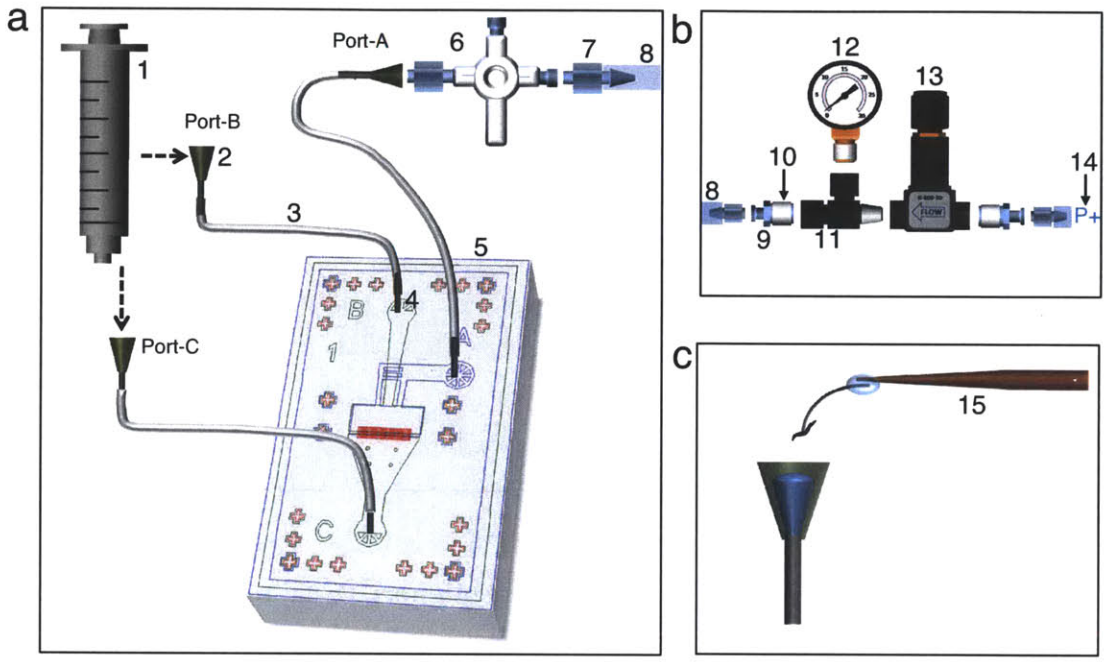

Figure B-8: Microfluidic device integrated with off-chip components. (a) Components for manual chip operation include the syringe (attached to **port-B** for loading the animal or **port-C** for unloading the animal) and manual **valve-A** (attached to **port-A** for pressurizing the **compression layer**). The large plastic tubing is labeled '8' in both (a) and (b) showing the connection between panels. (b) Construction of the air pressure regulator and gauge using connectors and Teflon thread tape. The 'flow arrow' indicates the direction of the flow from the pressure source to the chip. (c) Placement of an animal in the M9 buffer of the dispensing-needle-tip of **port-A** using an eyelash glued to a toothpick. The numerically labeled components are listed in Table B.2.

59. Assemble the **pressure gauge** and **regulator** (Figure B-8b). Use Teflon thread tape to ensure an air-tight seal around screw connections. Connect the tubing from the regulator to the air pressure supply.

60. Insert a **dispensing-needle-tip** into a 15 cm piece of tygon tubing and insert a steel pin into the opposite end of the tygon. Gently insert the steel pin into the PDMS hole to access **port-A** (Figure B-5t and B-8a). Avoid tearing the PDMS to prevent

Table B.2: List of components for the microfluidic system in Figure B-8

Component	Description
1	Syringe
2	Dispensing-needle-tip, 23 gauge
3	Tygon tubing
4	Steel pin
5	Microfluidic device
6	Manual 3-way valve: Stopcock with luer connections
7	Male luer lock to barb connector
8	Large flexible plastic tubing
9	Screw to female luer lock connector
10	Teflon thread tape
11	Right-angle threaded tee
12	Pressure gauge
13	Pressure regulator
14	Pressure source
15	Toothpick with glued eyelash

creation of unwanted particles. Repeat for both **port-B** and **port-C**.[26]

61. Connect one of the 3-way manual **valve-A** ports to the pressurized air from the regulator and the gauge (Figure B-8a). Leave one of the ports open to atmospheric pressure. Connect one of the ports to the dispensing-needle-tip (which should be connected to **port-A** via tygon tubing). Ensure that the arrow on the regulator is pointing towards the manual **valve-A** directing flow into the chip.

B.3.6 Manual operation (Figure B-9)

TIMING: These steps are not time dependent and should take about 20 min for initial priming and optimization of the immobilization pressure. Once in place the system can immobilize animals at a rate of 1 min per animal.

Prime the device to remove air bubbles before operation

62. Disconnect the tubing and steel pin from device **port-A**. Completely fill the 15 cm long inlet tube with deionized water (using a syringe) and reconnect the tube to the device

[26] **Critical step:** The dish should be placed on a flat surface padded with lint-free fab wipes when inserting the steel pins to avoid cracking the delicate cover glass.

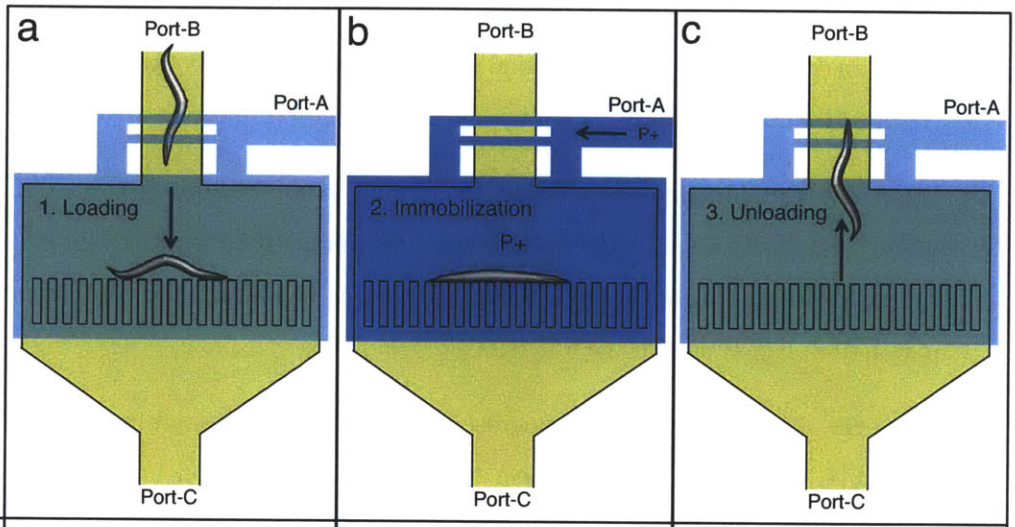

Port-A	Valve is in OFF position	Valve is in ON position, applying 15-20 psi	Valve is in OFF position
Port-B	Low pressure applied by syringe to position nematode	Syringe is detached	Syringe is detached. Nematode is dispensed onto agar pad
Port-C	Syringe is detached	Syringe is detached	Low pressure applied by syringe

Figure B-9: Manual operation of the microfluidic device. The table indicates the state of each port during operation. (a) Loading of the animal from syringe as in Step 65. (b) Immobilization of the animal in linear orientation as in Step 66. (c) Unloading of the animal to agar plate as in Step 68.

port-A. Set the pressure regulator to ~3 psi. Turn on the manual **valve-A** connected to **port-A** to pressurize the layer with low pressure. Slowly increase the pressure regulator to ~15 psi and wait 10-15 min for the air bubbles to permeate into the surrounding PDMS to fill the **compression layer** with water. Turn the **valve-A** such that the input to **port-A** is set to atmospheric pressure. ? TROUBLESHOOTING.

63. Aspirate M9 buffer solution into the syringe. Fill the **flow layer** using low pressure from the M9-filled syringe attached to **port-B** by gently removing any trapped bubbles.

64. Use a worm pick to transfer a single animal from either liquid or an agar plate into a small volume of M9 in the dispensing-needle-tip connected to **port-B** (Figure B-8c). Hold the M9 filled syringe with tip facing downward and connect it to the dispensing-needle-tip of **port-B** (Figure B-8a). Gently flick the syringe to remove any air bubbles that may be trapped.

65. Pressurize the syringe connected to **port-B** to gently flow liquid through the **channel array** in order to position the animal in a linear orientation along the **channel array** (Figure B-9a). ? TROUBLESHOOTING.

66. Pressurize the **compression layer** by turning manual **valve-A** to the pressurized source (Figure B-8b and B-9b). Optimize the immobilization pressure by adjusting the pressure regulator to account for differences in animal size and/or fabrication parameters.? TROUBLESHOOTING.

67. Place the chip on the inverted microscope. Perform the desired imaging and optical manipulations such as fluorescence, confocal and two-photon imaging, laser micro-surgery, calcium imaging, or photo-stimulation.

68. Remove the dispensing-needle-tip of **port-B** from the tygon tubing and direct the end of tubing onto an agar pad or reservoir to dispense the animal. Turn **valve-A** to atmospheric pressure in order to release the pressure in the **compression layer**. Attach the syringe to the dispensing-needle-tip of **port-C**. Gently pressurize the syringe in **port-C** to flow the animal out of the device through **port-B**. Replace the dispensing-needle-tip to the tygon tubing in **port-A** (Figure B-9c). ? TROUBLESHOOTING.

69. Repeat Steps 65 through 68 to immobilize additional animals.

70. To store the device, flush the microfluidic channels with deionized water and place male luer caps on each of the three dispensing-needle-tips. Cover the device with petri-dish to avoid dust particles.

B.4 Timing

The timing of the steps for fabrication and assembly of the microfluidic devices described in this chapter are shown in Table B.3.

B.5 Troubleshooting

Troubleshooting advice is provided in Table B.4.

Table B.3: Time required for fabrication and assembly of microfluidic devices.

Steps	Description	Time Required
1-25	Fabrication of wafer molds	4 h + baking overnight
26-46	Fabrication of PDMS devices	2 h + baking overnight
47-48	Characterization of the PDMS devices	20 min
49-58	Hole-punching and plasma bonding	20 min + baking overnight
59-61	Assembly and connection of off-chip components	20 min
62-70	Manual Operation	1 min per animal + 20 min initial priming and optimization

Table B.4: Troubleshooting table.

Step	Problem	Possible reason	Solution
25	The photoresist on wafer is not rounded after reflow.	Ramping of temperature is not uniform.	Ensure that the cover on hotplate allows adequate heat transfer. Try a new hotplate.
		Photoresist has expired or has been overexposed to air/light.	Use new photoresist.

Continued on Next Page...

Table B.4 – Continued

Step	Problem	Possible reason	Solution
26	Particles on wafer cannot be removed with nitrogen gun.	PDMS and dust particles adhered to the photoresist on wafer surface.	Do not use tape to avoid damaging photoresist structures. Pour a layer of PDMS over the wafer, bake for 1 h, and peel off to remove dust particles as described in Steps 28-39 for **mold-C**.
36	Bubbles trapped in wet PDMS near the wafer surface.	Air was trapped while pouring PDMS.	Use the rounded edge of a paper clip to drag the bubble to dislodge it. Do not touch wafer surface or photoresist structures.
38	Surface of PDMS layers is too rigid and not sticky enough for bonding.	PDMS is thermally overcured.	Ensure that the oven temperature and bake time are correct. Otherwise, reduce the bake time by 5 min in Step 37. Otherwise, try new oven.
38	Surface of PDMS layers is too soft and is not able to provide mechanical support for bonding of layers.	Surface is thermally undercured.	After checking temperature as suggested above, increase the bake time by 5 min in Step 37.

Continued on Next Page...

Table B.4 – Continued

Step	Problem	Possible reason	Solution
41	Failure in punching holes into PDMS.	Particle generation by tearing of PDMS because of dullness of punching tip.	Replace with new hole-puncher.
		PDMS is too rigid.	Check PDMS curing procedure and base/curing agent ratios.
		Metal tip retracts in plastic shaft.	Replace with a new hole-puncher.
		PDMS layer is too thick to completely punch through.	Decrease amount of PDMS used to reduce thickness.
42	PDMS particulates cause chip failure.	Particulates during fabrication or hole-punching block sections of the device (see Figure B-9b).	Wipe down bench surfaces and use fresh aluminum foil after each sequence of fabrication step. Use additional tape to clean PDMS surfaces.
57	Delamination of PDMS thermal bond.	Over-curing of PDMS layers prior to thermal bonding reduces adhesion properties.	Check oven temperature. Reduce the initial curing time in Step 37 to 25 min.

Continued on Next Page...

Table B.4 – Continued

Step	Problem	Possible reason	Solution
		Residue from gloves or external source.	Avoid touching PDMS surfaces that are to be bonded together. Ensure that surface of benches are clean. Change gloves after handling wet PDMS.
57	Channel array is distorted (Figure B-8).	The PDMS flow layer was not properly cured before peeling from **mold-F**.	Check oven temperature and curing time.
		Wafer surface was not free of debris before spinning PDMS.	See Troubleshooting Step 26.
57	**Immobilization membrane** is collapsed/stuck (Figure B-8).	Membrane has bonded to the PDMS **compression layer**.	Use a syringe attached at **port-A** to slowly and gently pressurize the channel to separate the membrane. Be careful to avoid stretching or tearing the membrane to prevent device failure.

Continued on Next Page...

Table B.4 – Continued

Step	Problem	Possible reason	Solution
		Membrane is bonded to the cover glass.	Plug **port-C** with male luer cap and gently pressurize **port-B** to slowly lift the membrane; additionally, a second syringe can be attached to **port-A** to apply a vacuum.
		Membrane is too thin or has torn or stretched preventing operation.	PDMS **flow layer** may be too thin or photoresist on **mold-F** may be too tall. Refer to Figure B-4 for device characterization.
57	Failure of plasma bonding (Figure B-8).	Surfaces are not clean.	Clean the PDMS surface with tape and avoid touching the surfaces.
		Cover glass is cracked.	Increase the amount of fab wipes for padding on the table in Step 51 and use less force when pressing on the device in Step 56.

Continued on Next Page...

Table B.4 – Continued

Step	Problem	Possible reason	Solution
		Plasma chamber is not clean.	Air filters on the vacuum line may not be working properly. Check filters and have plasma chamber cleaned.
62	Failure in filling of **compression layer** from **port-A** with water.	Air leak in the system.	Use a syringe to drip water around potential leaks and check for bubbling. Use appropriate Teflon thread tape to seal leaks.
		Water leak at the steel pin connector to **port-A** of the chip.	The punched hole may be torn or not sealing properly. Reseal around the pin and tubing by applying wet 20:1 PDMS and by baking for 1 hour. Leave the pin and tubing in place to prevent sealing of the hole.
		Air bubbles in the tygon tubing can prevent fluid flow even at high pressures.	Detach the tubing and use a syringe to prime with deionized water.

Continued on Next Page...

Table B.4 – Continued

Step	Problem	Possible reason	Solution
65	Sufficient flow cannot be achieved.	Blockage of external fluidic lines due to possible pinched tubing or dried M9 buffer. Blockage is often hidden in steel connector tubes.	Disconnect each line separately and check for continuity from pressure source. Flush lines with fresh M9/deionized water using syringe.
		Blockage inside the chip or in the channel array (Figure B-9)	Use a syringe filled with M9 to apply gentle pulses to dislodge the debris. Do not apply high pressures to avoid damaging the device. Bleach the chip using the protocol in Table B.5.
66	Cannot achieve sufficient immobilization.	Debris is blocking **compression layer** from compressing uniformly.	See Troubleshooting Step 65 to remove debris.
		15 psi is not sufficient to immobilize the animal	Slowly increase pressure to 20 psi.
		20 psi is not sufficient to immobilize the animal.	The tubing is blocked. See Troubleshooting Step 65.

Continued on Next Page...

Table B.4 – Continued

Step	Problem	Possible reason	Solution
			The fabrication is not within the tolerance in Figure B-4 & Table 1.

Table B.5: Bleaching Protocol (adapted from Lee *et al.* [150])

Step	Bleaching procedure for removal of biological material
1	Remove all of the pins and tubing from the microfluidic device.
2	Prepare a 2% bleach solution in deionized water. (1 ml Bleach : 50 ml DI water)
3	Use a syringe to gently inject the 2% bleach solution into each **port-B** and **port-C** of the device thoroughly filling the entire device. Deliver gentle pulses to dislodge debris. Avoid high pressures to prevent damaging the device.
4	Soak the device for 4 to 12 h to break down the biological material. Soak time is dependent upon the level of contamination.
5	Use the syringe to gently inject additional 2% bleach solution. Gently force the loosened debris out of the chip without delaminating thermally bonded layers
6	Use a separate syringe filled with deionized water to thoroughly rinse the device to remove all of the bleaching solution.
7	Flush the chip with M9 buffer solution and reconnect the ports of the chip.

B.6 Anticipated results

This protocol results in a fully functional microfluidic system capable of studying dynamic cellular processes at subcellular resolution in physiologically active *C. elegans*. The immobilization stability achievable is comparable to that induced by strong anesthetics such

as NaN_3 (See Chapter 3) and is sufficient for tasks such as two-photon imaging [87] and femtosecond laser microsurgery [87]. Once fabricated, the device can be operated by one single syringe and one manual valve.

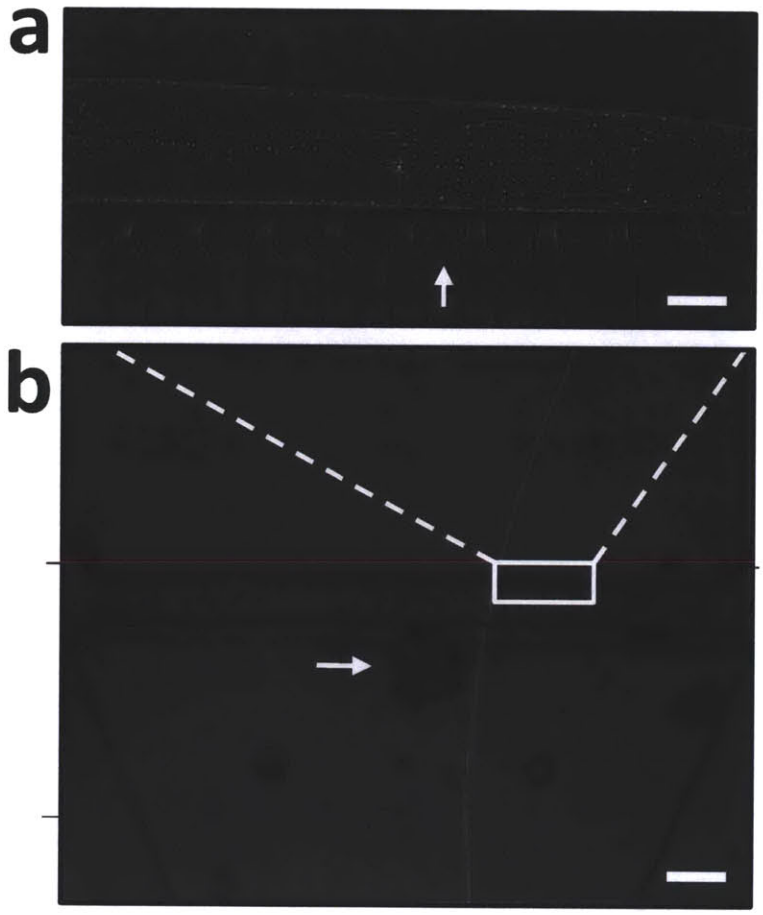

Figure B-10: Device contamination by debris and PDMS particulates. (a) Micrograph of an animal immobilized against the **channel array**. The build-up of debris, which occurs after thousands of cycles, is indicated by the arrow within the **channel array**. Such contamination can be removed by following the bleaching procedure described in Table B.5. Scale bar is 15 µm. (b) Large PDMS debris caused during PDMS hole-punching. Scale bar: 100 µm.

Bibliography

[1] Yanik, M. F., Rohde, C. B. & Pardo-Martin, C. Technologies for micromanipulating, imaging, and phenotyping small invertebrates and vertebrates. *Annual Review of Biomedical Engineering* **13**, 185–217 (2011).

[2] Hertzberg, R. P. & Pope, A. J. High-throughput screening: new technology for the 21st century. *Current Opinion in Chemical Biology* **4**, 445–51 (2000).

[3] Boutros, M. *et al.* Genome-wide RNAi analysis of growth and viability in Drosophila cells. *Science* **303**, 832–5 (2004).

[4] Gupta, P. B. *et al.* Identification of selective inhibitors of cancer stem cells by high-throughput screening. *Cell* **138**, 645–59 (2009).

[5] Wong, J. W. J., Brastianos, H. C., Andersen, R. J. & O'Connor, T. P. A high-throughput screen to identify novel compounds to promote neurite outgrowth. *Journal of Neuroscience Methods* **169**, 34–42 (2008).

[6] Giuliano, K. A., Haskins, J. R. & Taylor, D. L. Advances in high content screening for drug discovery. *Assay and Drug Development Technologies* **1**, 565–77 (2003).

[7] Barbaric, I. *et al.* Novel regulators of stem cell fates identified by a multivariate phenotype screen of small compounds on human embryonic stem cell colonies. *Stem Cell Research* **5**, 104–19 (2010).

[8] Ohnuki, S., Oka, S., Nogami, S. & Ohya, Y. High-content, image-based screening for drug targets in yeast. *PLoS One* **5**, e10177 (2010).

[9] Jan, E. *et al.* High-content screening as a universal tool for fingerprinting of cytotoxicity of nanoparticles. *ACS Nano* **2**, 928–38 (2008).

[10] Comley, J. High content screening: emerging importance of novel reagents/probes and pathway analysis. *Drug Discovery World* **6**, 31–53 (2005).

[11] Neumann, B. *et al.* Phenotypic profiling of the human genome by time-lapse microscopy reveals cell division genes. *Nature* **464**, 721–7 (2010).

[12] Xia, Y. & Whitesides, G. M. Soft lithography. *Annual Review of Materials Science* **28**, 153–184 (1998).

[13] Qin, D., Xia, Y. & Whitesides, G. M. Soft lithography for micro- and nanoscale patterning. *Nature Protocols* **5**, 491–502 (2010).

[14] Gray, J. M. *et al.* Oxygen sensation and social feeding mediated by a C. elegans guanylate cyclase homologue. *Nature* **430**, 317–22 (2004).

[15] Qin, J. & Wheeler, A. R. Maze exploration and learning in C. elegans. *Lab on a Chip* **7**, 186–92 (2007).

[16] Barrière, A. & Félix, M.-A. High local genetic diversity and low outcrossing rate in Caenorhabditis elegans natural populations. *Current Biology* **15**, 1176–84 (2005).

[17] Lockery, S. R. *et al.* Artificial dirt: microfluidic substrates for nematode neurobiology and behavior. *Journal of Neurophysiology* **99**, 3136–43 (2008).

[18] Park, S. *et al.* Enhanced Caenorhabditis elegans locomotion in a structured microfluidic environment. *PLoS One* **3**, e2550 (2008).

[19] Chronis, N., Zimmer, M. & Bargmann, C. I. Microfluidics for in vivo imaging of neuronal and behavioral activity in Caenorhabditis elegans. *Nature Methods* **4**, 727–31 (2007).

[20] Chalasani, S. H. *et al.* Dissecting a circuit for olfactory behaviour in Caenorhabditis elegans. *Nature* **450**, 63–70 (2007).

[21] Chokshi, T. V., Bazopoulou, D. & Chronis, N. An automated microfluidic platform for calcium imaging of chemosensory neurons in Caenorhabditis elegans. *Lab on a Chip* **10**, 2758–63 (2010).

[22] Kim, N., Dempsey, C. M., Zoval, J. V., Sze, J.-Y. & Madou, M. J. Automated microfluidic compact disc (CD) cultivation system of Caenorhabditis elegans. *Sensors and Actuators B: Chemical* **122**, 511–518 (2007).

[23] Bonner, W. A., Hulett, H. R., Sweet, R. G. & Herzenberg, L. A. Fluorescence activated cell sorting. *The Review of Scientific Instruments* **43**, 404–9 (1972).

[24] Pulak, R. Techniques for analysis, sorting, and dispensing of C. elegans on the COPAS flow-sorting system. *Methods in Molecular Biology* **351**, 275–86 (2006).

[25] Doitsidou, M., Flames, N., Lee, A. C., Boyanov, A. & Hobert, O. Automated screening for mutants affecting dopaminergic-neuron specification in C. elegans. *Nature Methods* **5**, 869–72 (2008).

[26] Stoeckius, M. *et al.* Large-scale sorting of C. elegans embryos reveals the dynamics of small RNA expression. *Nature Methods* **6**, 745–51 (2009).

[27] Fernandez, A. G., Mis, E. K., Bargmann, B. O. R., Birnbaum, K. D. & Piano, F. Automated sorting of live C. elegans using laFACS. *Nature Methods* **7**, 417–8 (2010).

[28] Fernandez, A. G. & Piano, F. MEL-28 is downstream of the Ran cycle and is required for nuclear-envelope function and chromatin maintenance. *Current Biology* **16**, 1757–63 (2006).

[29] Pawley, J. B. *Handbook of Biological Confocal Microscopy* (Springer, 1995).

[30] Denk, W., Strickler, J. H. & Webb, W. W. Two-photon laser scanning fluorescence microscopy. *Science* **248**, 73–6 (1990).

[31] Filippidis, G. *et al.* Imaging of Caenorhabditis elegans neurons by second-harmonic generation and two-photon excitation fluorescence. *Journal of Biomedical Optics* **10**, 024015–8 (2005).

[32] Gualda, E. J. *et al.* In vivo imaging of cellular structures in Caenorhabditis elegans by combined TPEF, SHG and THG microscopy. *Journal of Microscopy* **229**, 141–50 (2008).

[33] Filippidis, G. *et al.* In vivo imaging of cell morphology and cellular processes in Caenorhabditis elegans, using non-linear phenomena. *Micron* **40**, 876–80 (2009).

[34] Cheng, J.-X. & Xie, X. S. Coherent Anti-Stokes Raman Scattering Microscopy: Instrumentation, Theory, and Applications. *The Journal of Physical Chemistry B* **108**, 827–840 (2004).

[35] Hellerer, T. *et al.* Monitoring of lipid storage in Caenorhabditis elegans using coherent anti-Stokes Raman scattering (CARS) microscopy. *Proceedings of the National Academy of Sciences of the United States of America* **104**, 14658–63 (2007).

[36] Le, T. T., Duren, H. M., Slipchenko, M. N., Hu, C.-D. & Cheng, J.-X. Label-free quantitative analysis of lipid metabolism in living Caenorhabditis elegans. *Journal of Lipid Research* **51**, 672–7 (2010).

[37] Deisseroth, K. *et al.* Next-generation optical technologies for illuminating genetically targeted brain circuits. *The Journal of Neuroscience* **26**, 10380–6 (2006).

[38] Nagel, G. *et al.* Channelrhodopsin-2, a directly light-gated cation-selective membrane channel. *Proceedings of the National Academy of Sciences of the United States of America* **100**, 13940–5 (2003).

[39] Boyden, E. S., Zhang, F., Bamberg, E., Nagel, G. & Deisseroth, K. Millisecond-timescale, genetically targeted optical control of neural activity. *Nature Neuroscience* **8**, 1263–8 (2005).

[40] Zhang, F., Wang, L.-P., Boyden, E. S. & Deisseroth, K. Channelrhodopsin-2 and optical control of excitable cells. *Nature Methods* **3**, 785–92 (2006).

[41] Kolbe, M. Structure of the Light-Driven Chloride Pump Halorhodopsin at 1.8 A Resolution. *Science* **288**, 1390–1396 (2000).

[42] Zhang, F. *et al.* Multimodal fast optical interrogation of neural circuitry. *Nature* **446**, 633–9 (2007).

[43] Han, X. & Boyden, E. S. Multiple-color optical activation, silencing, and desynchronization of neural activity, with single-spike temporal resolution. *PLoS One* **2**, e299 (2007).

[44] Stirman, J. N., Brauner, M., Gottschalk, A. & Lu, H. High-throughput study of synaptic transmission at the neuromuscular junction enabled by optogenetics and microfluidics. *Journal of Neuroscience Methods* **191**, 90–3 (2010).

[45] Lange, D., Storment, C. W., Conley, C. A. & Kovacs, G. T. A. A microfluidic shadow imaging system for the study of the nematode Caenorhabditis elegans in space. *Sensors and Actuators B: Chemical* **107**, 904–914 (2005).

[46] Psaltis, D., Quake, S. R. & Yang, C. Developing optofluidic technology through the fusion of microfluidics and optics. *Nature* **442**, 381–6 (2006).

[47] Heng, X. *et al.* Optofluidic microscopy–a method for implementing a high resolution optical microscope on a chip. *Lab on a Chip* **6**, 1274–6 (2006).

[48] Cui, X. *et al.* Lensless high-resolution on-chip optofluidic microscopes for Caenorhabditis elegans and cell imaging. *Proceedings of the National Academy of Sciences of the United States of America* **105**, 10670–5 (2008).

[49] Pang, S. *et al.* Implementation of a color-capable optofluidic microscope on a RGB CMOS color sensor chip substrate. *Lab on a Chip* **10**, 411–4 (2010).

[50] Isikman, S., Seo, S., Sencan, I., Erlinger, A. & Ozcan, A. Lensfree cell holography on a chip: From holographic cell signatures to microscopic reconstruction. In *2009 IEEE LEOS Annual Meeting Conference Proceedings*, 404–405 (IEEE, 2009).

[51] Isikman, S. O. *et al.* Color and monochrome lensless on-chip imaging of Caenorhabditis elegans over a wide field-of-view. *Lab on a Chip* **10**, 1109–12 (2010).

[52] Fienup, J. R. Reconstruction of an object from the modulus of its Fourier transform. *Optics Letters* **3**, 27 (1978).

[53] Koren, G., Polack, F. & Joyeux, D. Iterative algorithms for twin-image elimination in in-line holography using finite-support constraints. *Journal of the Optical Society of America A* **10**, 423 (1993).

[54] Buckingham, S. D. & Sattelle, D. B. Strategies for automated analysis of C. elegans locomotion. *Invertebrate Neuroscience* **8**, 121–31 (2008).

[55] Sznitman, R., Gupta, M., Hager, G. D., Arratia, P. E. & Sznitman, J. Multi-environment model estimation for motility analysis of Caenorhabditis elegans. *PLoS One* **5**, e11631 (2010).

[56] Faumont, S. & Lockery, S. R. The awake behaving worm: simultaneous imaging of neuronal activity and behavior in intact animals at millimeter scale. *Journal of Neurophysiology* **95**, 1976–81 (2006).

[57] Ben Arous, J., Tanizawa, Y., Rabinowitch, I., Chatenay, D. & Schafer, W. R. Automated imaging of neuronal activity in freely behaving Caenorhabditis elegans. *Journal of Neuroscience Methods* **187**, 229–34 (2010).

[58] Peng, H., Long, F., Liu, X., Kim, S. K. & Myers, E. W. Straightening Caenorhabditis elegans images. *Bioinformatics* **24**, 234–42 (2008).

[59] Wahlby, C. *et al.* Resolving clustered worms via probabilistic shape models. In *2010 IEEE International Symposium on Biomedical Imaging: From Nano to Macro*, 552–555 (IEEE, 2010).

[60] Orlov, N., Johnston, J., Macura, T., Wolkow, C. & Goldberg, I. Pattern Recognition Approaches to Compute Image Similarities: Application to Age Related Morphological Change. In *3rd IEEE International Symposium on Biomedical Imaging: Macro to Nano, 2006.*, 1152–1155 (IEEE, 2006).

[61] Johnston, J., Iser, W. B., Chow, D. K., Goldberg, I. G. & Wolkow, C. A. Quantitative image analysis reveals distinct structural transitions during aging in Caenorhabditis elegans tissues. *PLoS One* **3**, e2821 (2008).

[62] Sulston, J. E. & Horvitz, H. R. Post-embryonic cell lineages of the nematode, Caenorhabditis elegans. *Developmental Biology* **56**, 110–56 (1977).

[63] Kimble, J. & Hirsh, D. The postembryonic cell lineages of the hermaphrodite and male gonads in Caenorhabditis elegans. *Developmental Biology* **70**, 396–417 (1979).

[64] White, J. G., Southgate, E., Thomson, J. N. & Brenner, S. The Structure of the Nervous System of the Nematode Caenorhabditis elegans. *Royal Society of London Philosophical Transactions Series B* **314**, 1–340 (1986).

[65] Long, F., Peng, H., Liu, X., Kim, S. K. & Myers, E. A 3D digital atlas of C. elegans and its application to single-cell analyses. *Nature Methods* **6**, 667–72 (2009).

[66] Bao, Z. *et al.* Automated cell lineage tracing in Caenorhabditis elegans. *Proceedings of the National Academy of Sciences of the United States of America* **103**, 2707–12 (2006).

[67] Murray, J. I. *et al.* Automated analysis of embryonic gene expression with cellular resolution in C. elegans. *Nature Methods* **5**, 703–9 (2008).

[68] Peng, H., Long, F. & Myers, E. W. VANO: a volume-object image annotation system. *Bioinformatics* **25**, 695–7 (2009).

[69] Liu, X. *et al.* Analysis of cell fate from single-cell gene expression profiles in C. elegans. *Cell* **139**, 623–33 (2009).

[70] Sulston, J. & White, J. Regulation and cell autonomy during postembryonic development of Caenorhabditis elegans. *Developmental Biology* **78**, 577–597 (1980).

[71] Kimble, J. E. & White, J. G. On the control of germ cell development in Caenorhabditis elegans. *Developmental Biology* **81**, 208–19 (1981).

[72] Yanik, M. F. *et al.* Neurosurgery: functional regeneration after laser axotomy. *Nature* **432**, 822 (2004).

[73] Yanik, M. F. *et al.* Nerve regeneration in Caenorhabditis elegans after femtosecond laser axotomy. *IEEE Journal of Selected Topics in Quantum Electronics* **12**, 1283–1291 (2006).

[74] Wu, Z. *et al.* Caenorhabditis elegans neuronal regeneration is influenced by life stage, ephrin signaling, and synaptic branching. *Proceedings of the National Academy of Sciences of the United States of America* **104**, 15132–7 (2007).

[75] Gabel, C. V. *et al.* Distinct cellular and molecular mechanisms mediate initial axon development and adult-stage axon regeneration in C. elegans. *Development* **135**, 1129–36 (2008).

[76] Hammarlund, M., Nix, P., Hauth, L., Jorgensen, E. M. & Bastiani, M. J. Axon regeneration requires a conserved MAP kinase pathway. *Science* **323**, 802–6 (2009).

[77] Yan, D., Wu, Z., Chisholm, A. D. & Jin, Y. The DLK-1 kinase promotes mRNA stability and local translation in C. elegans synapses and axon regeneration. *Cell* **138**, 1005–18 (2009).

[78] Ghosh-Roy, A., Wu, Z., Goncharov, A., Jin, Y. & Chisholm, A. D. Calcium and cyclic AMP promote axonal regeneration in Caenorhabditis elegans and require DLK-1 kinase. *The Journal of Neuroscience* **30**, 3175–83 (2010).

[79] Rohde, C. B., Zeng, F., Gonzalez-Rubio, R., Angel, M. & Yanik, M. F. Microfluidic system for on-chip high-throughput whole-animal sorting and screening at subcellular resolution. *Proceedings of the National Academy of Sciences of the United States of America* **104**, 13891–5 (2007).

[80] Massie, M. R., Lapoczka, E. M., Boggs, K. D., Stine, K. E. & White, G. E. Exposure to the metabolic inhibitor sodium azide induces stress protein expression and thermotolerance in the nematode Caenorhabditis elegans. *Cell Stress & Chaperones* **8**, 1–7 (2003).

[81] Podbilewicz, B. & Gruenbaum, Y. Live Imaging of Caenorhabditis elegans: Preparation of Samples. *Cold Spring Harbor Protocols* **2006**, pdb.prot4601–pdb.prot4601 (2006).

[82] Lewbart, G. A. & Bodri, M. S. *Nematodes.* In *Invertebrate Medicine* (Blackwell Publishing, 2006).

[83] Melin, J. & Quake, S. R. Microfluidic large-scale integration: the evolution of design rules for biological automation. *Annual Review of Biophysics and Biomolecular Structure* **36**, 213–31 (2007).

[84] Dupuy, D. *et al.* Genome-scale analysis of in vivo spatiotemporal promoter activity in Caenorhabditis elegans. *Nature Biotechnology* **25**, 663–8 (2007).

[85] Kaletta, T., Butler, L., Bogaert, T., Carroll, P. M. & FitzGerald, K. J. *Model organisms in drug discovery* (John Wiley and Sons, 2003).

[86] Zhang, J.-H. A Simple Statistical Parameter for Use in Evaluation and Validation of High Throughput Screening Assays. *Journal of Biomolecular Screening* **4**, 67–73 (1999).

[87] Zeng, F., Rohde, C. B. & Yanik, M. F. Sub-cellular precision on-chip small-animal immobilization, multi-photon imaging and femtosecond-laser manipulation. *Lab on a Chip* **8**, 653–6 (2008).

[88] Vogel, A., Noack, J., Hüttman, G. & Paltauf, G. Mechanisms of femtosecond laser nanosurgery of cells and tissues. *Applied Physics B* **81**, 1015–1047 (2005).

[89] Samara, C. *et al.* High-throughput in vivo femtosecond laser neurosurgery screen reveals factors modulating regeneration. *Proceedings of the National Academy of Sciences of the United States of America* **107**, 18342–18347 (2010).

[90] Silver, J. & Miller, J. H. Regeneration beyond the glial scar. *Nature Reviews. Neuroscience* **5**, 146–56 (2004).

[91] Neumann, S. & Woolf, C. Regeneration of dorsal column fibers into and beyond the lesion site following adult spinal cord injury. *Neuron* **23**, 83–91 (1999).

[92] Park, K. K. *et al.* Promoting axon regeneration in the adult CNS by modulation of the PTEN/mTOR pathway. *Science* **322**, 963–6 (2008).

[93] Bhatt, D. H., Otto, S. J., Depoister, B. & Fetcho, J. R. Cyclic AMP-induced repair of zebrafish spinal circuits. *Science* **305**, 254–8 (2004).

[94] Steinmeyer, J. D. *et al.* Construction of a femtosecond laser microsurgery system. *Nature Protocols* **5**, 395–407 (2010).

[95] Guo, S. X. *et al.* Femtosecond laser nanoaxotomy lab-on-a chip for in vivo nerve regeneration studies. *Nature Methods* **5**, 531–533 (2008).

[96] Hulme, S. E., Shevkoplyas, S. S., Apfeld, J., Fontana, W. & Whitesides, G. M. A microfabricated array of clamps for immobilizing and imaging C. elegans. *Lab on a Chip* **7**, 1515–23 (2007).

[97] Chung, K., Crane, M. M. & Lu, H. Automated on-chip rapid microscopy, phenotyping and sorting of C. elegans. *Nature Methods* **5**, 637–43 (2008).

[98] Chokshi, T. V., Ben-Yakar, A. & Chronis, N. CO2 and compressive immobilization of C. elegans on-chip. *Lab on a Chip* **9**, 151–7 (2009).

[99] Brenner, S. The genetics of Caenorhabditis elegans. *Genetics* **77**, 71–94 (1974).

[100] Chung, K. & Lu, H. Automated high-throughput cell microsurgery on-chip. *Lab on a Chip* **9**, 2764–2766 (2009).

[101] Haggarty, S. J. *et al.* Dissecting cellular processes using small molecules: identification of colchicine-like, taxol-like and other small molecules that perturb mitosis. *Chemistry & Biology* **7**, 275–286 (2000).

[102] Mayer, T. U. *et al.* Small molecule inhibitor of mitotic spindle bipolarity identified in a phenotype-based screen. *Science* **286**, 971–4 (1999).

[103] Goodman, M. B. & Schwarz, E. M. Transducing touch in Caenorhabditis elegans. *Annual Review of Physiology* **65**, 429–52 (2003).

[104] Syntichaki, P. & Tavernarakis, N. The biochemistry of neuronal necrosis: rogue biology? *Nature Reviews. Neuroscience* **4**, 672–84 (2003).

[105] Ruegg, U. T., Burgess, G. M. & Rüegg, U. T. Staurosporine, K-252 and UCN-01: potent but nonspecific inhibitors of protein kinases. *Trends in Pharmacological Sciences* **10**, 218–20 (1989).

[106] Couldwell, W. T. *et al.* Protein kinase C inhibitors induce apoptosis in human malignant glioma cell lines. *FEBS Letters* **345**, 43–6 (1994).

[107] Posmantur, R., McGinnis, K., Nadimpalli, R., Gilbertsen, R. B. & Wang, K. K. Characterization of CPP32-like protease activity following apoptotic challenge in SH-SY5Y neuroblastoma cells. *Journal of Neurochemistry* **68**, 2328–37 (1997).

[108] Kruman, I., Guo, Q. & Mattson, M. P. Calcium and reactive oxygen species mediate staurosporine-induced mitochondrial dysfunction and apoptosis in PC12 cells. *Journal of Neuroscience Research* **51**, 293–308 (1998).

[109] Yue, T. L. *et al.* Staurosporine-induced apoptosis in cardiomyocytes: A potential role of caspase-3. *Journal of Molecular and Cellular Cardiology* **30**, 495–507 (1998).

[110] Srinivasan, A. *et al.* Bcl-2 expression in neural cells blocks activation of ICE/CED-3 family proteases during apoptosis. *The Journal of Neuroscience* **16**, 5654–60 (1996).

[111] Jacobsen, M. D., Weil, M. & Raff, M. C. Role of Ced-3/ICE-family proteases in staurosporine-induced programmed cell death. *The Journal of Cell Biology* **133**, 1041–51 (1996).

[112] Armsby, C. C., Brugnara, C. & Alper, S. L. Cation transport in mouse erythrocytes: role of K(+)-Cl- cotransport in regulatory volume decrease. *The American Journal of Physiology* **268**, 894–902 (1995).

[113] Bize, I. & Dunham, P. B. Staurosporine, a protein kinase inhibitor, activates K-Cl cotransport in LK sheep erythrocytes. *The American Journal of Physiology* **266**, C759–70 (1994).

[114] Holtzman, E. J. *et al.* Cloning, characterization, and gene organization of K-Cl cotransporter from pig and human kidney and C. elegans. *The American Journal of Physiology* **275**, F550–64 (1998).

[115] Sassa, T. & Miwa, J. Purification and characterization of protein kinase C from the nematode Caenorhabditis elegans. *The Biochemical Journal* **282**, 219–23 (1992).

[116] Herbert, J. M., Augereau, J. M., Gleye, J. & Maffrand, J. P. Chelerythrine is a potent and specific inhibitor of protein kinase C. *Biochemical and Biophysical Research Communications* **172**, 993–9 (1990).

[117] Gschwendt, M., Leibersperger, H., Kittstein, W. & Marks, F. Protein kinase C zeta and eta in murine epidermis. TPA induces down-regulation of PKC eta but not PKC zeta. *FEBS Letters* **307**, 151–5 (1992).

[118] Heacock, A. M. & Agranoff, B. W. Protein kinase inhibitors block neurite outgrowth from explants of goldfish retina. *Neurochemical Research* **22**, 1179–85 (1997).

[119] Ekström, P. A., Bergstrand, H. & Edström, A. Effects of protein kinase inhibitors on regeneration in vitro of adult frog sciatic sensory axons. *Journal of Neuroscience Research* **31**, 462–9 (1992).

[120] Wu, D.-Y., Zheng, J.-Q., McDonald, M. A., Chang, B. & Twiss, J. L. PKC isozymes in the enhanced regrowth of retinal neurites after optic nerve injury. *Investigative Ophthalmology & Visual Science* **44**, 2783–90 (2003).

[121] Wiklund, P. & Ekström, P. A. Protein kinase C inhibition has only a transient growth arresting effect on in vitro regenerating mouse sensory neurons. *Neuroscience Letters* **275**, 155–8 (1999).

[122] Jian, X., Hidaka, H. & Schmidt, J. T. Kinase requirement for retinal growth cone motility. *Journal of Neurobiology* **25**, 1310–28 (1994).

[123] Toni, N., Stoppini, L. & Muller, D. Staurosporine but not chelerythrine inhibits regeneration in hippocampal organotypic cultures. *Synapse* **27**, 199–207 (1997).

[124] Lavie, Y., Dybowski, J. & Agranoff, B. W. Wortmannin blocks goldfish retinal phosphatidylinositol 3-kinase and neurite outgrowth. *Neurochemical Research* **22**, 373–378 (1997).

[125] Kimpinski, K. & Mearow, K. Neurite growth promotion by nerve growth factor and insulin-like growth factor-1 in cultured adult sensory neurons: role of phosphoinositide 3-kinase and mitogen activated protein kinase. *Journal of Neuroscience Research* **63**, 486–99 (2001).

[126] Qiu, J. *et al.* Spinal axon regeneration induced by elevation of cyclic AMP. *Neuron* **34**, 895–903 (2002).

[127] Dergham, P. *et al.* Rho signaling pathway targeted to promote spinal cord repair. *The Journal of Neuroscience* **22**, 6570–6577 (2002).

[128] Sjögreen, B., Wiklund, P. & Ekström, P. A. Mitogen activated protein kinase inhibition by PD98059 blocks nerve growth factor stimulated axonal outgrowth from adult mouse dorsal root ganglia in vitro. *Neuroscience* **100**, 407–16 (2000).

[129] Rohde, C. B. & Yanik, M. F. Multi-time-point immobilization, subcellular imaging, and microsurgery of C. elegans in standard multiwell plates. *Nature Communications* **2**, 1–7 (2011).

[130] Liu, J., Hansen, C. & Quake, S. R. Solving the "world-to-chip" interface problem with a microfluidic matrix. *Analytical Chemistry* **75**, 4718–23 (2003).

[131] Hulme, S. E. *et al.* Lifespan-on-a-chip: microfluidic chambers for performing lifelong observation of C. elegans. *Lab on a Chip* **10**, 589–97 (2010).

[132] Petrascheck, M., Ye, X. & Buck, L. B. An antidepressant that extends lifespan in adult Caenorhabditis elegans. *Nature* **450**, 553–6 (2007).

[133] Hosono, R. Sterilization and growth inhibition of caenorhabditis elegans by 5-fluorodeoxyuridine. *Experimental Gerontology* **13**, 369 – 373 (1978).

[134] Mitchell, D. H., Stiles, J. W., Santelli, J. & Sanadi, D. R. Synchronous growth and aging of caenorhabditis elegans in the presence of fluorodeoxyuridine. *Journal of Gerontology* **34**, 28–36 (1979).

[135] Long, F., Peng, H. & Myers, E. Automatic Segmentation of Nuclei in 3D Microscopy Images of C. Elegans. In *2007 4th IEEE International Symposium on Biomedical Imaging: From Nano to Macro*, 536–539 (IEEE, 2007).

[136] Budovskaya, Y. V. *et al.* An elt-3/elt-5/elt-6 GATA transcription circuit guides aging in C. elegans. *Cell* **134**, 291–303 (2008).

[137] Botvinick, E. L., Venugopalan, V., Shah, J. V., Liaw, L. H. & Berns, M. W. Controlled ablation of microtubules using a picosecond laser. *Biophysical Journal* **87**, 4203–4212 (2004).

[138] Watanabe, W. Femtosecond laser disruption of subcellular organelles in a living cell. *Optics Express* **12**, 4203–4213 (2004).

[139] Heisterkamp, A. Pulse energy dependence of subcellular dissection by femtosecond laser pulses. *Optics Express* **13**, 3690–3696 (2005).

[140] Tirlapur, U. K. & Konig, K. Targeted transfection by femtosecond laser. *Nature* **418**, 290–291 (2002).

[141] Vogel, A. Mechanisms of laser-induced dissection and transport of histologic specimens. *Biophysical Journal* **93**, 4481–4500 (2007).

[142] Shen, N. Ablation of cytoskeletal filaments and mitochondria in live cells using femtosecond laser nanoscissor. *Mechanics and Chemistry of Biosystems* **2**, 17–25 (2005).

[143] O'Brien, G. S. *et al.* Two-photon axotomy and time-lapse confocal imaging in live zebrafish embryos. *Journal of Visualized Experiments* **24** (2009).

[144] Frostig, R. D. *In Vivo Optical Imaging of Brain Function* (Nature Publishing Group, 2002).

[145] Sulston, J. & Hodgkin, J. *Methods.* In *The Nematode C. elegans* (Cold Spring Harbor Laboratory Press, 1998).

[146] Bourgeois, F. & Ben-Yakar, A. Femtosecond laser nanoaxotomy properties and their effect on nerve regeneration in C. elegans. *Optics Express* **15**, 8521–8531 (2007).

[147] Gilleland, C. L., Rohde, C. B., Zeng, F. & Yanik, M. F. Microfluidic immobilization of physiologically active Caenorhabditis elegans. *Nature Protocols* **5**, 1888–902 (2010).

[148] Unger, M. A., Chou, H. P., Thorsen, T., Scherer, A. & Quake, S. R. Monolithic microfabricated valves and pumps by multilayer soft lithography. *Science* **288**, 113–6 (2000).

[149] Fang-Yen, C., Wasserman, S., Sengupta, P. & Samuel, A. D. Agarose immobilization of C. elegans. *Worm Breeder's Gazette* **18** (2009).

[150] Lee, J. N., Park, C. & Whitesides, G. M. Solvent compatibility of poly(dimethylsiloxane)-based microfluidic devices. *Analytical Chemistry* **75**, 6544–54 (2003).